2019

Behavior and Transport of Organic Acids in the Troposphere using Observational Data and Models

Victoria Ann Treadaway
University of Rhode Island, treachang@gmail.com

BEHAVIOR AND TRANSPORT OF ORGANIC ACIDS IN THE TROPOSPHERE USING OBSERVATIONAL DATA AND MODELS

BY

VICTORIA ANN TREADAWAY

A DISSERTATION SUBMITTED IN PARTIAL FULFILLMENT OF THE REQUIREMENTS FOR THE DEGREE OF

DOCTOR OF PHILOSOPHY

IN

OCEANOGRAPHY

UNIVERSITY OF RHODE ISLAND

2019

DOCTOR OF PHILOSOPHY DISSERTATION

OF

VICTORIA ANN TREADWAY

APPROVED:

Dissertation Committee:

Major Professor Brian Heikes

Brice Loose

James Smith

Nasser H. Zawia
DEAN OF THE GRADUATE SCHOOL

UNIVERSITY OF RHODE ISLAND
2019

ABSTRACT

Formic acid (HFo) and acetic acid (HAc) have both natural and anthropogenic sources and a role in the atmospheric processing of carbon. These organic acids also have an increasing importance in setting the acidity of precipitation as nitrate and sulfate concentrations have decreased. This dissertation examines HFo and HAc tropospheric formation and transport in the continental United States using observations and models. Observational data from two field campaigns were collected with the peroxide chemical ionization mass spectrometer (PCIMS) using iodide clusters for both HFo and HAc recorded at mass-to-charge ratios of 173 and 187. The first campaign, the Deep Convective Clouds and Chemistry Experiment (DC3), was in May and June 2012 and observations extended from the surface to 13 km over the central and eastern United States. The second campaign, the Front Range Air Pollution and Photochemistry Experiment (FRAPPÉ), was in July and August 2014 with measurements from the surface to 7 km over the Colorado Front Range. Post-mission calibration work determined glycolaldehyde (GA) is a significant isobaric interference to HAc with the HAc:GA sensitivity ranging from 1:1 to 1:10. PCIMS HAc data from both campaigns are reported as the acetic acid equivalent sum (AAES). Based on DC3 model work and estimates of secondary production during FRAPPÉ the instrumental sensitivity was closer to a 1:1. Manuscripts 1 and 2 focus on the DC3 May 21st airmass storm case study at the Alabama/Tennessee border. During this flight a 700 ppt HFo plume at 8 km was observed, approximately 300 ppt in excess of boundary layer air. Different potential reasons for this increase including aqueous production and a pH dependent scavenging were evaluated with the Weather Research and

Forecasting model version 3.7 coupled with chemistry (WRF-Chem). Manuscript 1 evaluated the WRF-Chem meteorological reproduction of the airmass storm and the applicability of the Model for Ozone And Related chemical Tracers version 4 and Model for Simulating Aerosol Interactions and Chemistry (MOZART-MOSAIC) compatible microphysics schemes, Morrison and Purdue Lin, in conjunction with a lightning data assimilation (LDA) method. The Morrison microphysics scheme with an LDA temperature range of 261 – 291 K best represented the case study storm. Manuscript 2 showed that there was no difference in WRF-Chem scavenging between a convective complex and isolated convection. It is possible to have cloud top HFo greater than cloud base in a more acidic cloud, pH of 3.5, with multiple HFo aqueous sources, and assuming there is aqueous chemistry up to -40^{o}C. Manuscript 3 investigated HFo and AAES distributions on the Colorado Front Range using three geographic and four chemical classifications. HFo was highest near predominately biogenic sources with the Denver Metropolitan area as the second highest region. AAES was higher than HFo throughout the campaign with the highest AAES in the Denver Metropolitan area and during the Greeley missed approaches. This dissertation highlights that precipitation chemistry influences organic acids in the upper troposphere. Additionally, HFo and HAc gas phase production are controlled by different emission sources which could provide insight into the atmospheric processing of carbon.

ACKNOWLEDGMENTS

First and foremost I would like to thank my advisor Brian Heikes. He introduced me to a field I didn't know existed and has worked alongside me through every hurdle and complication. I have learned a lot from him in my time at GSO and I am forever grateful he took on a confused chemist that didn't know what she wanted to study. I would also like to thank my committee for their support and patience through this process. A special thank you to Mary Barth who guided this experimentalist into the world of modeling and patiently held my hand as I navigated Fortran, super computers, and WRF-Chem. There are countless other professionals who have helped along the way and made the work presented here possible. Thank you.

I would like to thank the GSO community that helped mold me from a young, naïve chemist into a slightly less young atmospheric chemist and oceanographer. Thank you to David Smith and Meredith Clark for your support. Thank you to Cornelia for always putting a smile on my face and sharing a seemingly never ending supply of candy. Thank you to everyone in CACS I had the privilege of knowing over the last 8 years. You have made me a better scientist and person. Thank you to all the friends I have made while living in RI. You have kept me going through this long process and made my life brighter. Listing you all would make this dissertation even longer! A special thank you to Christina and Mary. You were both unexpected lifelong friends that I never could have guessed I would meet when I applied to GSO. Finally, thank you to my family. You supported and cheered me on every step of the way even when you didn't understand what those steps were. Thank you for everything. I am forever grateful for the opportunities and friendships GSO has provided.

PREFACE

This dissertation is written in manuscript format with an introduction chapter presenting the state of organic acid understanding in the literature and a brief overview of the three manuscripts. The first manuscript, *Evaluating MOZART-MOSIAC Compatible Cloud Microphysics Schemes in Conjunction with Lightning Data Assimilation for the DC3 May 21st Airmass Storm*, is prepared for publication in Geosciences Model Development. The second manuscript, *Convective Transport and Scavenging of Formic and Acetic Acid over the Central United States during DC3*, is prepared for publication in Journal of Geophysical Research: Atmospheres. The third manuscript, *Characterizing Formic and Acetic Acid Sources on the Colorado Front Range*, is prepared for publication in Journal of Geophysical Research: Atmospheres. The dissertation wraps up with a conclusion chapter answers the questions posed in the introduction and highlights the major takeaways from this work.

TABLE OF CONTENTS

LIST OF TABLES

LIST OF FIGURES

LIST OF ABBREVIATIONS

Acetic Acid Equivalent Sum	AAES
Acetic Acid	HAc
Formic Acid	HFo
Glycolaldehyde	GA
Peroxide Chemical Ionization Mass Spectrometer	PCIMS
Scavenging Efficiency	SE
Cloud Mass Fraction	q_{cloud}
Ice Mass Fraction	q_{ice}
WRF-Chem Soluble Species	q_j
Water Vapor Saturation	Q_{sat}
Observed Soluble Species	S_j
Weather Research and Forecasting Model	WRF-Chem

INTRODUCTION

Formic acid (HFo) and acetic acid (HAc) have both natural and anthropogenic sources and play a significant role in atmospheric chemical processes – in particular volatile organic compound (VOC) and oxygenated volatile organic compound (OVOC) processing in the troposphere and precipitation chemistry. Secondary production is a significant source for both acids especially from biogenic precursors, biomass burning, secondary organic aerosols, and photochemical production from VOCs and OVOCs (Khare et al., 1999; Paulot et al., 2011; Yuan et al., 2015). Both organic acids have been studied for decades however a great deal of uncertainty remains concerning the extent and pathways of their secondary production. Chemical transport model simulations presented by multiple authors highlight the large discrepancies between model and measurements as a result of these unknown pathways (Millet et al., 2015; Paulot et al., 2011; Stavrakou et al., 2012; Yuan et al., 2015). For example, Yuan et al. (2015) reported model HFo results 13 - 40 times lower than measurements. Millet et al. (2015) highlighted that increasing secondary sources in order to close the HFo budget, such as from isoprene ozonolysis, requires significant alteration of current product yields to keep the carbon balance. Closing the organic acid budgets will improve our overall understanding of VOC chemistry.

Part of this discrepancy could be from underrepresentation of HFo from the Criegee biradical. The Criegee reaction series is important as it is a major degradation pathway for biogenic (e.g. isoprene and pinenes) and anthropogenic (e.g. ethene and propene) alkenes. The Criegee biradical reacts with H_2O, NO, SO_2, and CO leading to

a variety of different products which have not all been identified (Neeb et al., 1997). Organic acids are formed from the reaction of the stabilized biradical with H_2O:

$$H_2C = CH_2 + O_3 \rightarrow HCOH + [H_2COO]^* \quad (1)$$

$$[H_2COO]^* + M \rightarrow H_2COO + M \quad (2)$$

$$H_2COO + H_2O \rightarrow HC(O)OH + H_2O \quad (3)$$

Reaction 3 produces hydroxymethyl hydroperoxide ($HOCH_2OOH$) which decomposes under atmospheric conditions to HFo (Neeb et al., 1997). In laboratory experiments the presence of water increased HFo production from the Criegee biradical up to 10 times the dry HFo production (Neeb et al., 1997). HFo formation from the Criegee biradical could explain a great deal of the current discrepancy between models and measurements.

HFo and HAc are fairly soluble species. HFo Henry's Law constant is 8900 M/atm and HAc is 4100 M/atm at 298 K (Johnson et al., 1996); therefore, wet deposition is a dominant sink for both acids especially near the surface. HFo and HAc contribute to the free acidity (portion of total acidity that exists in the form of an acid) of rainwater all over the world. Acid rain (pH < 5.0) is generally considered to be influenced by SO_2 and NO_x from anthropogenic emissions though there are several chemicals influencing the pH of rain and cloud water. Emission controls on NO_x and SO_2 have led to a reduction in sulfate and nitrate and a consequent increase in precipitation pH. This change in pH is expected to be reflected in aerosol composition and will increase the proportion of the weaker organic acids in these waters. Over thirty years ago HFo and HAc comprised 64% of the volume weighed free acidity at a remote site in Australia (Keene et al., 1983) and 16% in North Carolina (Keene &

Galloway, 1984). It is very likely their relative contribution has increased as SO_2 and NO_x emissions decreased.

Wet and dry deposition are the largest HFo and HAc sinks leading to a lifetime of a few days for both acids. If they reach the upper troposphere the lifetimes increase to 20+ days because reaction with HO is the dominant gas phase sink. In general, one efficient pathway to move chemical species to the upper troposphere is convection. HFo and HAc are assumed to be mostly scavenged in convective systems based on their solubilities. Barth et al. (2007) presented model results indicating that the amount of HFo in the outflow depends on the storm type (affecting aqueous phase HFo production) as well as cloud and rainwater pH. Barth et al. (2007) determined that it may be possible to use HFo to detect cloud-processed air though it is highly dependent on cloud conditions and the initial concentration of HFo. Traditionally, HFo and HAc have not been the focus of modeled convective storm chemistry compared to peroxides and formaldehyde. In addition, the majority of available measurements for HFo and HAc in the United States did not sample vertical profiles to the upper troposphere. For example, Jones et al. (2014), Le Breton et al. (2012), Millet et al. (2015), Reiner et al. (1999), and Talbot et al. (1996) have reported vertical profiles for HFo and/or HAc though only Reiner et al. (1999) and Talbot et al. (1996) sampled above 7 km.

This dissertation explores the formation, transportation, and removal of HFo and HAc in the troposphere. Studying organic acids will help us understand precipitation chemistry and atmospheric carbon processing. This dissertation addresses the following questions:

1. Does organic acid scavenging extent differ between a convective multicell complex and an isolated convective cell?
2. Can HFo serve as a tracer of cloud processed air?
3. What HFo potential sources are we not accounting for in models? What does this tell us about the differences in production pathways between HFo and HAc?
4. How do HFo and HAc distributions vary based on natural and anthropogenic sources?

This dissertation presents work from two field campaigns, box models, and the Weather Research and Forecasting with coupled Chemistry (WRF-Chem) regional chemical transport model. A general caveat to the organic acid measurements presented here is the potential cofounding measurement of HAc with glycolaldehyde (GA) with our chemical ionization mass spectrometer. Manuscripts 2 and 3 address this concern in different ways; however, until a quantifiable standard can be prepared acetic acid results are presented as acetic acid equivalent sum (AAES). Manuscript 2 uses WRF-Chem results and Manuscript 3 uses measurements and Master Chemical Mechanism reactions to estimate the relative contributions of HAc and GA to AAES.

Manuscripts 1 and 2 analyzed an airmass case study, Research Flight 03 on May 21, 2012, from the Deep Convective Clouds and Chemistry Experiment (DC3). DC3 sampled summertime, mid-latitude deep convection in the United States in order to understand how deep convection impacts upper tropospheric composition and chemistry. This was accomplished by sampling active convection inflow and outflow and the upper troposphere 12-48 hours after convection. The May 21st case study was

chosen because there was higher than expected HFo by a few hundred parts per trillion (ppt) above background levels in a region dominated by convective outflow. This HFo increase suggests either transport from the boundary layer or formation within the storm and subsequent release in the outflow. A major goal of this dissertation was to understand why there was elevated HFo detected at high altitude and what this could mean for the production pathways for both acids. WRF-Chem was used in conjunction with observations to test different hypotheses explaining the observations. However, first verification of the reproducibility of the case study storm in WRF-Chem was needed which was the focus of Manuscript 1.

WRF-Chem was unable to produce a storm at the Alabama/Tennessee border without the use of a lightning data assimilation (LDA) method. Manuscript 1 discusses different combinations of cloud microphysics schemes and temperature ranges for the LDA method. This LDA method adjusts the water vapor over a set temperature range to help locate and promote convection by augmenting buoyancy. The microphysics schemes and LDA temperature ranges were evaluated for the smallest domain (0.6 km) using 5 criteria: 1) maximum-column radar reflectivity, 2) vertical wind, 3) maximum cloud top height, 4) cloud mass flux, and 4) hydrometeors' mass and number concentration. The different simulated storms were compared to observations and a previously simulated WRF-Chem storm. New simulations needed to be performed for this case study as the microphysics scheme from the previous WRF-Chem simulations was not compatible with the chemical mechanism desired to produce organic acids. The original WRF-Chem code, modified for this work, is from Dr. Yunyao Li a former student of Dr. Kenneth Pickering at the University of

Maryland. The radar data used for observational comparisons in Manuscript 1 were graciously prepared and shared by Dr. Retha Mecikalski at the University of Alabama Huntsville.

In Manuscript 2, measurements from our peroxide chemical ionization mass spectrometer (PCIMS) and WRF-Chem simulations explored different hypotheses for what caused the unexpected peak in HFo. The scavenging efficiencies of multiple soluble species were calculated for both observations and WRF-Chem including those detected by PCIMS: hydrogen peroxide, methyl hydroperoxide, HFo, HAc, and GA. Two simulated storms, isolated convection and a convective complex, were compared to see how storm structure impacts the scavenging efficiency of soluble species. The execution of Manuscripts 1 and 2 would not have been possible without the guidance of Dr. Mary Barth at NCAR. In addition, assistance in modifying the code for Manuscripts 1 and 2 was provided by Dr. Megan Bela at NOAA.

Manuscript 3 focused on the Front Range Atmospheric Pollution and Photochemistry Experiment (FRAPPÉ) field campaign. FRAPPÉ's goal was to characterize emissions on the Northern Colorado Front Range Metropolitan Area. Despite efforts to limit emissions, this region has multiple air quality ozone exceedance events in the summer. The Colorado Department of Public Health and Environment helped fund this project to understand what factors impact ozone formation in this region and if current emission standards are sufficient. Manuscript 3 looked at HFo and AAES sources and the role in ozone processing on the Colorado Front Range. Manuscript 3 discusses HFo and AAES chemical characterization using geographic and chemical partitioning of the Colorado Front Range. The geographic

regions were forest, Denver Metropolitan area, and the Greeley region which has both oil and natural gas operations (O&NG) and concentrated animal feeding operations (CAFO). Chemical classifications based on literature data were used to distinguish biogenic, urban, O&NG, and CAFO emissions. Beyond a campaign wide characterization two case study flights, August 11th and 12th, are highlighted. These two were chosen because both were forecasted to be upslope, or mountain-valley, circulation flights; however, this was only observed on August 12th. These upslope events can compound the air quality issue by transporting Front Range pollution to the mountains. Re-entrainment back into the boundary layer could bring part of the pollution back into the Front Range resulting in combining emissions from multiple days (Pfister et al., 2017). Dr. Rebecca Hornbrook provided guidance on this chapter by supplying data that wasn't publicly available and information about current chemical markers being used.

References

Barth, M. C., Kim, S.-W., Skamarock, W. C., Stuart, A. L., Pickering, K. E., & Ott, L. E. (2007). Simulations of the redistribution of formaldehyde, formic acid, and peroxides in the 10 July 1996 Stratospheric-Tropospheric Experiment: Radiation, Aerosols, and Ozone deep convection storm. *Journal of Geophysical Research*, *112*(D13), D13310-13334. https://doi.org/10.1029/2006JD008046

Le Breton, M., McGillen, M. R., Muller, J. B. a., Bacak, A., Shallcross, D. E., Xiao, P., et al. (2012). Airborne observations of formic acid using a chemical ionization mass spectrometer. *Atmospheric Measurement Techniques*, *5*(12), 3029–3039. https://doi.org/10.5194/amt-5-3029-2012

Johnson, B. J., Betterton, E. A., & Craig, D. (1996). Henry's law coefficient of formic and acetic acids. *Journal of Atmospheric Chemistry*, *24*(1), 113–119. https://doi.org/10.1007/BF00162406

Jones, B. T., Muller, J. B. A., O'Shea, S. J., Bacak, A., Le Breton, M., Bannan, T. J., et al. (2014). Airborne measurements of HC(O)OH in the European Arctic: A winter – summer comparison. *Atmospheric Environment*, *99*, 556–567. https://doi.org/10.1016/j.atmosenv.2014.10.030

Keene, W. C., & Galloway, J. N. (1984). Organic acidity in precipitation of North America. *Atmospheric Environment*, *18*(11), 2491–2497. https://doi.org/10.1016/0004-6981(84)90020-9

Keene, W. C., Galloway, J. N., & Holden, J. D. (1983). Measurements of Weak Organic Acidity in Precipitation From Remote Areas of the World. *J. Geophys. Res.*, *88*(C9), 5122–5130.

Khare, P., Kumar, N., Kumari, K., & Srivastava, S. (1999). Atmospheric formic and acetic acids: An overview. *Reviews of Geophysics*, *32*(2), 227–248. Retrieved from http://www.agu.org/pubs/crossref/1999/1998RG900005.shtml

Millet, D. B., Baasandorj, M., Farmer, D. K., Thornton, J. A., Baumann, K., Brophy, P., et al. (2015). A large and ubiquitous source of atmospheric formic acid. *Atmospheric Chemistry and Physics*, *15*(11), 6283–6304. https://doi.org/10.5194/acp-15-6283-2015

Neeb, P., Sauer, F., Horie, O., & Moortgat, G. K. (1997). Formation of

Hydroxymethyl Hydroperoxide And Formic Acid In Alkene Ozonolysis In The Presence Of Water Vapour. *Atmospheric Environment*, *31*(10), 1417–1423.

Paulot, F., Wunch, D., Crounse, J. D., Toon, G. C., Millet, D. B., DeCarlo, P. F., et al. (2011). Importance of secondary sources in the atmospheric budgets of formic and acetic acids. *Atmospheric Chemistry and Physics*, *11*(5), 1989–2013. https://doi.org/10.5194/acp-11-1989-2011

Pfister, G. G., Reddy, P. J., Barth, M. C., Flocke, F. F., Fried, A., Herndon, S. C., et al. (2017). Using Observations and Source-Specific Model Tracers to Characterize Pollutant Transport During FRAPPÉ and DISCOVER-AQ. *Journal of Geophysical Research: Atmospheres*, 510–538. https://doi.org/10.1002/2017JD027257

Reiner, T., Möhler, O., & Arnold, F. (1999). Measurements of acetone, acetic acid, and formic acid in the northern midlatitude upper troposphere and lower stratosphere. *Journal of Geophysical Research*, *104*(D11), 13943–13952. https://doi.org/10.1029/1999JD900030

Stavrakou, T., Müller, J. F., Peeters, J., Razavi, A., Clarisse, L., Clerbaux, C., et al. (2012). Satellite evidence for a large source of formic acid from boreal and tropical forests. *Nature Geoscience*, *5*(1), 26–30. https://doi.org/10.1038/ngeo1354

Talbot, R. W., Dibb, J. E., Klemm, K. I., Bradshaw, J. D., Sandholm, S. T., Sachse, G. W., et al. (1996). Chemical characteristics of continental outflow from Asia to the to the troposphere over the western Pacific Ocean during September-October 1991 : Results from PEM-West A. *Journal of Geophysical Research*, *101*(D1), 1713–1725.

Yuan, B., Veres, P. R., Warneke, C., Roberts, J. M., Gilman, J. B., Koss, et al. (2015). Investigation of secondary formation of formic acid: urban environment vs. oil and gas producing region. *Atmospheric Chemistry and Physics*, *15*(4), 1975–1993. https://doi.org/10.5194/acp-15-1975-2015

MANUSCRIPT 1

Evaluating MOZART-MOSIAC Compatible Cloud Microphysics Schemes in Conjunction with Lightning Data Assimilation for the DC3 May 21st Airmass Storm

By

Victoria Treadaway[1], Mary Barth[2], Brian Heikes[1]

To be submitted to Geosciences Model Development

---

[1]Graduate School of Oceanography

[2]National Center for Atmospheric Research

Abstract

This work evaluates the meteorological simulation of a Deep Convective Clouds and Chemistry Experiment (DC3) airmass storm case study. The coupled chemistry and aerosol mechanism, Model for Ozone And Related chemical Tracers version 4 and Model for Simulating Aerosol Interactions and Chemistry (MOZART4-MOSAIC), is required to study the transport, scavenging, and aqueous chemistry of organic acids presented in Manuscript 2. Prior simulations of this case used a parameterization of cloud microphysics which was incompatible with aqueous chemistry parameterization and the applicability of the two aqueous chemistry compatible cloud microphysics schemes, Morrison and Lin, are investigated. The use of different cloud microphysics parameterizations further required adjustment of the lightning data assimilation (LDA) procedure used in the model. In this work, the Weather Research and Forecasting (WRF) model version 3.7 was used for three domains (15 km, 3 km, and 0.6 km) with one-way nesting in combination with the Fierro LDA method. The LDA method adds water vapor to a column of air within a prescribed temperature range to help locate and promote convection by augmenting buoyancy. Three prescribed temperature ranges are evaluated here: 261-285 K, 261-288 K, and 261-291 K. The microphysics schemes and LDA temperature ranges were evaluated for the 0.6 km domain using 5 criteria: 1) maximum-column radar reflectivity, 2) vertical wind, 3) maximum cloud top height, 4) cloud mass flux, and 4) hydrometeors' mass and number concentration. The intensity and location of the simulated storm was assessed by these criteria in a comparison against ARMOR (Doppler radar) observations and previous WRF simulation of this case study. The previous simulation used WRF version 3.7 with the

WRF Single-Moment 6-Class microphysics scheme and an LDA temperature range of 261 – 285 K. A step-wise evaluation of the above criteria determined the Morrison microphysics scheme in conjunction with an LDA temperature range of 261 – 291 K best represented the case study storm.

1. Background

It has been known for decades that convection has the ability to transport boundary layer (BL) chemicals to the upper troposphere (UT) and will alter the amount of ozone in the UT (e.g., Bertram et al., 2007; Dickerson et al., 1987; Lelieveld and Crutzen, 1994). Despite the work so far we still do not know the full impact of BL chemical precursors on UT ozone formation. The amount of ozone in the UT will impact the radiative budget and the production of radical species that could remove pollutants (e.g., Barth et al., 2007; Bertram et al., 2007). Therefore, understanding the deep convective transport and transformation of ozone and its precursors will help improve the UT ozone budget.

Relative to the UT, the BL has slower wind speeds, higher humidity, and warmer temperatures shortening chemical lifetimes (Dickerson et al., 1987). If chemicals are lofted to the UT their lifetimes extend substantially and can travel thousands of kilometers impacting chemistry downwind. This could have a large impact during summer when there is a substantial amount of convection across the United States. Measurements from the Intercontinental Chemical Transport Experiment–North America 2004 campaign over the eastern United States and Canada found that 54% of the sampled air between 7.5 and 11.5 km was influenced by convection in the previous 2 days (Bertram et al., 2007).

Traditionally, chemical studies of deep convection have used insoluble tracers such as carbon monoxide and ozone (e.g. Bertram et al., 2007; Dickerson et al., 1987; Li et al., 2017). Both carbon monoxide and ozone have lifetimes longer than that of a thunderstorm making them ideal tracers to study transport through storms and downwind. As studies of convection's chemical impact increased, soluble chemical species have become more widely used. Three common chemical tracers are formaldehyde (CH_2O), hydrogen peroxide (H_2O_2), and methyl hydroperoxide (CH_3OOH). These three chemicals are important reservoirs for odd-hydrogen radicals thus impacting ozone production (Lee et al., 2000). The importance of hydrogen peroxide and methyl hydroperoxide as sources of the odd-hydrogen radicals increases in the upper troposphere because there is low water vapor (Lee et al., 2000). Furthermore, the ratio of hydrogen peroxide to methyl hydroperoxide serves as a tracer of convective outflow (Prather & Jacob, 1997). There is a greater scavenging of hydrogen peroxide within a storm cloud because the Henry's Law constant of hydrogen peroxide (8.33×10^4 M atm^{-1} at 298 K, O'Sullivan et al., 1996) is greater than methyl hydroperoxide (3.11×10^2 M atm^{-1} at 298 K, O'Sullivan et al., 1996). Formaldehyde's solubility is between the two peroxides (3.2×10^3 M atm^{-1} at 298 K, Sander, 2015).

Soluble species studies are aimed at understanding how scavenging impacts transport of soluble ozone precursors to the UT. Barth et al. (2001) modeled nonreactive, soluble species to study the impact of scavenging and how liquid versus solid or mixed phase impacted solubility. As liquid freezes it is possible that some soluble species, such as hydrogen peroxide, may be scavenged into ice during the

conversion of liquid to ice, snow, or hail (Barth et al., 2001). The other most likely possibility is that the soluble species will degas during the freezing process (Barth et al., 2001). If modeled scavenged species were degassed during conversion of liquid to solid then, regardless of solubility, it was transported to the UT (Barth et al., 2001). Modeled species with H $\geq 10^5$ M atm^{-1} were retained in snow and hail and had a scavenging efficiency of at least 50% (Barth et al., 2001).

Another important component to consider is the chemical transformation of BL chemicals within the storm cloud. Soluble species scavenged by cloud water can undergo aqueous chemistry transforming them into a different species. This eliminates the possibility of degassing the original chemical in the storm outflow. For example, in the aqueous phase formaldehyde can be oxidized to formic acid (HCOOH). Barth et al. (2007) hypothesized that formic acid could be a tracer for cloud processed air as a result of the aqueous formation from formaldehyde. Formic acid is an important contributor in establishing the pH of cloud and precipitation water. Up to 64% of the free acidity of rainwater in remote regions is controlled by formic and acetic acid (Khare et al., 1999). If formic acid is lofted to the UT, given the lifetime of 20+ days with respect to HO (Paulot et al., 2011), it could impact ozone chemistry and other photochemical processes far removed from the BL origin.

Unfortunately, there are limited measurements to date of formic acid in storm outflow to test Barth's hypothesis. During the Deep Convective Clouds and Chemistry (DC3) Experiment we sampled a plume of formic acid in a convective outflow region on May 21st, 2012 at the Alabama/Tennessee border. This was surprising given formic acid's high solubility (5.7×10^3 M atm^{-1} at 298 K, Treadaway et al., 2018) and will

serve as a test case for the possibility of formic acid as a tracer of cloud processed air in a future study (Manuscript 2).

Manuscript 2 will utilize observational data and numerical experiments together to investigate this hypothesis. In order to accomplish this chemical investigation the Weather Research and Forecasting (WRF) model will be coupled with a more extensive chemical mechanism, including aqueous chemistry, than previously used for this DC3 case (Bela et al., 2016; Li et al., 2017). Previous studies (Bela et al., 2016; Li et al., 2017) used the WRF Single-Moment 6-Class (WSM6, Hong and Lim 2006) microphysics scheme coupled to the Model for Ozone and Related chemical Tracers version 4 (MOZART-4) gas phase chemistry scheme (Emmons et al., 2010) and Goddard Chemistry Aerosol Radiation and Transport (GOCART) aerosol scheme (Chin et al., 2002). In order to simulate formic acid and the impacts of aqueous chemistry a different chemical mechanism was chosen which is only compatible with the Morrison and Lin cloud microphysics schemes. MOZART-4 is a detailed chemical mechanism for tropospheric inorganic chemistry and organic chemistry up to three carbons. When coupled with the Model for Simulating Aerosol Interactions and Chemistry (MOSAIC) sectional aerosol scheme, the MOZART-MOSAIC chemistry extends to include a detailed treatment of monoterpenes (Hodzic et al., 2014) and an updated isoprene mechanism (Knote et al., 2014), among other changes. MOZART-MOSAIC formic acid reactions and comparison to observed mixing ratios is discussed in Manuscript 2.

Li et al. (2017), in a study focusing on deep convective transport in different storm types (airmass, mesoscale, and supercell), reported that the Weather Research

and Forecasting (WRF) model could not reproduce the observed May 21st storm without the inclusion of a water vapor adjustment based on total lightning flash rate to initiate convection. The Li et al. (2017) simulations used WSM6 and the Advanced Research dynamical core (Skamarock et al., 2008). The lightning adjustment method was developed by Fierro et al. (2012) for horizontal grid scales less than 3 km. This method is a computationally inexpensive way to improve a modeled storm. We are unaware of the implementation of this method for the Lin and Morrison cloud microphysics schemes, one of which is required for our chemical study, besides Bela et al. (2016). The majority of published studies using the Fierro lightning data assimilation (LDA) method or similar (e.g. Marchand and Fuelberg 2014; Zhang et al. 2017) have used the WSM6 microphysics scheme. Fierro et al. (2016) tested Thompson cloud microphysics scheme with a modified version of the LDA method and found that, while there were more isolated reflectivity cores exceeding observed maxima by up to 10 dBZ, the results were similar to WSM6. As has been documented in a multitude of studies (e.g. Fan et al., 2015; Morrison and Milbrandt, 2011; Phoenix et al., 2017; Rajeevan et al., 2010; White et al., 2017), the choice in microphysics impacts storm development and strength. For example, Rajeevan et al. (2010) compared simulations using WSM6, Thompson, Lin, and Morrison for a severe thunderstorm observed in India. There were significant variations in the updraft and downdraft cores, the hydrometeor profiles, and amount of surface rainfall depending on the microphysics scheme.

The objective of this work is to determine how to best replicate the May 21st storm with either Morrison or Lin, currently the only two MOZART-MOSAIC

compatible cloud microphysics schemes. In addition, two different temperature ranges are evaluated for the water vapor adjustment using Morrison. In Section 2 the WRF model set-up, LDA method, and observational data sources are described. Section 3 provides a brief overview of the observed May 21st storm. Section 4 compares Morrison and Lin to observations and Li et al. (2017) and discusses the influence that the LDA temperature range has on simulated storms. The majority of the work presented is without chemistry included. The inclusion of chemistry into the model altered the storm compared to the meteorology only simulations. Section 5 briefly explores how the storm changed after chemistry was added.

2. Methods

2.1 Model Set-Up

This study used the Weather Research and Forecasting (WRF) model version 3.7 with the Advanced Research WRF dynamical core (Skamarock et al., 2008) for simulations of the May 21st Alabama airmass storm. Simulations were run with one-way nesting for three domains with 15 km, 3 km, and 0.6 km horizontal resolutions (Fig. 1.1). There were 40 vertical levels with a model top of 70 hPa. The time step for each domain was 75 s, 15 s, and 3 s, respectively. The simulations were performed from 15:00 – 22:00 UTC using initial and boundary conditions from 3-hourly time resolution Global Forecast System (GFS) analysis (https://www.ncdc.noaa.gov/data-access/model-data/model-datasets/global-forcast-system-gfs).

Besides the microphysics, the WRF set-up replicated the previous work of Bela et al. (2016) and Li et al. (2017) that tested different parameterizations in order to accurately represent the observed storm. The 15 km domain used the Grell 3D

cumulous parameterization (Grell, 1993; Grell & Dévényi, 2002). The Yonsei University (YSU) scheme was used to simulate planetary boundary layer (PBL) mixing in all three domains (Hong et al., 2006). The RRTMG shortwave and longwave radiation schemes (Iacono et al., 2008) and the Noah land-surface parameterization (Koren et al., 1999) were used for all three domains.

2.2 Lightning Data Assimilation Method

The lightning data assimilation (LDA) technique used was developed by Fierro et al. (2012; 2014; 2015) and modified by Li et al. (2017). This technique nudges the water vapor based on flash counts and graupel. The Buck (1996) water vapor saturation pressure equation was used as that was similar to the internal WRF Q_{sat} calculation. Fierro et al. (2012) originally adjusted the water vapor between 253 to 273 K. Li et al. (2017) modified this range to 261 – 285 K thereby improving the vertical scale of the modeled storm. This was based on suggestions that lowering the temperature range to include the boundary layer may better represent weakly forced deep convection (Fierro et al., 2015; Marchand & Fuelberg, 2014). As will be discussed below, the 261 – 285 K temperature range was insufficient to reproduce the vertical extent observed. Therefore, the temperature range was increased further to 261 – 288 K to root the storm in the boundary layer. This work compares the Li et al. (2017) and modified temperature range using Morrison.

Lightning data came from the North Alabama Lightning Mapping Array (NALMA) very high frequency (VHF). The LDA adjustment occurred only if the minimum flashes were greater than 5 per 10 min. A dampening option was also used to suppress convection outside the region of interest. Prior to convection initiation,

from 17:00-19:00 UTC, the relative humidity was reduced to 75% throughout the domain to prevent the formation of spurious storms (Li et al., 2017).

2.3 Model Microphysics Options

This study compared two WRF-Chem MOZART-MOSAIC compatible microphysics schemes: Lin et al. and Morrison double-moment. The Lin et al. scheme was introduced by Lin et al. (1983) and Rutledge and Hobbs (1984). Lin was modified for WRF using the Purdue cloud model described in Chen and Sun (2002). Lin is a single-moment scheme with mass variables (mixing ratio) for six hydrometeors (water vapor, cloud water, rain, cloud ice, snow, and graupel). The Morrison double-moment scheme (Morrison et al., 2009) also has six hydrometeor classes (water vapor, cloud water, rain, cloud ice, snow, and graupel/hail). Like Lin, Morrison predicts the mixing ratio for all six hydrometeors. In addition, Morrison predicts the number concentration for cloud drops, rain, cloud ice, snow, and graupel/hail. This work treats dense precipitating ice as hail instead of graupel. The hail option uses a fall speed of 0.9 g/cm^3 while graupel uses 0.4 g/cm^3 (Morrison et al., 2005).

2.4 *Observational Data Sources*

Radar observations are from the Next Generation Weather Radar (NEXRAD) Weather Surveillance Radar-1988 Doppler (WSR-88D) stationed at Hytop, Alabama (KHTX) and the Advanced Radar for Meteorological and Operational Research (ARMOR). ARMOR is operated by the University of Alabama in Huntsville (UAH). The maximum radar reflectivity profiles are the maximum merged ARMOR-KHTX horizontal radar reflectivity. The radar composites have a 1 km horizontal resolution and a vertical grid spacing of 1 km. The three-dimensional radar composites and

vertical velocity were prepared using the methods outlined in Mecikalski et al. (2015). The mass flux calculation used sounding data collected by the UAH Mobile Radiosonde Observation Data (RAOB). The radiosonde used was launched on May 21st at 20:37 UTC near Capshaw, Alabama (86.794^{o} W, 34.806^{o} N).

3. Observational Description of the Storm

The May 21st storm has been described extensively in Mecikalski et al. (2015), Barth et al. (2015), Bela et al. (2016;2018), Fried et al. (2016), and Li et al. (2017) and will only be discussed briefly here. There were two rounds of deep moist convection on May 21st in the DC3 Alabama domain (Mecikalski et al., 2015). The storm of interest started in Tennessee as two separate updrafts at 19:45 UTC with a third storm on the Alabama/Tennessee border. At 20:04 UTC (Fig. 1.2a) the northern storm had its first lightning flashes though no lightning was detected in the southern storm until the two merged (Mecikalski et al., 2015). At 20:15 UTC (Fig. 1.2b) the two storms merged into one, commonly called B2, resulting in an increase in lightning and vertical motion (Mecikalski et al., 2015). By 20:20 UTC (Fig. 1.3a) the maximum velocity was 12 m/s and was in the -10^{o}C layer. The peak flash rate was at 20:23 UTC and the storm started to collapse after 20:30 UTC (Fig. 1.2c) (Mecikalski et al., 2015). The vertical motion formed a wedge that sloped from west to east likely due to the surface outflow moving faster than the main convection line and a strong cold pool (Li et al., 2017; Mecikalski et al., 2015). By 20:50 UTC (Fig. 1.2d) B2 merged with the southern storm to form a ring-shaped convective complex.

4. Results and Discussion

This work confirmed that both Morrison and Lin required the LDA water vapor adjustment to produce a storm in the region (Fig. 1.3). Even with the lightning data, the simulated storms generated about 30 minutes later than the observed storm. This work compares three simulations: Morrison with LDA applied from 261 – 285 K (hereafter M285), Lin with LDA applied from 261 – 285 K (hereafter L285), and Morrison with LDA applied from 261 – 288 K (hereafter M288).

4.1 Horizontal Radar Reflectivity

The column-maximum radar reflectivity profiles for the three WRF simulations are in Figs 1.4-1.6. For M285, the two storms that merged to form B2 first appeared at 20:30 UTC (Fig. 1.4a) and B2 formed by 20:50 (Fig. 1.4b). As the storm moved south, it elongated to the north forming a "tail" that remained as the storm decayed. There was also the storm on the Alabama/Tennessee border as seen in observations. By 21:30 UTC there was a cluster of storms at the border but not the observed ring-shaped convective complex.

L285 column-maximum radar reflectivity (Fig. 1.5) contained scattered background reflectivity (less than 10 dBZ) in the surrounding area that was not present with Morrison. Unlike M285, the two initial storms appeared at 20:20 UTC (Fig. 1.5a) though much weaker than the initial appearance in M285 (20:30 UTC). By 20:30 UTC the storms' reflectivities were similar to M285 and the two storms fully merged by 20:50 UTC (Fig. 1.5b). As B2 decayed and moved towards the southeast it formed a ring shape similar to the observed storm (Fig. 1.5e) though it did not merge with the surrounding storms like observed. L285 formed a similar elongated shape as M285 to the north as the storm decayed.

M288 had the highest reflectivity of the three simulations (Fig. 1.6). Like M285, the two storms appeared at 20:30 UTC (Fig. 1.6a) though M288 was larger. By 20:40 UTC the two merged but there were clearly two storm cores with reflectivity greater than 55 dBZ (Fig. 1.3c). The two cores fully merged by 20:50 UTC (Fig. 1.6b). M288 produced a larger and stronger storm than either M285 or L285 though the characteristic northern "tail" was present. The border storm was also larger than either of the other simulations. Unlike M285 and L285, M288 did not form a ring as the storm decayed. Instead, smaller storms, with reflectivity greater than 50 dBZ, formed on the edges of B2 (Fig. 1.6c) resulting in a cluster of small storms and the original B2 was lost.

Overall, L285 was the only simulated storm to form a ring with surrounding storms as it decayed. This is likely helped by the presence of spurious smaller storms in the area. M285 stayed as isolated convection during its decay. M288 created smaller storms near B2 as it decayed but the convection was scattered and never formed a ring.

4.2 Vertical Radar and Wind Cross-Sections

ARMOR reflectivity and vertical wind (w) for 20:20 UTC in Fig. 1.7 represents a snapshot during the peak time of B2 (Mecikalski et al., 2015). The panels are oriented the same as WRF but the cross-sections are not the same length. The cross-sections are spaced 1 km apart and the south-north transects covered 30 km while west-east covered 25 km. This was to keep the similar storm analysis box used in Mecikalski et al. (2015). Figure S1.1 shows multiple panels in both directions to show the observed storm structure. The maximum reflectivity was less than 60 dBZ

and w was 12 m/s. The storm topped at 12 km and was about 10 km wide. The maximum reflectivity reached the surface. The wind contours wedged in the south-north direction.

Figures 1.8-1.10 are WRF vertical cross-sections of reflectivity and vertical velocity at 20:50 UTC. WRF comparisons are done at 20:50 UTC as that was the first time with B2 for all three storms. The top panel shows the south-north transect through the core of column maximum radar reflectivity (transects shown in Figs. 1.4-1.6) and the bottom panel shows the west-east transect. Both cross-sections are equidistant (18 km). In Figs. S1.2- S1.4 are multiple transects spaced 1.2 km apart in both directions highlighting the structure of the storms. An example of the transect layout is shown in Fig. S1.5 for Lin.

L285 (Fig. 1.8) had the lowest maximum reflectivity (less than 55 dBZ). The maximum reflectivity was not at the surface but from 1 – 3 km. The maximum vertical extent was less than 10 km and the maximum storm width was 8.5 km (Fig. 8 top panel, dBZ > 35). The wind formed a wedge from south to north with a maximum of 10 m/s. M285 (Fig. 1.9) had a maximum reflectivity greater than 60 dBZ though again not at the surface though it did have reflectivity greater than 55 dBZ at the surface. A similar vertical wind wedge formed in the south-north transects and the maximum w was 12 m/s. In the west-east transect there were still two vertical motion cores corresponding with the irregular shape of the storm core in Fig. 1.4. M285 was 9 km wide at its maximum reflectivity center (Fig. 1.9 top panel) and the maximum vertical extent was 9 km. M285 at 20:40 UTC (not shown) had a higher reflectivity in the core (greater than 60 dBZ) but this is before the full formation of B2 as indicated in Fig.

1.4b. M288 clearly produced the strongest storm (Fig. 1.10). Unlike M285 and L285, the vertical extent of the storm reached 12 km. M288 had the highest w (32 m/s) of the three simulations and reflectivity greater than 65 dBZ The storm was about 12 km wide in all transects, the largest of the three WRF runs, which isn't surprising based on the horizontal column maximum reflectivity profiles. In the west-east cross-sections multiple vertical motion cores were present. At 20:50 UTC, M288 did not have the south-north wedge present in L285 and M285.

4.3 Cloud Top Height, Maximum Vertical Motion, and Storm Core Volume

It is essential to use other parameters, besides radar images, to compare the simulated and observed storm. Figure 1.11 shows the cloud top height (km), maximum vertical wind (w_{max}, m/s), and the 35 dBZ volume (m^3) for the Morrison and Lin simulations, the Li et al. (2017) WSM6 simulation, and ARMOR observations. This encompasses the B2 storm for the time period that includes the two storms that formed B2 and follows B2 through its lifetime. As the storms moved, L285 and M285 remained as isolated storms longer than M288. It is not possible to distinguish the M288 B2 from other storms in the region after 21:10 UTC. For this reason, the M288 time series ends before the other two simulated storms.

The cloud top height (Fig. 1.11a) is defined as the maximum height of grid cells with reflectivity greater than 20 dBZ. Both M285 and L285 reached 10 km or less while M288 reached a similar cloud top height to observed (12 km) by 20:40 UTC as seen in the vertical cross sections (Figs. 1.8-1.10). M288 had a w_{max} double that of the other simulations and observed storm with a maximum of 32 m/s at 20:50 UTC (Fig. 1.11b). The second increase in M288 w_{max} to 17 m/s at 21:10 UTC could be

caused by two small storms that formed to the west of B2. The observed storm has a peak w_{max} of 17 m/s just before the storm's decay (Mecikalski et al., 2015). For the majority of observed B2's lifetime the w_{max} was 10 – 13 m/s. The 35 dBZ volume (Fig. 1.11c) is defined as the volume of grid cells of the storm with reflectivity equal to or greater than 35 dBZ. This is used as a proxy for graupel/hail. Overall M288 had the largest 35 dBZ volume. M285 and L285 had similar volumes as the observed storm.

Data from Li et al. (2017) show that, for the May 21st storm, the WSM6 results were similar to M288. The WSM6 maximum cloud top height was 13 km and w_{max} was 32 m/s. The WSM6 35 dBZ volume (~$5.6x10^{12}$ m^3) was larger than M288. Unlike M288, the WSM6 and observed storms formed around the same time. B2 merged with the surrounding storms by 21:00 UTC thus the time series stops at 20:50 UTC to ensure only B2 is represented.

Figure 1.11 highlights the different storm start times observed in Figs. 1.4-1.6. The initial convection in L285 began at 20:20 UTC while Morrison initial convection began at 20:30 UTC. Though the L285 simulated cloud appeared first, the three simulated storms' updraft started at the same time (20:10 UTC). This implies that the LDA increase in water vapor resulted in a similar timing in the initial perturbation in the virtual potential temperature leading to the updraft (Fierro et al., 2012). Lin cloud microphysics scheme responded faster to the injection of additional water vapor and formed a cloud. All three storms initiation times were delayed relative to the observed storm by about 30 minutes. This is likely an effect of the assimilation method. Adding water vapor based on observed lightning strikes requires the observed storm to have

developed enough to produce lightning. If there is no simulated storm present without adding additional water vapor, as opposed to just enhancing a weakly simulated storm, the simulated storm will be delayed relative to observations. Future users may want to consider changing the timing of the LDA based adjustments.

4.4 Cumulus Updraft Mass Flux

Since the goal of Manuscript 2 is to use modeled aqueous chemistry to study chemical fate and transport through this storm it is important to reasonably estimate the mass flux through the storm. The mean cumulus updraft mass flux for storm B2 was calculated for the WRF simulations and the observed storm (Fig. 1.12). The B2 updraft mass flux (humid air density x vertical velocity) was summed for all grid points with a vertical velocity greater than 1 m/s and reflectivity greater than 20 dBZ and divided by grid area. This accounts for the different storm sizes for the simulations and observation. To calculate the density for the observed storm the UAH sounding at 20:37 UTC was used along with the ARMOR vertical velocity. Because this sounding was taken as the storm decayed this serves as an estimation of mass flux. On each plot the 0^{o}C (blue), -10^{o}C line (red), and -20^{o}C line (green) are shown for reference.

ARMOR cumulus mass fluxes are shown in Fig.1.12a from 20:15 to 20:37 UTC which corresponds to the peak time for B2. The greatest observed mass flux occurred just after the two cores merged to form B2 (4.1 kg $m^{-2}s^{-1}$) and the maximum decreased 25% by 20:23 UTC. The observed maximum altitude with mass flux greater than zero was at 20:23 UTC (13 km). M285 and L285 mass fluxes for storm B2 were calculated from 20:50 – 21:10 UTC (Fig. 1.12b and Fig. 1.12d, respectfully). The mass flux for both M285 and L285 were zero in parts of the profile by 21:10 UTC.

There is clearly no entrainment from the surface by this point as B2 matured and decayed. The M285 maximum mass flux at 20:50 UTC (3.3 kg $m^{-2}s^{-1}$) was similar in magnitude to L285 (3.5 kg $m^{-2}s^{-1}$) though 1.2 km lower. L285 and M285 upward mass flux decreased 43% and 30%, respectively, from 20:50 to 21:00 UTC. Both L285 and M285 mass fluxes were zero before 10 km corresponding to the 10 km maximum cloud top height. The mass flux for M288 was calculated from 20:50 – 21:00 UTC. By 21:10 UTC B2 had decayed and spurious storms in the same region were forming (Fig. 1.6). M288 had the greatest mass flux of all the simulations and largest vertical extent. The mass flux maximum and vertical extent of 4.4 kg $m^{-2}s^{-1}$ (20:50 UTC) was similar to observations. M288 had a 27% decrease from 20:50 to 21:00 UTC which is comparable to the other simulations. The M288 transition from convergence to divergence was at the highest altitude (8 km) though there was also a peak at 4 km similar to ARMOR and the other simulations.

The varying mass flux maximum peaks for the WRF simulations were a function of the changing area meeting the criteria (Fig. 1.13). ARMOR (at 20:23 UTC) had the greatest storm area meeting the criteria while all three storms had substantially smaller areas (Fig. 1.13). M288 had the largest area meeting the criteria of the three simulations. The shape of the area meeting the criteria results in the multiple mass fluxes peaks observed for the simulations leading to the multiple peaks in the mass flux for the simulations. For example, the M285 and M288 peak below 2 km is reflected in the area plot.

4.5 Water Hydrometeors

A final comparison shows how water is divided between the hydrometeors for the different meteorological set-ups. WRF reports ice, snow, graupel/hail, cloud water, and rain (g/kg for all). The graupel/hail hydrometeor represents graupel for L285 and hail for M285 and M288. The hydrometeor maximum for B2 is shown from 20:00 UTC to 21:00 UTC in Fig. 1.14. Using the maximum value represents the dominant hydrometeor at a given model time and shows trends between the set-ups. Total condensed water (q_{total}) is the sum of cloud water, rain, ice, snow, and graupel/hail. Please note that q_{total} shows maximum of the sum and not the sum of the maximums. As there is no possible quantitative comparison for ARMOR, the maximum hydrometeors are compared to the WSM6 data from Li et al. (2017). WSM6 has the same hydrometeor categories as L285. As mentioned in Section 4.3, the end times for the simulations differ depending on when B2 could confidently be sampled independently from surrounding storms.

WSM6 and L285 had nearly indistinguishable ice, rain, and cloud maximums once L285 matured. Both WSM6 and Lin are single moment schemes which could explain the comparable category maximums with the exception of snow. WSM6 had a greater snow maximum mixing ratio (4 g/kg) than Morrison or Lin. L285 had the smallest overall snow maximum (0.15 g/kg). M288 and WSM6 had similar q_{total} maximums. Since M288 was substantially stronger than L285 and M285 there would be more time to grow particles to hail which is why the M288 hail maximum is greater than L285 and M285. As seen in Fig. 1.11, WSM6 developed first explaining the q_{total} greater than zero at 20:00 UTC. WSM6 and M288 had practically indistinguishable graupel/hail maximums from 20:30 to 20:50 UTC however M288 treated the graupel

category as hail. When using the hail option the fall speed increases because the Morrison bulk density of hail is 0.9 g/cm^3 compared to 0.4 g/cm^3 for graupel (Morrison et al., 2005). This analysis does not account for altitude differences; therefore, the high M288 hail maximum is likely much closer to the ground than the graupel maximum in WSM6.

Overall, M288 had the highest maximums in each category of the Morrison and Lin simulations. This is expected as M288 added water vapor over the largest temperature range, corresponding to the greatest number of grid cells. The different microphysics schemes also clearly impact how water is divided among the hydrometeors. M285 and L285 had nearly identical q_{total} maximums; however, they did not partition the water among the categories in a similar way. M285 started with a higher cloud maximum though by 20:40 UTC they were comparable. L285 had a higher graupel maximum than M285 for the duration of B2's lifetime. The heavier hail in M285 would fall and rain out potentially explaining M285's higher rain maximum earlier in the storm. This discussion highlights how different microphysics schemes partition water vapor among hydrometeors. The similarities between L285 and WSM6 can be attributed to both being single moment schemes.

5. Meteorological Versus Chemical Simulations

Of the three simulations discussed above, M288 best captured the horizontal and vertical structure of the storm as well as the total mass transport through the storm. Since the ultimate objective was to use WRF-Chem with MOZART-MOSAIC it was important to confirm that adding the chemistry module did not significantly impact the storm structure. The addition of chemistry adds an aerosol scheme which

allows for a more complex interaction between radiation and aerosols which could impact the storm structure. The WRF-Chem run with M288 produced a simulated storm that was weaker than M288 and in fact more reflected M285 in horizontal size and storm strength. It is possible that aerosols impacted the radiation strongly enough to dampen the storm. However, after running with and without aerosol direct effects there was minimal improvement in storm strength.

Due to the similarity to M285 we increased the LDA temperature adjustment range another 3 K (261 K to 291 K) into the boundary layer to see if that strengthened the storm. This improved the storm structure, better reflecting the M288 meteorological simulation. This suggests that there were potential dampening effects in the chemistry run not present in the meteorological run involving interactions between aerosols, chemistry, and radiation. Aerosol-radiation interactions impact the sensible and latent heat fluxes which impacts the thermodynamic structure of the atmosphere. Furthermore, with an aerosol scheme there are aerosol-cloud interactions that will impact cloud condensation nuclei concentrations.

When chemistry was included, other storms appeared in the 0.6 km domain that were not present in the meteorological simulation including a squall line near the western boundary. This suggests that the baseline conditions were different for the chemistry and meteorological simulations. In general, the water vapor adjustment is not applied if the relative humidity is greater than 93%. It is assumed that above this relative humidity a storm would form “naturally” and not need the additional water vapor. The chemistry simulation had a vertical layer (around 2.5 km) with relative humidity greater than 90% adjacent to B2 that was not present in the meteorological

run. It is possible the adjacent peak in relative humidity altered the B2 storm region enough that a smaller amount of water was being added with the chemistry run because, in theory, the relative humidity was high enough to produce the storm. However, because B2 was not formed without the LDA addition the amount of water added with the M288 chemistry run was insufficient to root the storm in the boundary layer thus producing a similar storm to M285. The M288 chemistry simulation had half the total condensed water (q_{total}) maximum as M288 and M291 with chemistry.

For LDA to be effective and reproduce B2 it needed a larger addition of water vapor to increase the buoyancy even more than the meteorological run. This is likely due to aerosol effects. With only meteorology, particles had a prescribed number and size distribution. When chemistry is added, the emissions and chemistry impact the number, composition, and size distribution of the aerosols. WRF-Chem passes the cloud droplet number source (resulting from aerosol activation) and cloud droplet number between the chemistry and physics modules (Chapman et al., 2009). Not using aerosol direct effects slightly improved the simulation though not substantially. It is possible that indirect effects or other chemical and meteorological interactions impacted the overall domain making it more challenging for the LDA adjustment to root the storm in the BL.

Furthermore, there were unforeseen interactions with the addition of observed formic acid (HFo). WRF-Chem HFo mixing ratio was two orders of magnitude lower than observed. Aircraft HFo data was implemented into WRF-Chem to evaluate HFo scavenging (Manuscript 2) following the approach of Bela et al. (2016). Peroxide chemical ionization mass spectrometer HFo median altitude profiles in the boundary

layer and free troposphere were used as the HFo altitude profile implemented into WRF-Chem. The boundary layer was defined as altitude $\leq$ 2 km and q_{total} < 0.01 g/kg from 21:00 – 22:00 UTC which was during a spiral before returning to base. The free troposphere was defined as altitude > 3km, q_{total} <0.01 g/kg, and O_3/CO<1.25 with aircraft data from 17:00-19:00 UTC which was before the storm sampling. The lowest altitude median HFo value was applied to all layers below available GV measurements down to the surface. The chemistry of these simulations is discussed in detail in Manuscript 2. This change was implemented into the WRF boundary files and the WRF restart file at 19:00 UTC.

The WRF-Chem simulation with LDA adjustment from 261 – 291 K and the aircraft HFo mixing ratio is referred to as M291-Chem. Since this version will be used in Manuscript 2 it is important to understand how this version of the storm compares to observations. The structure and timing of M291-Chem differed from the above discussed simulated storms. The critical understanding for M291-Chem is how this storm impacts the chemical transport through the storm in order to evaluate different hypotheses explaining the elevated HFo near storm outflows. A brief discussion is presented with 4 of the criteria discussed above: 1) maximum-column radar reflectivity, 2) vertical wind, 3) maximum cloud top height, and 4) cloud mass flux. This comparison focuses on ARMOR and M291-Chem during the outflow period (20:50 – 21:14:30 UTC) defined in Bela et al. (2016), Fried et al. (2016), and Li et al. (2017). This differs from the above discussion that focused on the formation of B2 and how WRF compared to observations in forming the desired storm.

Figure S1.6 shows ARMOR maximum-column radar reflectivity for 20:51, 20:59, 21:06, and 21:14 UTC. These are roughly every 10 minutes during the outflow period to match the WRF-Chem output time period. The convective complex discussed above is present but decaying. There is at least one cell with reflectivity greater than 55 dBZ throughout the outflow period. M291-Chem is similar to the meteorology simulations where the storm developed later than observed. The period from 21:30-21:50 UTC (Fig. S1.7) starts as a storm cluster and the different cells merge with one dominant cell with reflectivity greater than 60 dBZ though there are still a couple other smaller complexes within the system. The box in Fig. S1.6 represents the area used to calculate the parameters in Fig. 1.15. Figure 1.15 shows the cloud top height, w_{max}, and 35 dBZ volume described in Section 4.3 for ARMOR and M291-Chem with arbitrary time units for the different outflow periods. This differs slightly from the ARMOR used in Fig.1.11 because that included just B2.The cloud top height is higher for ARMOR but the w_{max} and 35 dBZ volume are higher for M291-Chem. The w_{max} is more similar between ARMOR and M291-Chem than with the M288 meteorological simulation. The M291-Chem 35 dBZ volume is closer to the M288 than ARMOR.

Despite the differences in storm structure compared to ARMOR and the simulations discussed above the mass flux was similar to observed. The M291-Chem mass flux had a similar maximum flux to the later portions of ARMOR B2 after 20:30 UTC in Figure 1.12. The transition between convergence and divergence was at a similar altitude to ARMOR at 20:30 UTC. This is before the observed outflow period. The outflow period ARMOR cumulus updraft mass flux is compared to M291-Chem

in Fig. 1.16. This comparison is important when considering the transport through a storm and scavenging efficiency in Manuscript 2. The same outflow times are shown as in Figs. S1.5 and S1.6. Despite the higher cloud top height in Fig. 1.15 there is no mass flux above 6 km for ARMOR. Overall, the ARMOR mass flux decreased with altitude and is half of the M291-Chem flux. The sampled outflow period was likely not directly from the surface. There is cumulus mass flux up to almost 10 km for M291-Chem. The difference between the cloud top height and mass flux tops for ARMOR relates to vertical velocity. There must be part of ARMOR with reflectivity greater than 20 dBZ, a factor for mass flux and cloud top height, but vertical velocity less than 1 m/s. Therefore, the cumulus mass flux is lower than the cloud top height.

During a review on the status of atmospheric modeling in Europe, Baklanov et al. (2014) discussed the need to improve our conceptual understanding of the aerosol-radiation-cloud-chemistry interactions. As more is understood about these interactions the modeled parameterizations will also need to be improved. Baklanov et al. (2014) cautioned that as more chemistry and meteorological parameters are added we need to be aware of how these will affect each other. Feedbacks between chemistry, radiation, and aerosols for WRF-Chem with MOZART-MOSAIC appear to have altered the meteorology of the domain. A more extensive exploration of this interaction for the May 21st case is beyond the scope of this work. However, as discussed here, when data assimilation is required to produce a storm it is possible that even more energy is needed to overcome the natural interactions between chemistry, aerosols, and meteorology.

6. Summary

WRF simulations were performed with Morrison and Lin microphysics schemes to replicate the DC3 May 21st airmass storm at the Alabama-Tennessee border. In order to produce a storm in the region with WRF a LDA method was needed that added water vapor in a defined temperature range. Originally, the Morrison and Lin simulations were performed over the temperature range 261 – 285 K to replicate WSM6 simulations in Li et al. (2017) and Bela et al. (2016). This resulted in a storm with a similar maximum vertical velocity and radar reflectivity to the observed storm. However, the cloud top (10 km) was lower than observed (12 km) and there was a smaller cumulus mass flux. The LDA temperature range was extended from 285 K to 288 K for Morrison resulting in a cloud top height within 1 km of observations. However, the maximum vertical wind was overestimated by 18 m/s. Clearly extending the temperature region to 288 K made the simulated storm too vigorous. Despite the differences to the observed storm, it produced a similar storm to the WSM6 simulations based on the 35 dBZ volume, cloud top height, and maximum vertical velocity.

As the goal of this study was to simulate the chemical transport through this storm, the amount of mass being moved through the storm was important. M285 and L285 had similar maximum mass fluxes. M288, because of its higher cloud top height, was the only simulated storm to have mass flux reach 12 km, like observed. None of the WRF simulations produced a perfect replica of the observed May 21st storm. Of the options available M288 did the best at capturing the horizontal and vertical

structure of the storm as well as the total mass transport through the storm. M288 also best reflected previously published WRF work using WSM6.

A final adjustment was made with the addition of chemistry. M288 used with the MOZART-MOSAIC chemistry set-up resulted in a storm that was weaker than the meteorological M288 run. The chemical M288 simulation produced a similar storm to M285; therefore, the LDA temperature region was increased another 3 K (261 – 291 K) in order to provide more energy to the system. Adjusting the temperature range improved the vertical extent but with the addition of chemistry and observed formic acid the storm structure changed. Understanding the reasons for the change in storm structure are outside the scope of this work but highlight the complicated interplay between chemistry, aerosols, and meteorology. In part it is clear that additional water vapor was required to overcome the WRF-Chem dampening effects that result from the interplay of chemistry, aerosols, and meteorology. The WRF-Chem storm with the chemistry modifications had a similar maximum vertical velocity to ARMOR but with a slightly lower cloud top height. The M291-Chem cumulus mass flux was in the range of the ARMOR B2 storm and higher than the mass flux during the outflow period. Manuscript 2 will use Morrison with an LDA adjustment from 261 – 291 K

References

Baklanov, A., Schlünzen, K., Suppan, P., Baldasano, J., Brunner, D., Aksoyoglu, S., Carmichael, G., Douros, J., Flemming, J., Forkel, R., Galmarini, S., Gauss, M., Grell, G., Hirtl, M., Joffre, S., Jorba, O., Kaas, E., Kaasik, M., Kallos, G., Kong, X., Korsholm, U., Kurganskiy, A., Kushta, J., Lohmann, U., Mahura, A., Manders-Groot, A., Maurizi, A., Moussiopoulos, N., Rao, S. T., Savage, N., Seigneur, C., Sokhi, R. S., Solazzo, E., Solomos, S., Sørensen, B., Tsegas, G., Vignati, E., Vogel, B. and Zhang, Y.: Online coupled regional meteorology chemistry models in Europe: Current status and prospects, Atmos. Chem. Phys., 14(1), 317–398, doi:10.5194/acp-14-317-2014, 2014.

Barth, M. C., Stuart, A. L. and Skamarock, W. C.: Numerical simulations of the July 10, 1996, Stratospheric-Tropospheric Experiment: Radiation, Aerosols, and Ozone (STERAO)-Deep Convection experiment storm: Redistribution of soluble tracers, J. Geophys. Res., 106(D12), 381–400, 2001.

Barth, M. C., Kim, S.-W., Skamarock, W. C., Stuart, A. L., Pickering, K. E. and Ott, L. E.: Simulations of the redistribution of formaldehyde, formic acid, and peroxides in the 10 July 1996 Stratospheric-Tropospheric Experiment: Radiation, Aerosols, and Ozone deep convection storm, J. Geophys. Res., 112(D13), D13310-13334, doi:10.1029/2006JD008046, 2007.

Barth, M. C., Cantrell, C. A., Brune, W. H., Rutledge, S. A., Crawford, J. H., Huntrieser, H., Carey, L. D., MacGorman, D., Weisman, M., Pickering, K. E., Bruning, E., Anderson, B., Apel, E., Biggerstaff, M., Campos, T., Campuzano-Jost, P., Cohen, R., Crounse, J., Day, D. A., Diskin, G., Flocke, F., Fried, A., Garland, C., Heikes, B., Honomichl, S., Hornbrook, R., Huey, L. G., Jimenez, J. L., Lang, T., Lichtenstern, M., Mikoviny, T., Nault, B., O'Sullivan, D., Pan, L. L., Peischl, J., Pollack, I., Richter, D., Riemer, D., Ryerson, T., Schlager, H., Clair, J. St., Walega, J., Weibring, P., Weinheimer, A., Wennberg, P., Wisthaler, A., Wooldridge, P. J. and Ziegler, C.: The Deep Convective Clouds and Chemistry (DC3) Field Campaign, Bull. Am. Meteorol. Soc., doi:10.1175/BAMS-D-13-00290.1, 2015.

Bela, M. M., Barth, M. C., Toon, O. B., Fried, A., Homeyer, C. R., Morrison, H., Cummings, K. A., Li, Y., Pickering, K. E., Allen, D. J., Yang, Q., Wennberg, P. O., Crounse, J. D., St Clair, J. M., Teng, A. P., O'Sullivan, D., Huey, L. G., Chen, D., Liu, X., Blake, D. R., Blake, N. J., Apel, E. C., Hornbrook, R. S., Flocke, F., Campos, T. and Diskin, G.: Wet scavenging of soluble gases in DC3 deep convective storms using WRF-Chem simulations and aircraft observations, J. Geophys. Res. Atmos., 121(8), 4233–4257, doi:10.1002/2015JD024623, 2016.

Bela, M. M., Barth, M. C., Toon, O. B., Fried, A., Ziegler, C., Cummings, K. A., Li,

Y., Pickering, K. E., Homeyer, C. R., Morrison, H., Yang, Q., Mecikalski, R. M., Carey, L., Biggerstaff, M. I., Betten, D. P. and Alford, A. A.: Effects of Scavenging, Entrainment, and Aqueous Chemistry on Peroxides and Formaldehyde in Deep Convective Outflow Over the Central and Southeast United States, J. Geophys. Res. Atmos., 123(14), 7594–7614, doi:10.1029/2018JD028271, 2018.

Bertram, T. H., Bertram, T. H., Perring, A. E., Wooldridge, P. J., Crounse, J. D., Kwan, A. J., Wennberg, P. O., Scheuer, E., Dibb, J., Avery, M., Sachse, G., Vay, S. A., Crawford, J. H., Mcnaughton, C. S., Clarke, A., Pickering, K. E., Fuelberg, H., Huey, G. and Blake, D. R.: Direct Measurements of the Convective Recycling of the Upper Troposphere, Science (80-.)., 315(5813), 816–820, doi:10.1126/science.1134548, 2007.

Buck, A.: Buck research instruments Appendix 1, [online] Available from: http://www.hygrometers.com/wp-content/uploads/CR-1A-users-manual-2009-12.pdf, 1996.

Chapman, E. G., Gustafson, W. I., Easter, R. C., Barnard, J. C., Ghan, S. J., Pekour, M. S. and Fast, J. D.: Coupling aerosol-cloud-radiative processes in the WRF-Chem model: Investigating the radiative impact of elevated point sources, Atmos. Chem. Phys., 9(3), 945–964, doi:10.5194/acp-9-945-2009, 2009.

Chin, M., Ginoux, P., Kinne, S., Torres, O., Holben, B. N., Duncan, B. N., Martin, R. V., Logan, J. A., Higurashi, A. and Nakajima, T.: Tropospheric Aerosol Optical Thickness from the GOCART Model and Comparisons with Satellite and Sun Photometer Measurements, J. Atmos. Sci., 59(3), 461–483, doi:10.1175/1520-0469(2002)059<0461:TAOTFT>2.0.CO;2, 2002.

Dickerson, R. R., Huffman, G. J., Luke, W. T., Nunnermacker, L. J., Pic, K. E., Leslie, A. C. D., Lindsey, C. G., Slinn, W. G. N., Kelly, T. J., Daum, P. H., Delany, A. C., Greenberg, J. P., Zimmerman, P. R., Boatman, J. F., Raw, J. D. and Stedman, D. H.: Thunderstorms: An Important Mechanism in the Transport of Air Pollutants, Science (80-.)., 235(4787), 460–465, 1987.

Emmons, L. K., Walters, S., Hess, P. G., Lamarque, J. F., Pfister, G. G., Fillmore, D., Granier, C., Guenther, A., Kinnison, D., Laepple, T., Orlando, J., Tie, X., Tyndall, G., Wiedinmyer, C., Baughcum, S. L. and Kloster, S.: Description and evaluation of the Model for Ozone and Related chemical Tracers, version 4 (MOZART-4), Geosci. Model Dev., 3(1), 43–67, doi:10.5194/gmd-3-43-2010, 2010.

Fan, J., Liu, Y., Xu, K., North, K., Collis, S., Dong, X., Zhang, G. J., Chen, Q.,

Kollias, P. and Ghan, S. J.: Improving representation of convective transport for scale-aware parameterization: 1. Convection and cloud properties simulated with spectral bin and bulk microphysics, J. Geophys. Res. Atmos., 120, 3485–3509, doi:10.1002/2014JD022142.Received, 2015.

Fierro, A. O., Mansell, E. R., Ziegler, C. L. and MacGorman, D. R.: Application of a Lightning Data Assimilation Technique in the WRF-ARW Model at Cloud-Resolving Scales for the Tornado Outbreak of 24 May 2011, Mon. Weather Rev., 140(8), 2609–2627, doi:10.1175/MWR-D-11-00299.1, 2012.

Fierro, A. O., Gao, J., Ziegler, C. L., Mansell, E. R., MacGorman, D. R. and Dembek, S. R.: Evaluation of a Cloud-Scale Lightning Data Assimilation Technique and a 3DVAR Method for the Analysis and Short-Term Forecast of the 29 June 2012 Derecho Event, Mon. Weather Rev., 142(1), 183–202, doi:10.1175/MWR-D-13-00142.1, 2014.

Fierro, A. O., Clark, A. J., Mansell, E. R., MacGorman, D. R., Dembek, S. R. and Ziegler, C. L.: Impact of Storm-Scale Lightning Data Assimilation on WRF-ARW Precipitation Forecasts during the 2013 Warm Season over the Contiguous United States, Mon. Weather Rev., 143(3), 757–777, doi:10.1175/MWR-D-14-00183.1, 2015.

Fried, A., Barth, M. C., Bela, M., Weibring, P., Richter, D., Walega, J., Li, Y., Pickering, K., Apel, E., Hornbrook, R., Hills, A., Riemer, D. D., Blake, N., Blake, D. R., Schroeder, J. R., Luo, Z. J., Crawford, J. H., Olson, J., Rutledge, S., Betten, D., Biggerstaff, M. I., Diskin, G. S., Sachse, G., Campos, T., Flocke, F., Weinheimer, A., Cantrel, C., Pollack, I., Peischl, J., Froyd, K., Wisthaler, A., Mikoviny, T. and Woods, S.: Convective transport of formaldehyde to the upper troposphere and lower stratosphere and associated scavenging in thunderstorms over the central United States during the 2012DC3 study, J. Geophys. Res., 121(12), 7430–7460, doi:10.1002/2015JD024477, 2016.

Grell, G. A.: Prognostic Evaluation of Assumptions Used by Cumulus Parameterizations, Mon. Weather Rev., 121(3), 764–787, doi:10.1175/1520-0493(1993)121<0764:PEOAUB>2.0.CO;2, 1993.

Grell, G. A. and Dévényi, D.: A generalized approach to parameterizing convection combining ensemble and data assimilation techniques, Geophys. Res. Lett., 29(14), 38-1-38–4, doi:10.1029/2002GL015311, 2002.

Hodzic, A., Gochis, D., Cui, Y. and Et, A.: Meteorological conditions, emissions and transport of anthropogenic pollutants over the Central Rocky Mountains during the

2011 BEACHON-RoMBAS field study, Prep., 2014.

Hong, S.-Y., Noh, Y. and Dudhia, J.: A New Vertical Diffusion Package with an Explicit Treatment of Entrainment Processes, Mon. Weather Rev., 134(9), 2318–2341, doi:10.1175/MWR3199.1, 2006.

Hong, S. and Lim, J.: The WRF single-moment 6-class microphysics scheme (WSM6), J. Korean Meteorol. Soc., 42(2), 129–151 [online] Available from: http://www.mmm.ucar.edu/wrf/users/docs/WSM6-hong_and_lim_JKMS.pdf%5Cnhttp://search.koreanstudies.net/journal/thesis_name.asp?tname=kiss2002&key=2525908, 2006.

Iacono, M. J., Delamere, J. S., Mlawer, E. J., Shephard, M. W., Clough, S. A. and Collins, W. D.: Radiative forcing by long-lived greenhouse gases: Calculations with the AER radiative transfer models, J. Geophys. Res. Atmos., 113(13), 2–9, doi:10.1029/2008JD009944, 2008.

Khare, P., Kumar, N., Kumari, K. and Srivastava, S.: Atmospheric formic and acetic acids: An overview, Rev. Geophys., 32(2), 227–248 [online] Available from: http://www.agu.org/pubs/crossref/1999/1998RG900005.shtml (Accessed 10 October 2013), 1999.

Knote, C., Hodzic, A., Jimenez, J. L., Volkamer, R., Orlando, J. J., Baidar, S., Brioude, J., Fast, J., Gentner, D. R., Goldstein, A. H., Hayes, P. L., Knighton, W. B., Oetjen, H., Setyan, A., Stark, H., Thalman, R., Tyndall, G., Washenfelder, R., Waxman, E. and Zhang, Q.: Simulation of semi-explicit mechanisms of SOA formation from glyoxal in aerosol in a 3-D model, Atmos. Chem. Phys., 14(12), 6213–6239, doi:10.5194/acp-14-6213-2014, 2014.

Koren, V., Schaake, J., Mitchell, K., Duan, Q. Y., Chen, F. and Baker, J. M.: A parameterization of snowpack and frozen ground intended for NCEP weather and climate models, J. Geophys. Res. Atmos., 104(D16), 19569–19585, doi:10.1029/1999JD900232, 1999.

Lee, M., Heikes, B. G. and O'Sullivan, D. W.: Hydrogen peroxide and organic hydroperoxide in the troposphere: a review, Atmos. Environ., 34(21), 3475–3494, doi:10.1016/S1352-2310(99)00432-X, 2000.

Lelieveld, J. and Crutzen, P. J.: Role of Deep Cloud Convection in the Ozone Budget of the Troposphere, Science (80-.)., 264(5166), 1759–1761, doi:10.1126/science.264.5166.1759, 1994.

Li, Y., Pickering, K. E., Allen, D. J., Barth, M. C., Bela, M. M., Cummings, K. A., Carey, L. D., Mecikalski, R. M., Fierro, A. O., Campos, T. L., Weinheimer, A. J., Diskin, G. S. and Biggerstaff, M. I.: Evaluation of deep convective transport in storms from different convective regimes during the DC3 field campaign using WRF-Chem with lightning data assimilation, J. Geophys. Res. Atmos., 122(13), 7140–7163, doi:10.1002/2017JD026461, 2017.

Lin, Y.-L., Farley, R. D. and Orville, H. D.: Bulk Parameterization of the Snow Field in a Cloud Model, J. Clim. Appl. Meteorol., 22(6), 1065–1092, doi:10.1175/1520-0450(1983)022<1065:BPOTSF>2.0.CO;2, 1983.

Marchand, M. R. and Fuelberg, H. E.: Assimilation of Lightning Data Using a Nudging Method Involving Low-Level Warming, Mon. Weather Rev., 142(12), 4850–4871, doi:10.1175/MWR-D-14-00076.1, 2014.

Mecikalski, R. M., Bain, A. L. and Carey, L. D.: Radar and Lightning Observations of Deep Moist Convection across Northern Alabama during DC3: 21 May 2012, Mon. Weather Rev., 143(7), 2774–2794, doi:10.1175/MWR-D-14-00250.1, 2015.

Morrison, H. and Milbrandt, J.: Comparison of Two-Moment Bulk Microphysics Schemes in Idealized Supercell Thunderstorm Simulations, Mon. Weather Rev., 139(4), 1103–1130, doi:10.1175/2010MWR3433.1, 2011.

Morrison, H., Curry, J. A., Shupe, M. D. and Zuidema, P.: A New Double-Moment Microphysics Parameterization for Application in Cloud and Climate Models. Part II: Single-Column Modeling of Arctic Clouds, J. Atmos. Sci., 62(6), 1678–1693, doi:10.1175/JAS3447.1, 2005.

Morrison, H., Thompson, G. and Tatarskii, V.: Impact of Cloud Microphysics on the Development of Trailing Stratiform Precipitation in a Simulated Squall Line: Comparison of One- and Two-Moment Schemes, Mon. Weather Rev., 137(3), 991–1007, doi:10.1175/2008MWR2556.1, 2009.

O'Sullivan, D. W., Lee, M., Noone, B. C. and Heikes, B. G.: Henry's Law Constant Determinations for Hydrogen Peroxide, Methyl Hydroperoxide, Hydroxymethyl Hydroperoxide, Ethyl Hydroperoxide, and Peroxyacetic Acid, J. Phys. Chem., 100(8), 3241–3247, 1996.

Paulot, F., Wunch, D., Crounse, J. D., Toon, G. C., Millet, D. B., DeCarlo, P. F., Vigouroux, C., Deutscher, N. M., González Abad, G., Notholt, J., Warneke, T., Hannigan, J. W., Warneke, C., de Gouw, J. a., Dunlea, E. J., De Mazière, M., Griffith,

D. W. T., Bernath, P., Jimenez, J. L. and Wennberg, P. O.: Importance of secondary sources in the atmospheric budgets of formic and acetic acids, Atmos. Chem. Phys., 11(5), 1989–2013, doi:10.5194/acp-11-1989-2011, 2011.

Phoenix, D. B., Homeyer, C. R. and Barth, M. C.: Sensitivity of simulated convection-driven stratosphere-troposphere exchange in WRF-Chem to the choice of physical and chemical parameterization, Earth Sp. Sci., 4(8), 454–471, doi:10.1002/2017EA000287, 2017.

Prather, M. J. and Jacob, D. J.: Photochemistry of the Upper Troposphere Driven By Deep Tropical Convection, Geophys. Res. Lett., 24(24), 3189, doi:10.1029/97GL03027, 1997.

Rajeevan, M., Kesarkar, A., Thampi, S. B., Rao, T. N., Radhakrishna, B. and Rajasekhar, M.: Sensitivity of WRF cloud microphysics to simulations of a severe thunderstorm event over Southeast India, Ann. Geophys., 28(2), 603–619, doi:10.5194/angeo-28-603-2010, 2010.

Sander, R.: Compilation of Henry's law constants (version 4.0) for water as solvent, Atmos. Chem. Phys., 15(8), 4399–4981, doi:10.5194/acp-15-4399-2015, 2015.

Skamarock, W. C., Klemp, J. B., Gill, D. O., Barker, D. M., Duda, M. G., Wang, W. and Powers, J. G.: A Description of the Advanced Research WRF Version 3., 2008.

Treadaway, V., Heikes, B. G., McNeill, A. S., Silwal, I. K. C. and O'Sullivan, D. W.: Measurement of formic acid, acetic acid and hydroxyacetaldehyde, hydrogen peroxide, and methyl peroxide in air by chemical ionization mass spectrometry: Airborne method development, Atmos. Meas. Tech., 11(4), 1901–1920, doi:10.5194/amt-11-1901-2018, 2018.

White, B., Gryspeerdt, E., Stier, P., Morrison, H., Thompson, G. and Kipling, Z.: Uncertainty from the choice of microphysics scheme in convection-permitting models significantly exceeds aerosol effects, Atmos. Chem. Phys., 17(19), 12145–12175, doi:10.5194/acp-17-12145-2017, 2017.

Zhang, R., Zhang, Y., Xu, L., Zheng, D. and Yao, W.: Assimilation of total lightning data using the three-dimensional variational method at convection-allowing resolution, J. Meteorol. Res., 31(4), 731–746, doi:10.1007/s13351-017-6133-3, 2017.

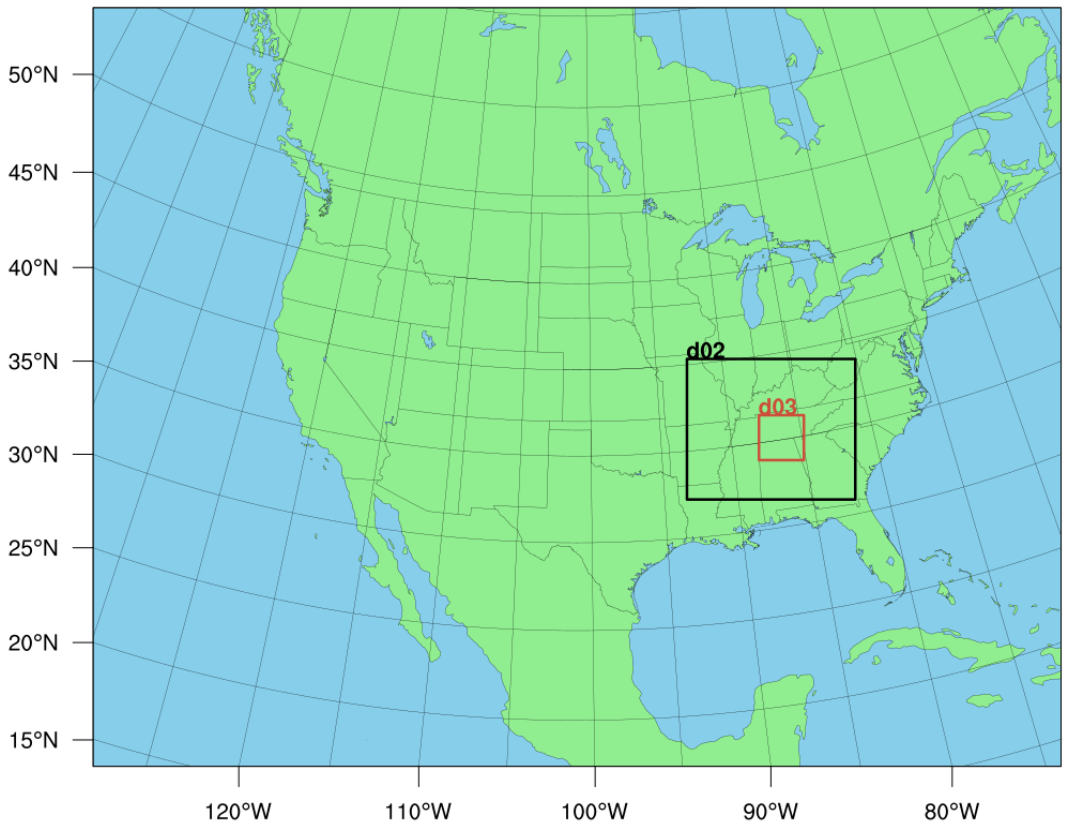

Figure 1.1: Map of the three WRF domains with horizontal resolutions of 15 km (415x325), 3 km (361x301), and 0.6 km (481x481). The outer domain (d01, 15 km) is the whole picture and had 415 grid points in the east-west direction and 325 in the north-south direction. The second domain (d02, 3km) is the white box with 361 grid points in east-west and 301 in the north-south direction. The third domain (d03, 0.6 km) is the red box and had 481 grid points in both the east-west and north-south directions. There were 40 vertical levels for each domain.

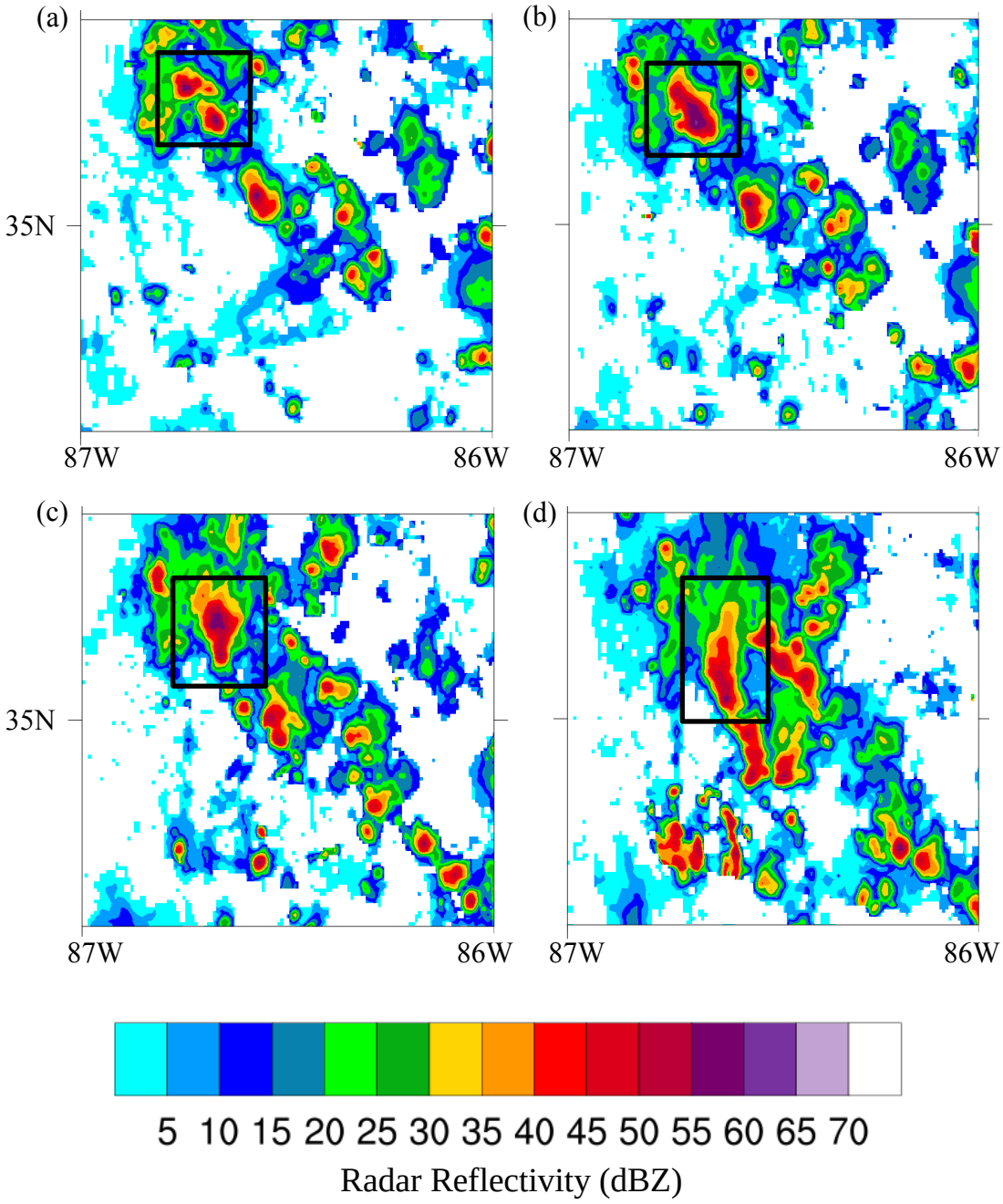

Figure 1.2: Gridded ARMOR-KHTX maximum column radar reflectivity (dBZ). B2 is identified on each map by a black box. The times are: (a) 20:04 UTC, (b) 20:15 UTC, (c) 20:29 UTC, and (d) 20:51 UTC.

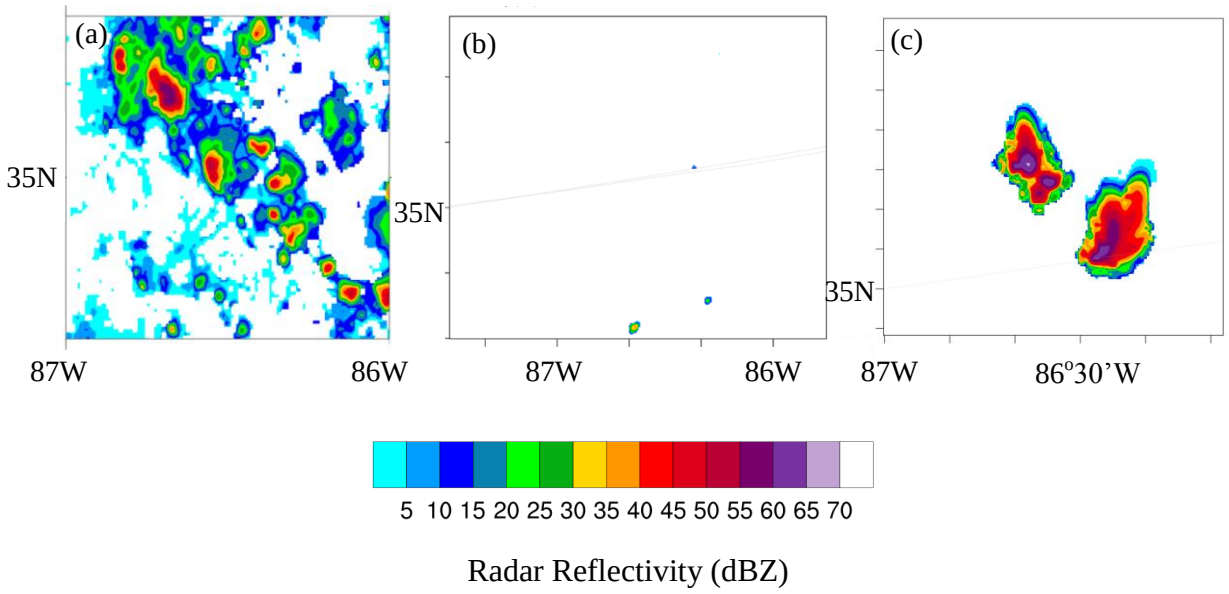

Figure 1.3: Maximum column radar reflectivity (dBZ) for (a) ARMOR at 20:20 UTC, (b) simulation without lightning data assimilation, (c) simulation with lightning data assimilation applied over the temperature range 261-288 K. Simulations used the Morrison double-moment cloud microphysics scheme. The simulations were ~30 minutes delayed relative to observations thus both simulations are for 20:40 UTC. Please note the shift in latitudes and longitudes.

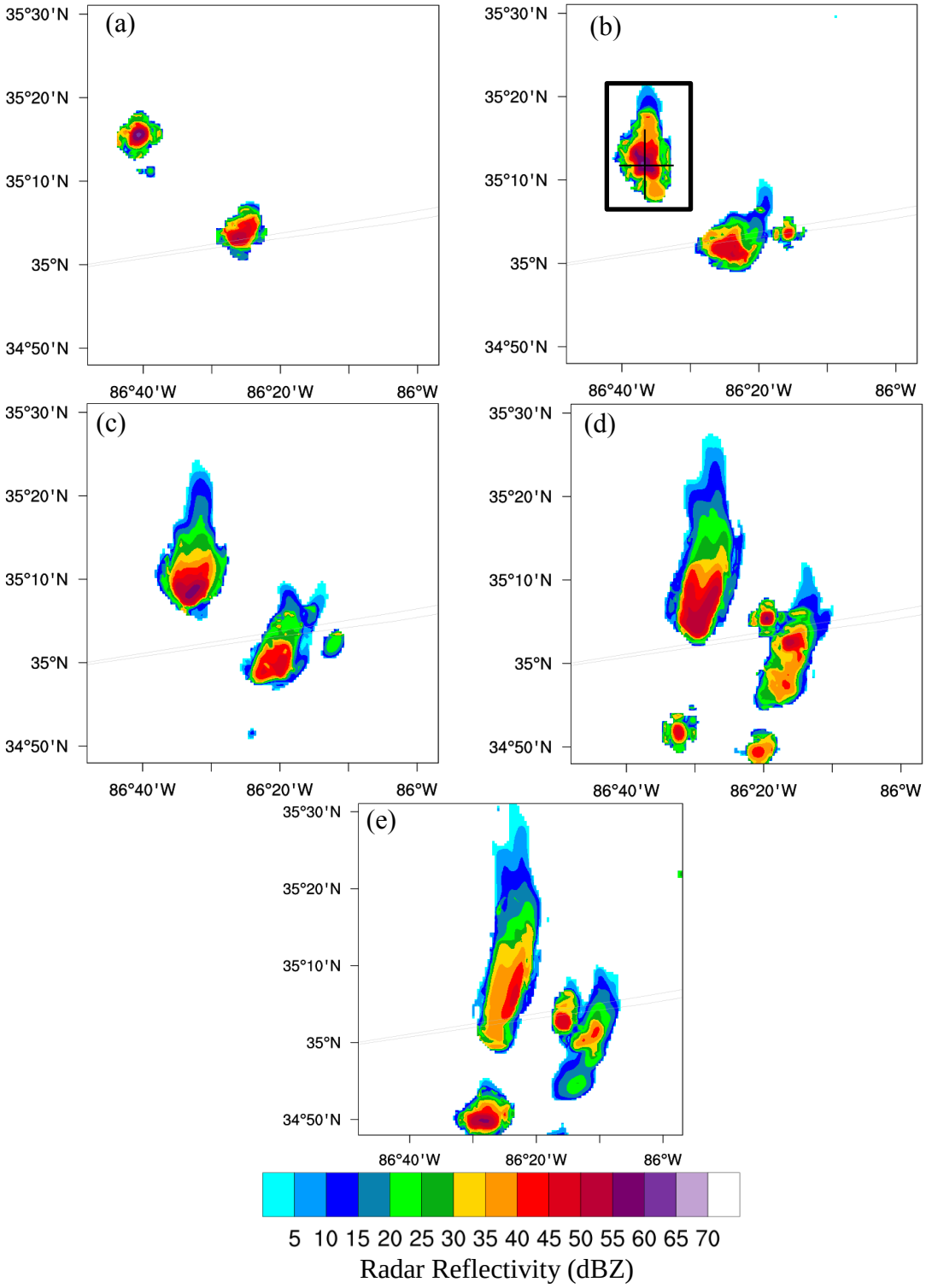

Figure 1.4: Times series of maximum column radar reflectivity (dBZ) for WRF using the Morrison cloud microphysics scheme and lightning data assimilation over the temperature range 261 – 285 K. Storm B2 is identified in 1.4b (black box) and thin lines represent vertical cross sections in Figure 1.9. The times are: (a) 20:30 UTC, (b) 20:50 UTC, (c) 21:10 UTC, (d) 21:30 UTC, and (e) 21:50 UTC.

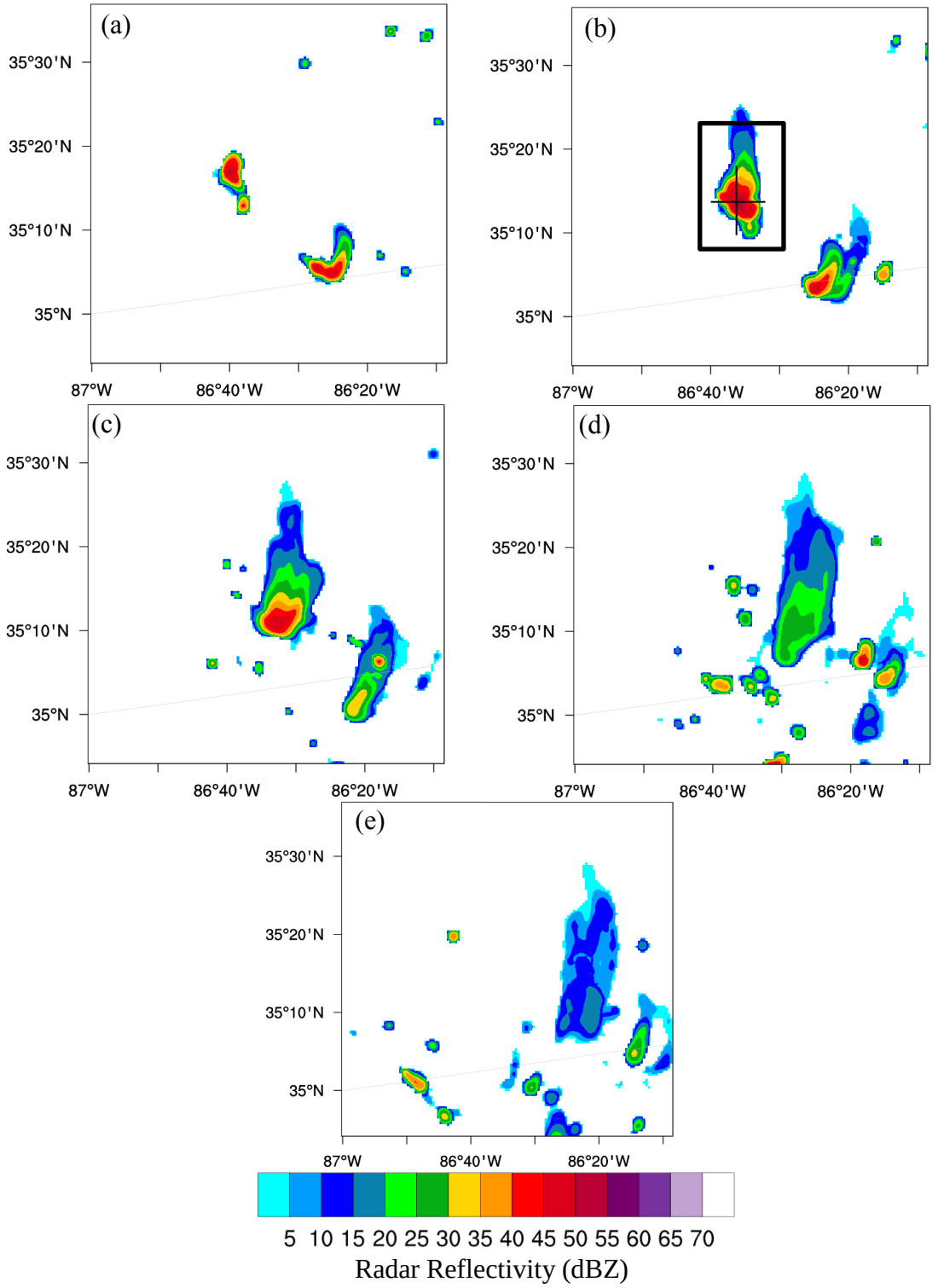

Figure 1.5: Same as Figure 1.4 except for the use of the Lin cloud microphysics scheme over the 261 – 285 K lightning data assimilation temperature range. Storm B2 is identified in 1.5b (black box) and thin lines represent vertical cross sections in Figure 1.8. The times are: (a) 20:30 UTC, (b) 20:50 UTC, (c) 21:10 UTC, (d) 21:30 UTC, and (e) 21:50 UTC.

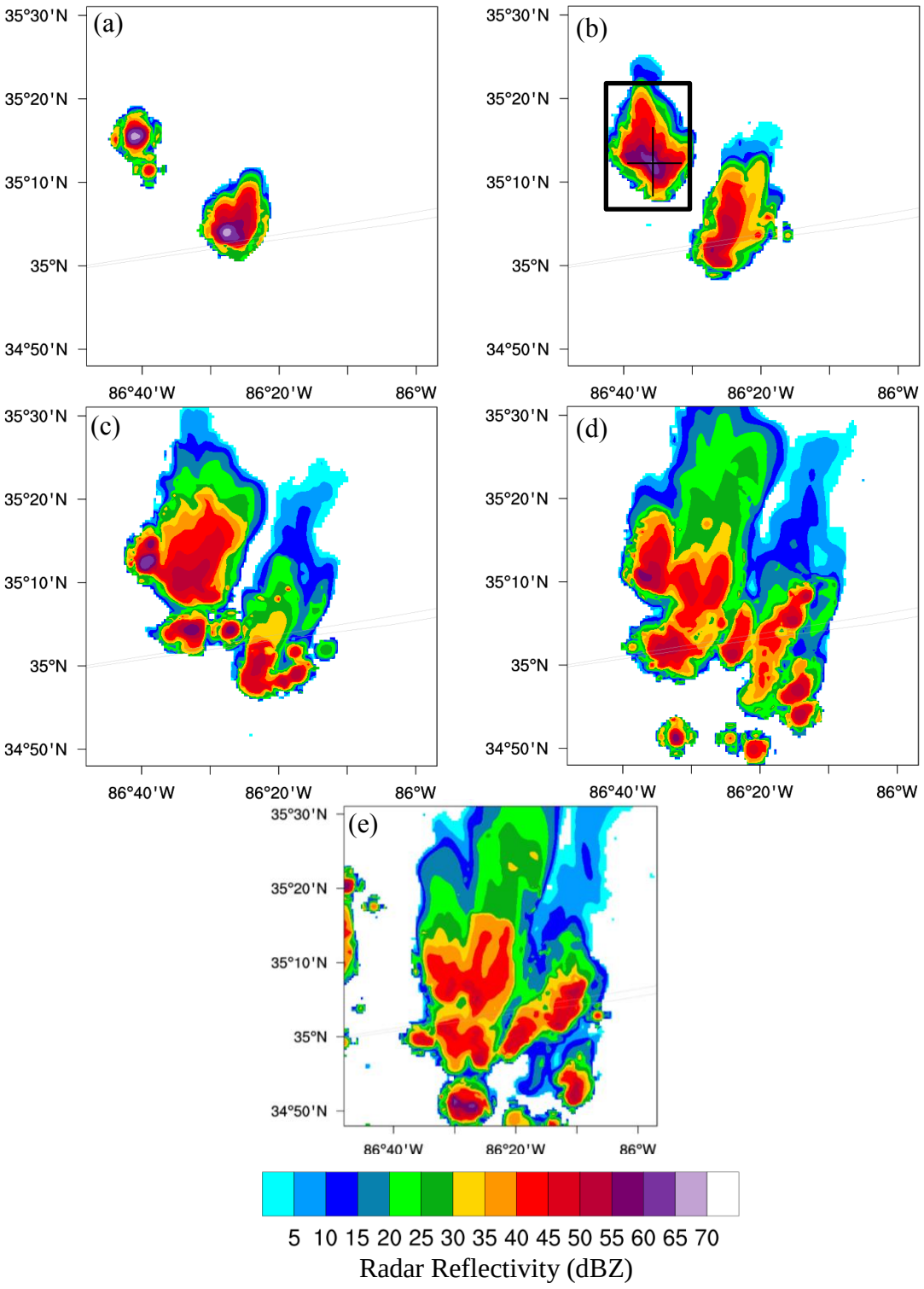

Figure 1.6: Same as Figure 1.4 except for the use of the lightning data assimilation over the temperature range 261 – 288 K. Storm B2 is identified in 1.6b (black box) and thin lines represent vertical cross sections in Figure 1.10. The times are: (a) 20:30 UTC, (b) 20:50 UTC, (c) 21:10 UTC, (d) 21:30 UTC, and (e) 21:50 UTC.

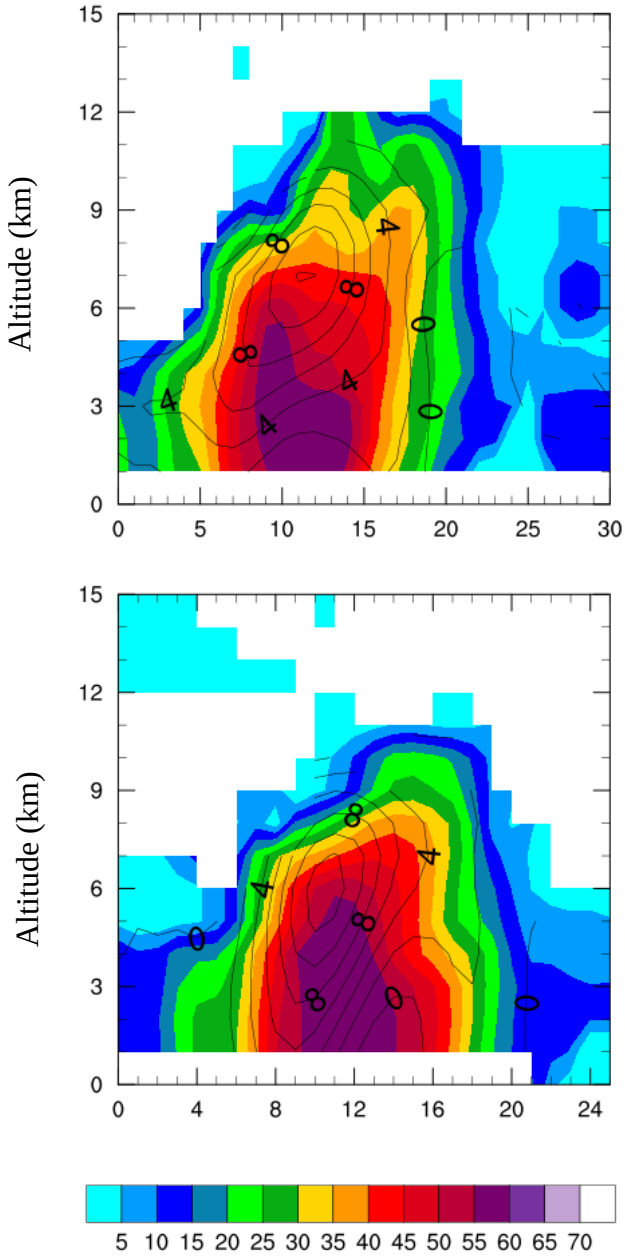

Figure 1.7: Vertical cross-sections of radar reflectivity (dBZ) and vertical wind motion for the ARMOR radar at 20:20 UTC. The horizontal and vertical axes grid spacing are 1 km. The vertical wind contours are from 0 to 16 m/s by 2 m/s increments. The top cross-section shows the south-north transects through the core of maximum column radar reflectivity. The bottom cross-section shows the west-east transect through the core of maximum column radar reflectivity. Note the lengths of the cross-sections are not the same for the south-north and west-east transects in order to use a similar storm box to Mecikalski, Bain, and Carey (2015).

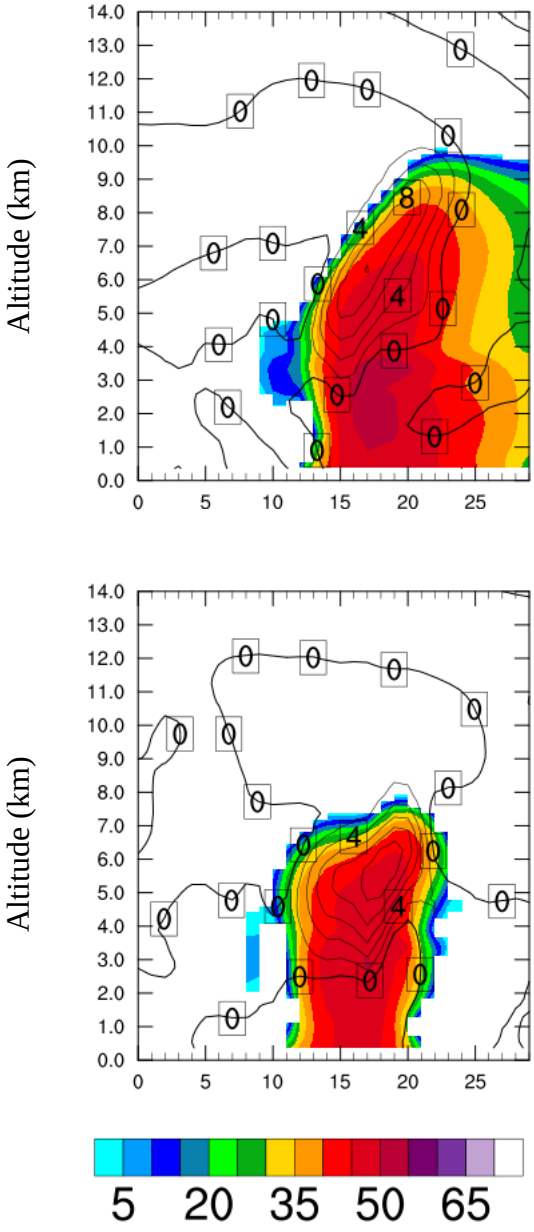

Figure 1.8: Vertical cross-sections of radar reflectivity (dBZ) and vertical wind motion using the Lin cloud microphysics scheme with lightning data assimilation over the 261 - 285 K temperature range at 20:50 UTC. The x axis represents the horizontal grid spacing (0.6 km) and the y axis is altitude (km). The vertical wind contours are from 0 to 24 m/s by 2 m/s increments. The top plot shows the south-north transect through the core of maximum radar reflectivity and the bottom shows the west-east transect through the core of maximum radar reflectivity. Location of the cross-section is shown on Figure 1.5b.

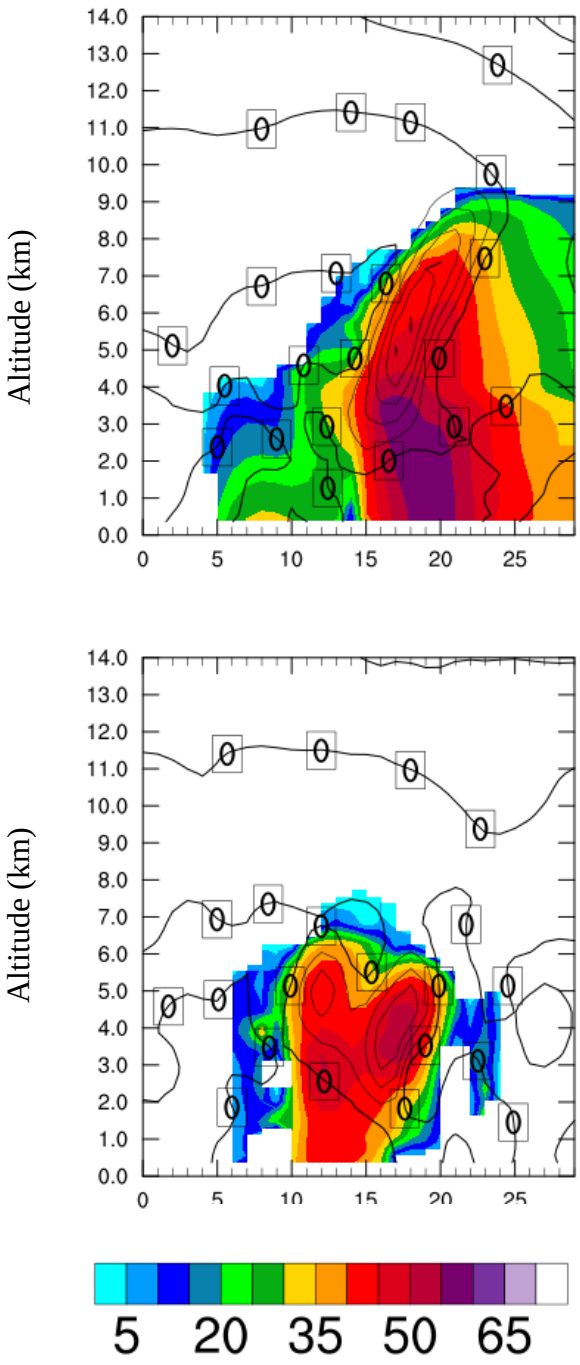

Figure 1.9: Same set-up as Figure 1.8 but using the Morrison cloud microphysics scheme and lightning data assimilation over the 261 – 285 K temperature range at 20:50 UTC. Location of the cross-section is shown on Figure 1.4b.

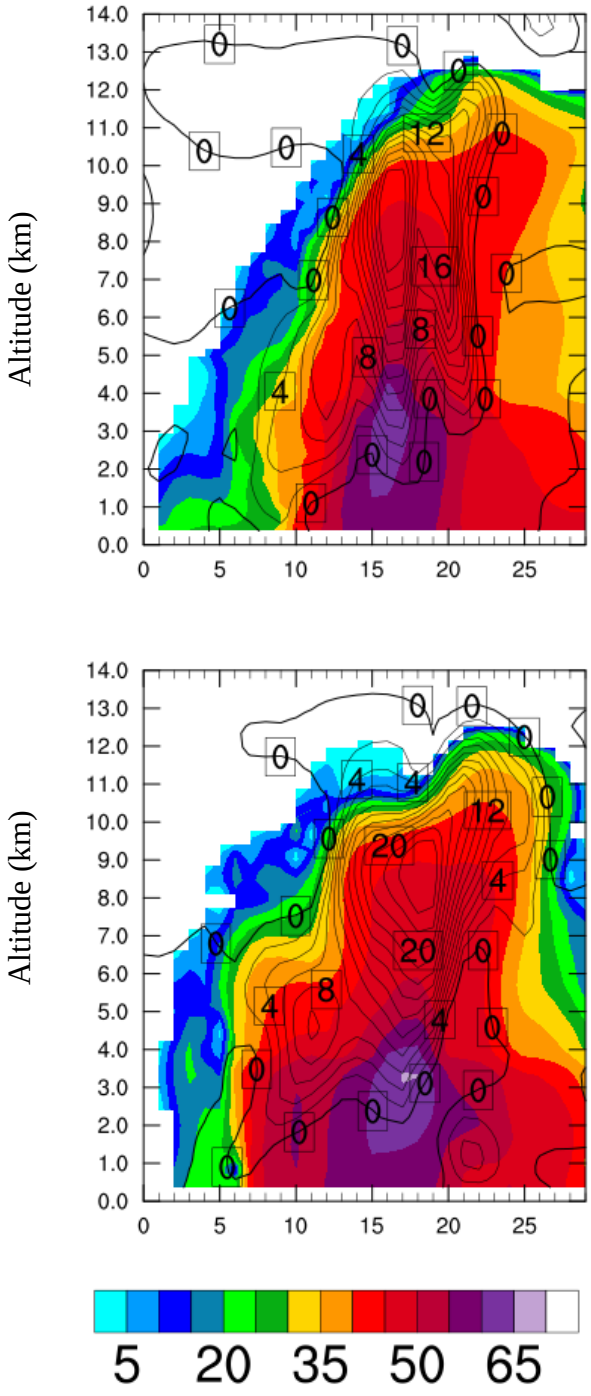

Figure 1.10: Same set-up as Figure 1.8 but using the Morrison cloud microphysics scheme and lightning data assimilation over the 261 – 288 K temperature range at 20:50 UTC. Location of the cross-section is shown on Figure 1.6b.

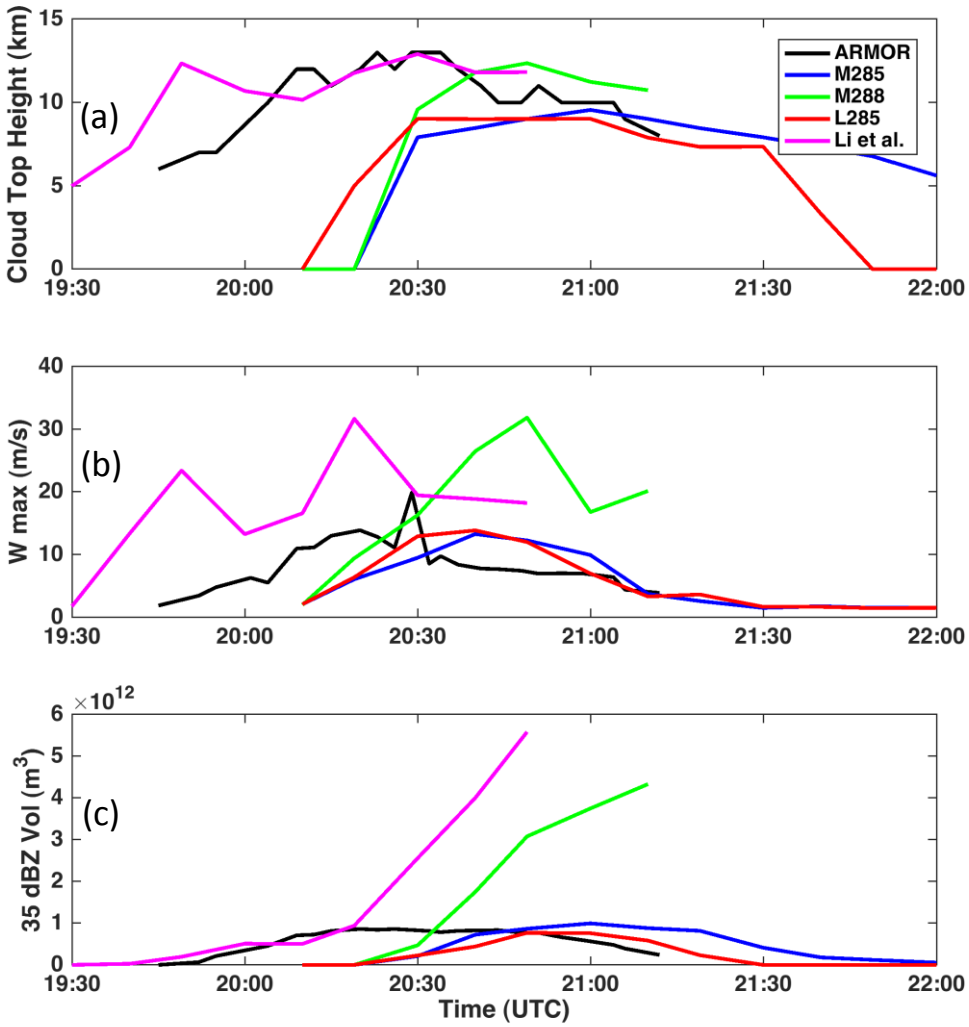

Figure 1.11: Time series for ARMOR observations (black), Morrison LDA from 261 - 285 K (blue), Morrison LDA from 261 - 288 (green), Lin LDA from 261 - 285 K (red), and Li et al. (2017) WSM6 data (magenta) for: (a) cloud top height, defined as the maximum altitude with reflectivity greater than 20 dBZ (km), (b) maximum vertical velocity (m/s), and (c) 35 dBZ volume (m^3).

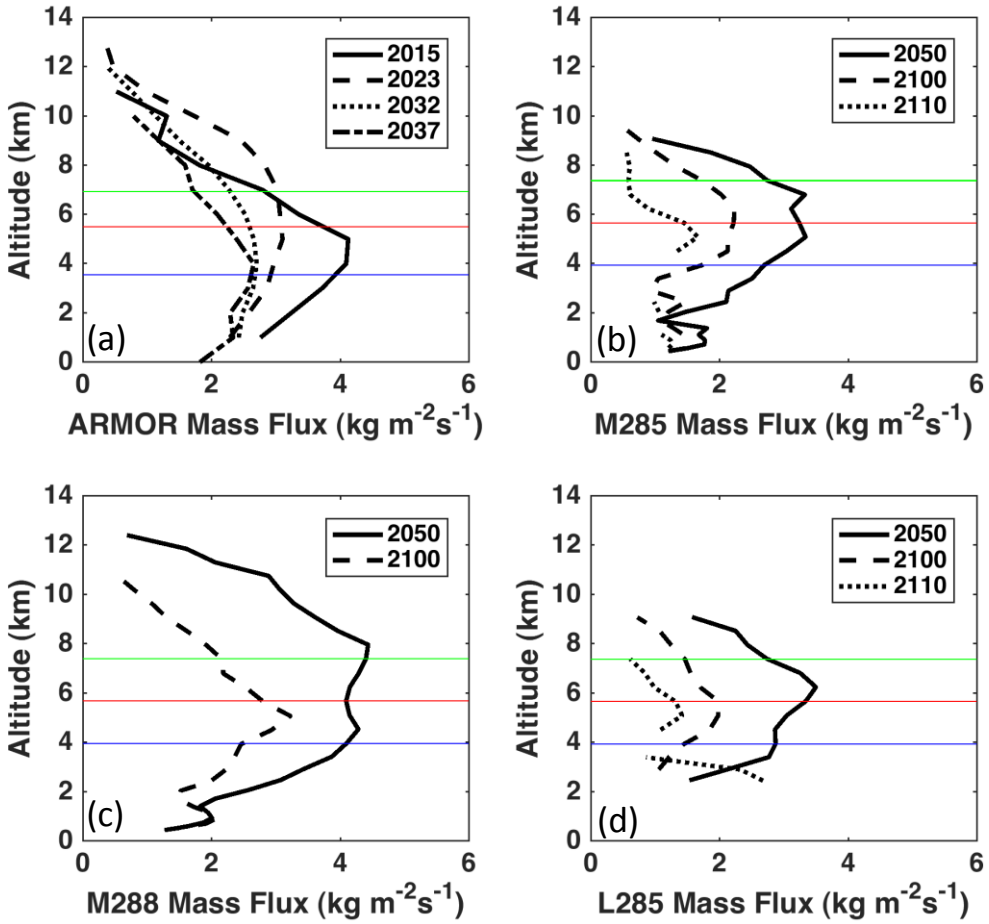

Figure 1.12: Cumulus mass flux profiles (kg m^{-2} s^{-1}) as a function of altitude (km) for multiple times during B2's lifetime for (a) ARMOR observations, (b) Morrison from 261 - 285 K, (c) Morrison from 261 - 288 K , and (d) Lin from 261 - 285 K. This includes the freezing line (0^{o}C, blue), -10^{o}C (red), and -20^{o}C (green).

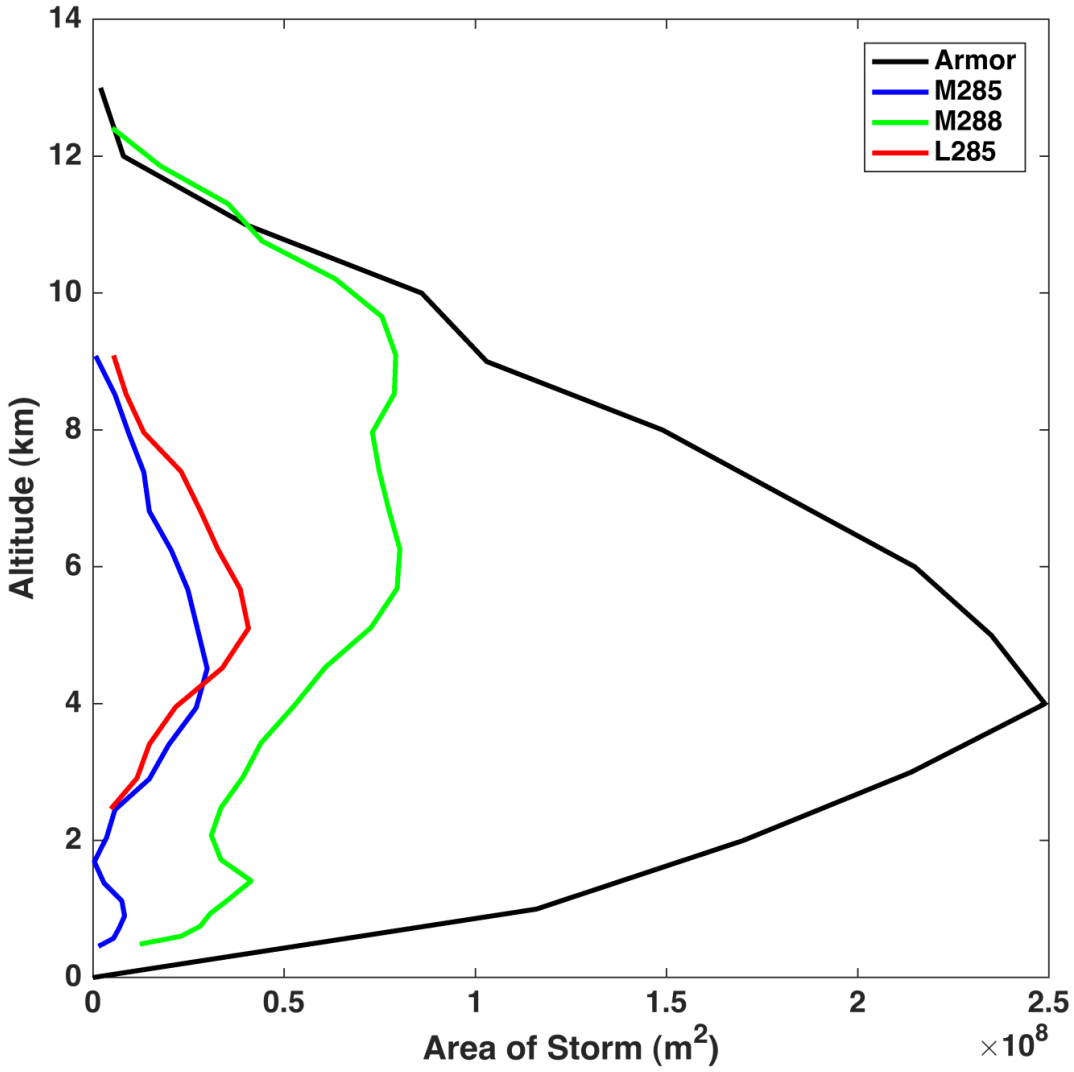

Figure 1.13: Storm area meeting the criteria for upward mass flux in Figure 1.12. The criteria are radar reflectivity greater than 20 dBZ and vertical velocity greater than 1 m/s for ARMOR (black, 20:23 UTC), M285 (blue, 20:50 UTC), M288 (green, 20:50 UTC), L285 (red, 20:50 UTC).

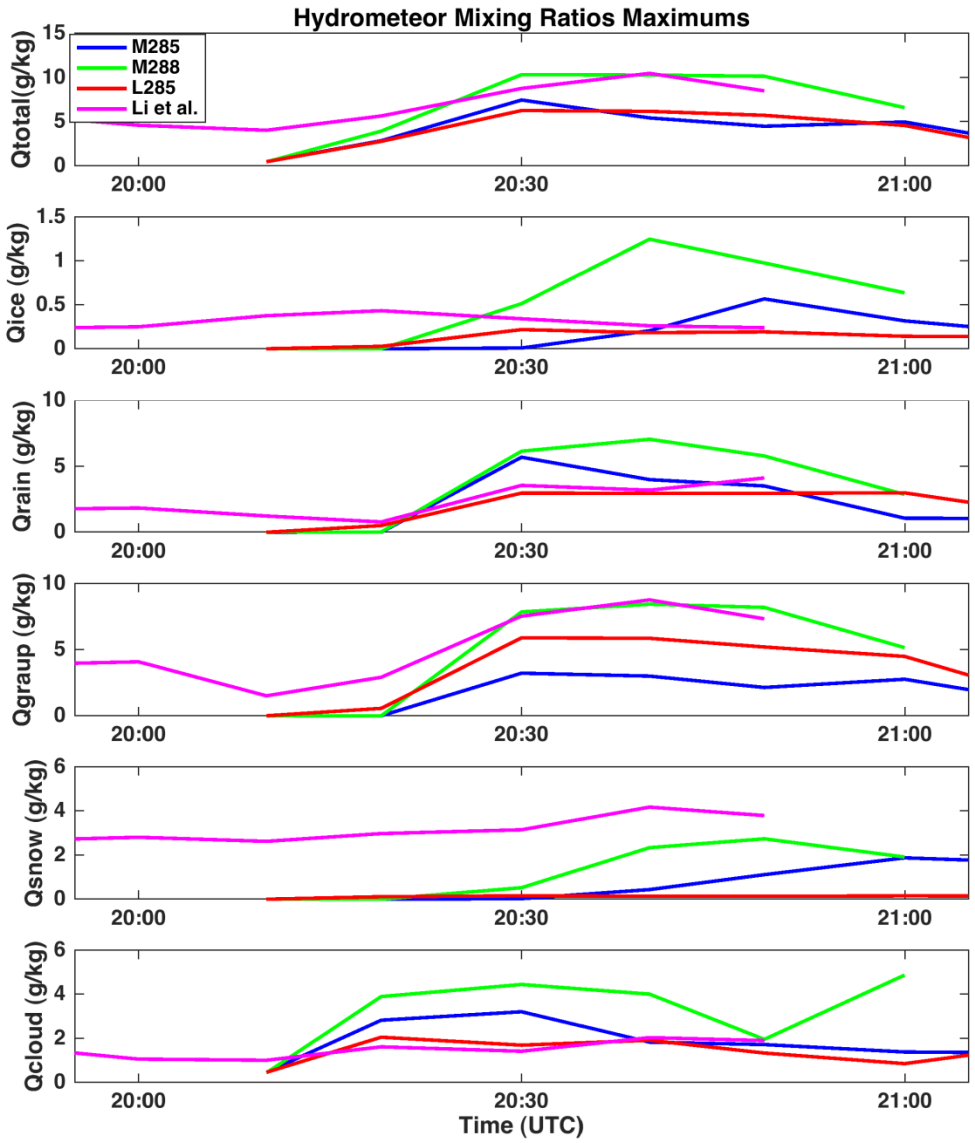

Figure 1.14: Water hydrometeor maximum mixing ratio (g/kg) for total condensed water, rain, graupel/hail, snow, and cloud water from 20:00 - 21:00 UTC. The colors correspond to M285 (blue), M288 (green), L285 (red), and Li et al. (2017) (magenta).

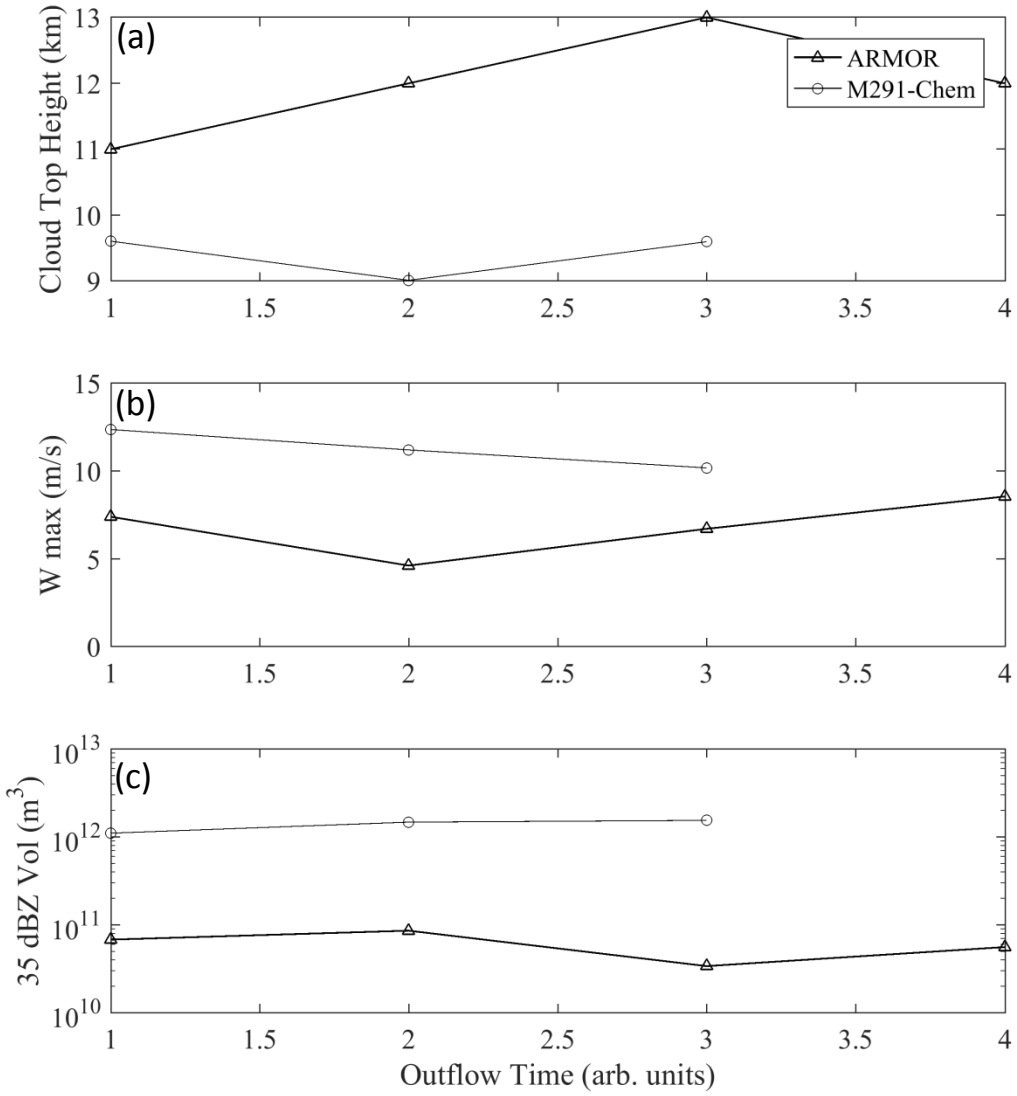

Figure 1.15: Similar time series to Figure 1.11 for the ARMOR outflow time period (20:50-21:14 UTC) (triangle) and WRF-Chem Morrison cloud microphysics scheme with lightning data assimilation from 261 - 291 K from 21:30 - 21:50 UTC (circle): (a) cloud top height, defined as the maximum altitude with reflectivity greater than 20 dBZ (km), (b) maximum vertical velocity (m/s), and (c) 35 dBZ volume (m^3). This has arbitrary units of time as the outflow periods were 30+ minutes apart.

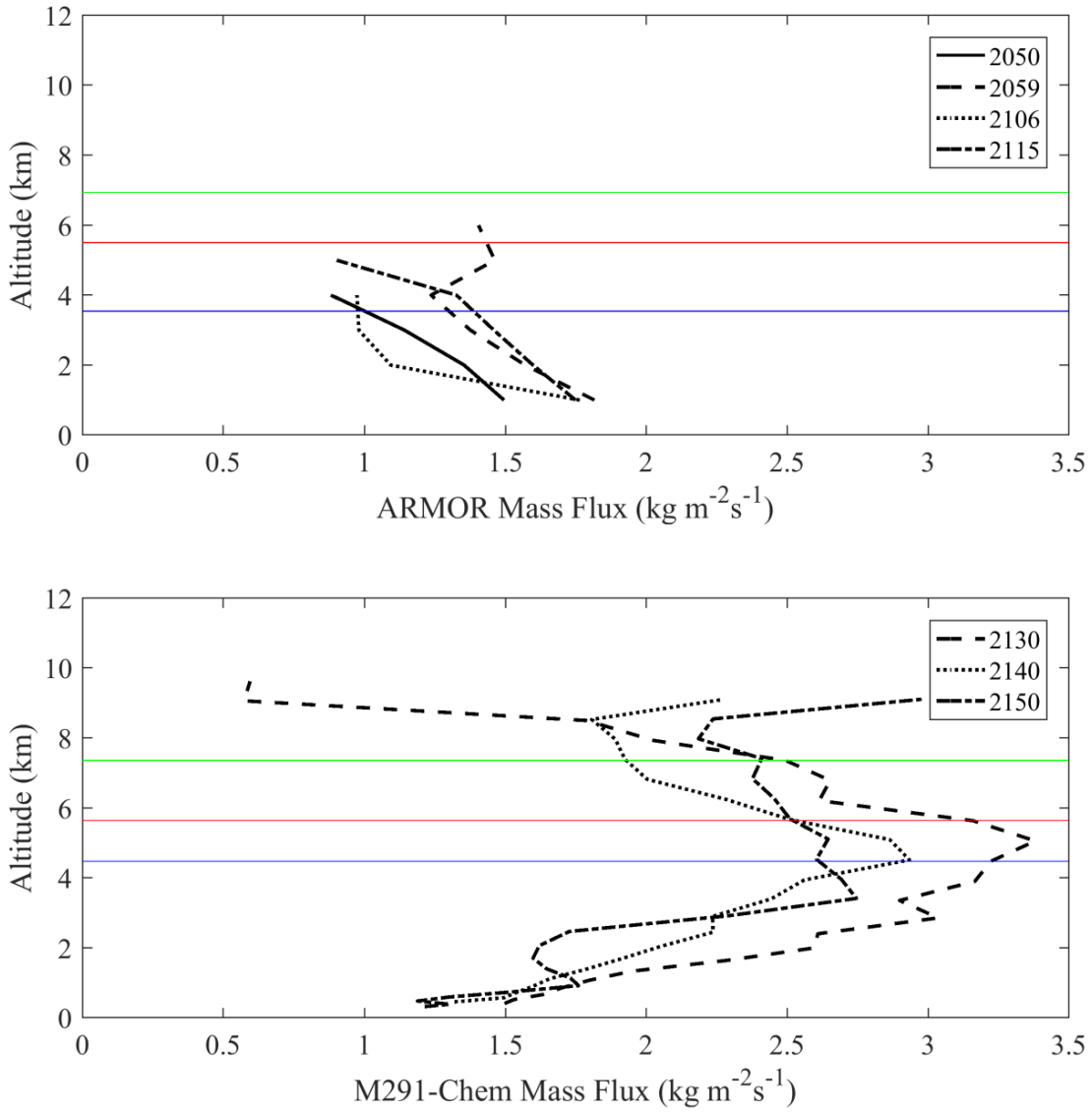

Figure 1.16: Cumulus mass flux profiles (kg m^{-2} s^{-1}) as a function of altitude (km) for multiple outflow times: (top) ARMOR observations, (bottom) Morrison from 261 - 291 K with chemistry. This includes the freezing line (0°C, blue), -10°C (red), and -20°C (green)

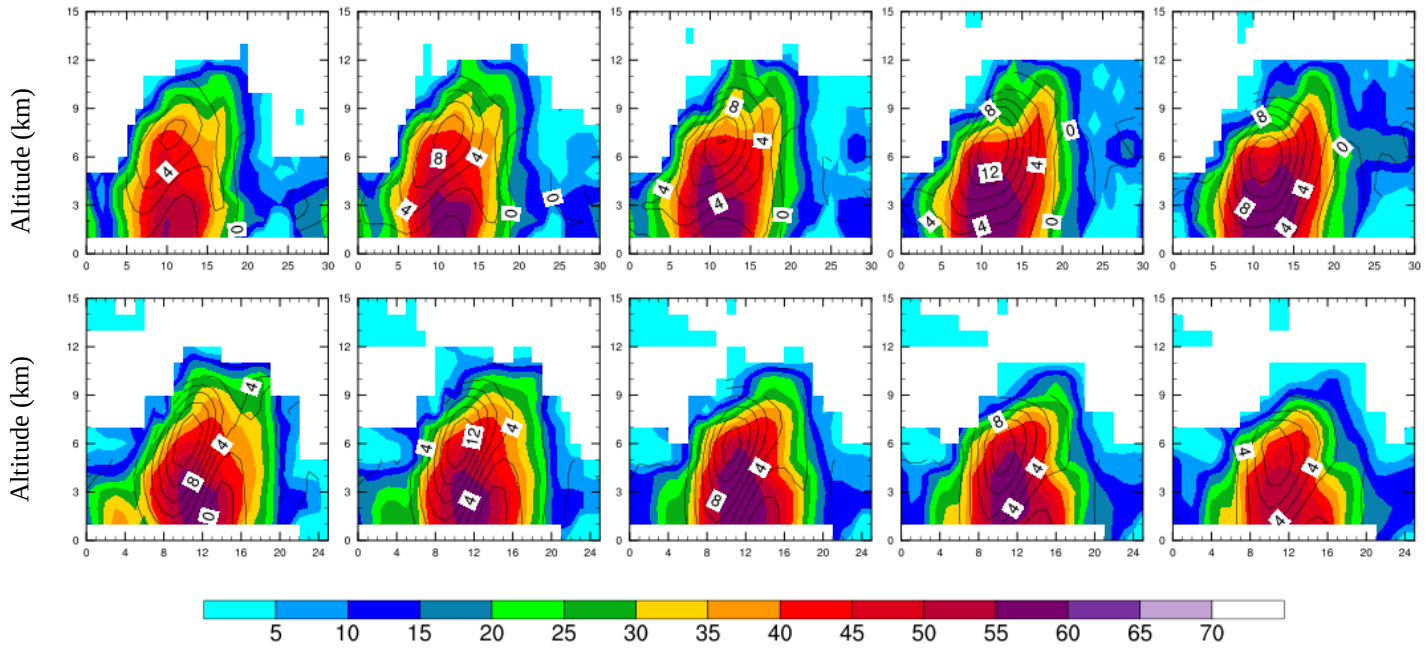

Figure S1.1: Vertical cross-sections of radar reflectivity and vertical wind motion for the ARMOR radar at 20:20 UTC. The axes grid spacing are 1 km. The vertical wind contours are from 0 to 16 m/s by 2 m/s increments. The top row are south-north transects shifting from west to east by 1 km. The bottom row are west-east transects shifting from north to south by 1 km. Note the length of the cross-sections are not the same for the south-north and west-east transects in order to use a similar storm box to Mecikalski, Bain, and Carey (2015).

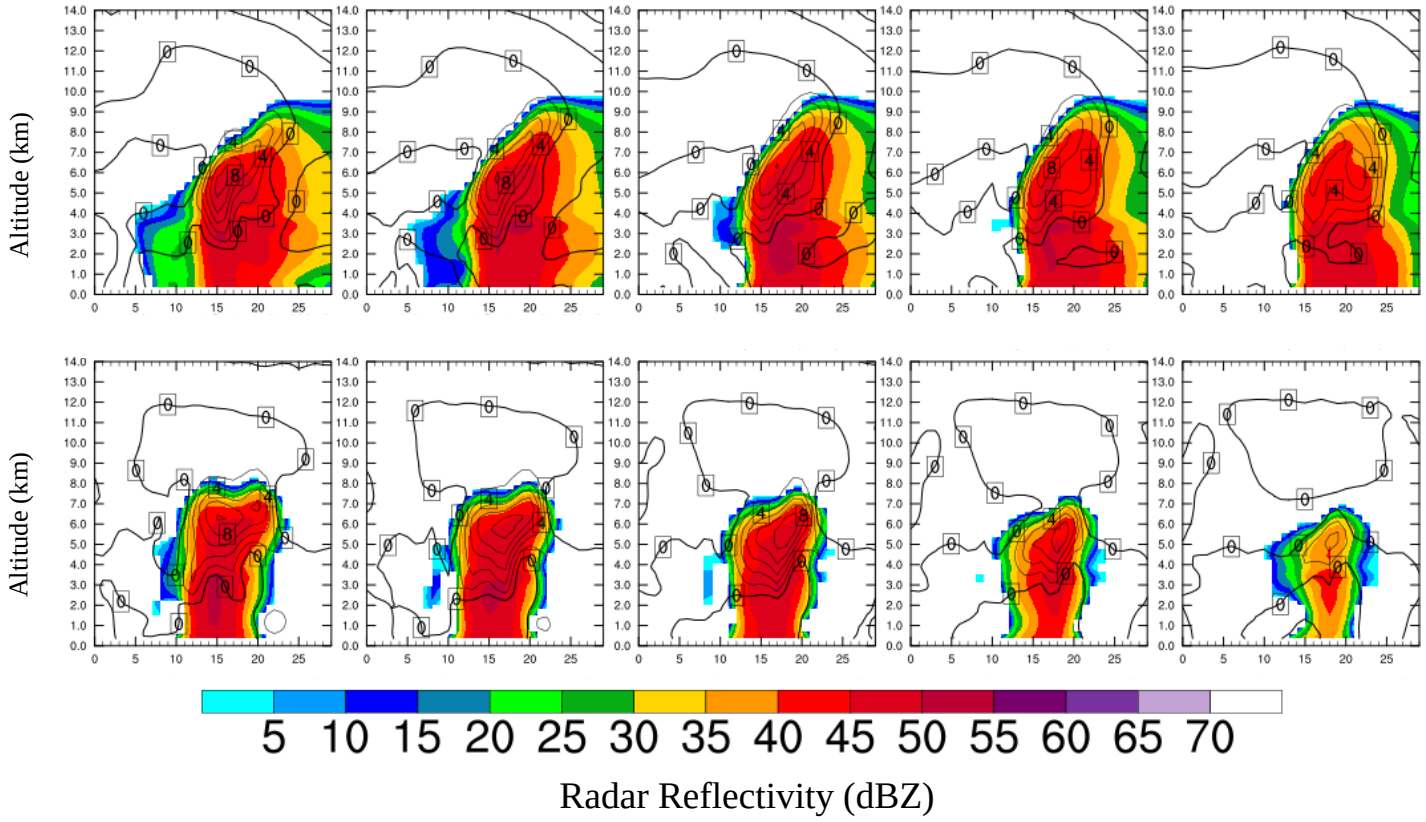

Fig: S1.2: Vertical cross-sections of radar reflectivity and vertical wind motion of the Lin simulation with LDA adjustment between 261 - 285 K at 20:50 UTC. The x axis horizontal grid spacing is 0.6 km and the y axis is altitude (km). The vertical wind contours are from 0 to 24 m/s by 2 m/s increments. The top row are south-north transects shifting from west to east by 1.2 km. The bottom row are west-east transects shifting from north to south by 1.2 km.

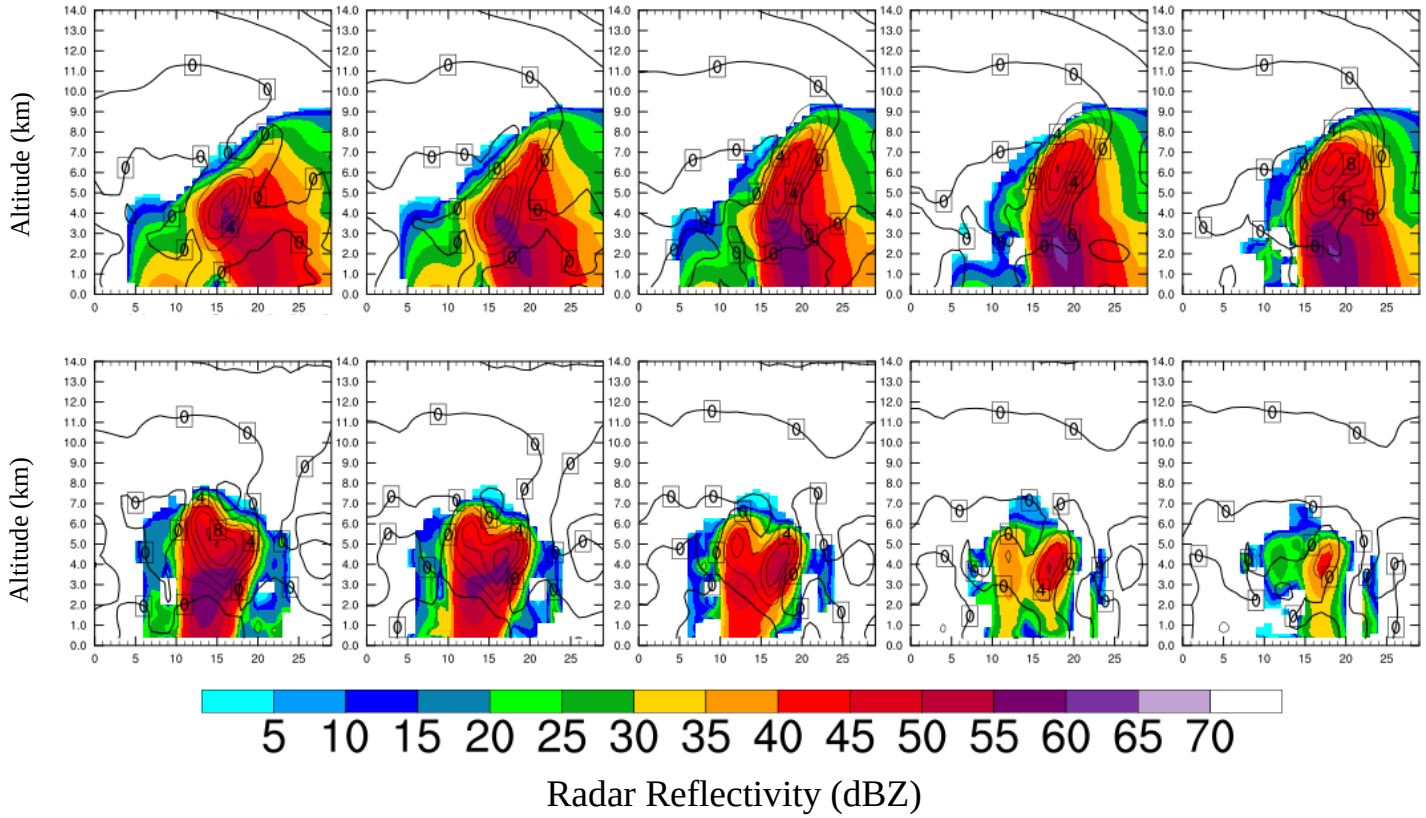

Figure S1.3: Similar to Figure S1.2 for the Morrison simulation with LDA adjustment between 261 - 285 K at 20:50 UTC.

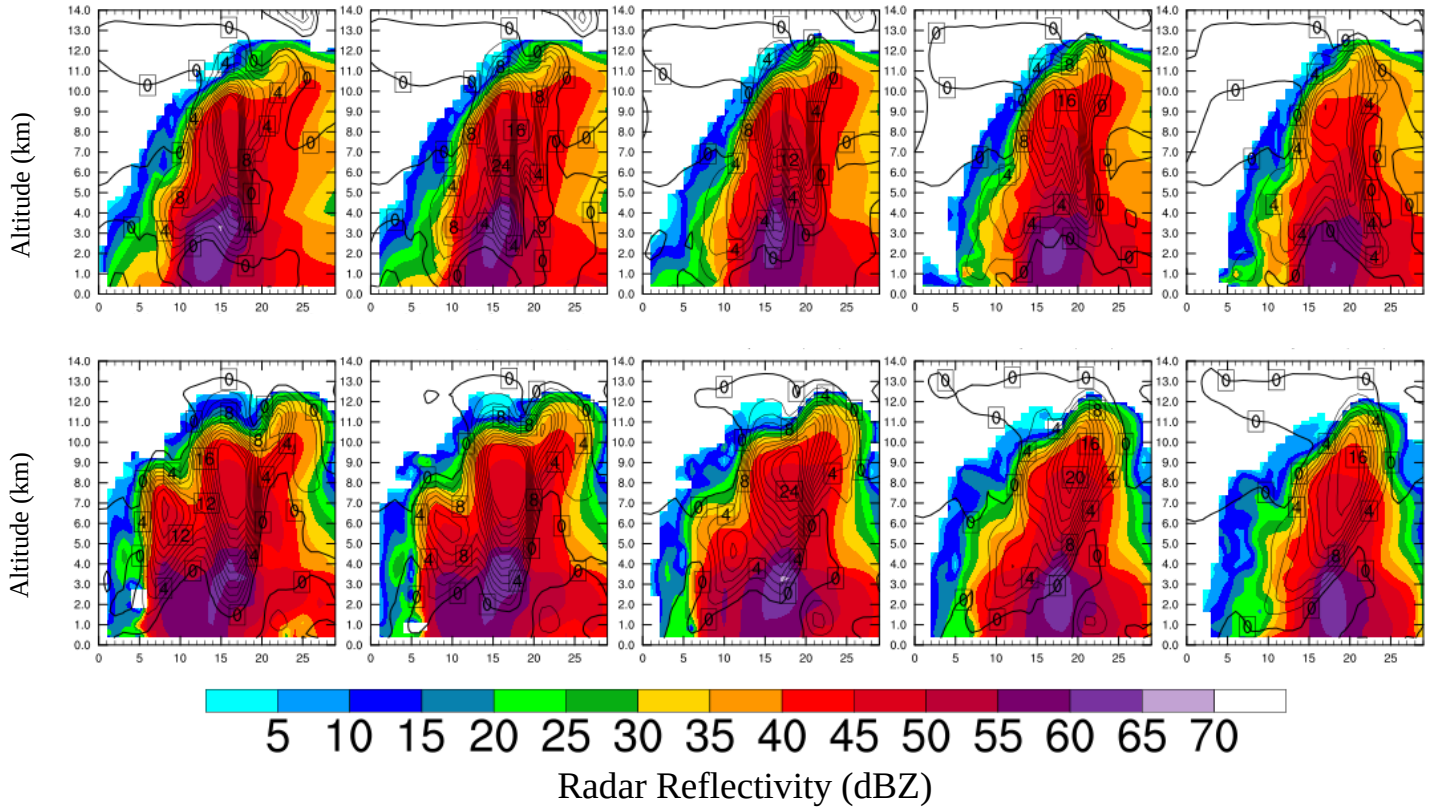

Figure S1.4: Similar to Figure S1.2 for the Morrison simulation with LDA adjustment between 261 - 288 K at 20:50 UTC.

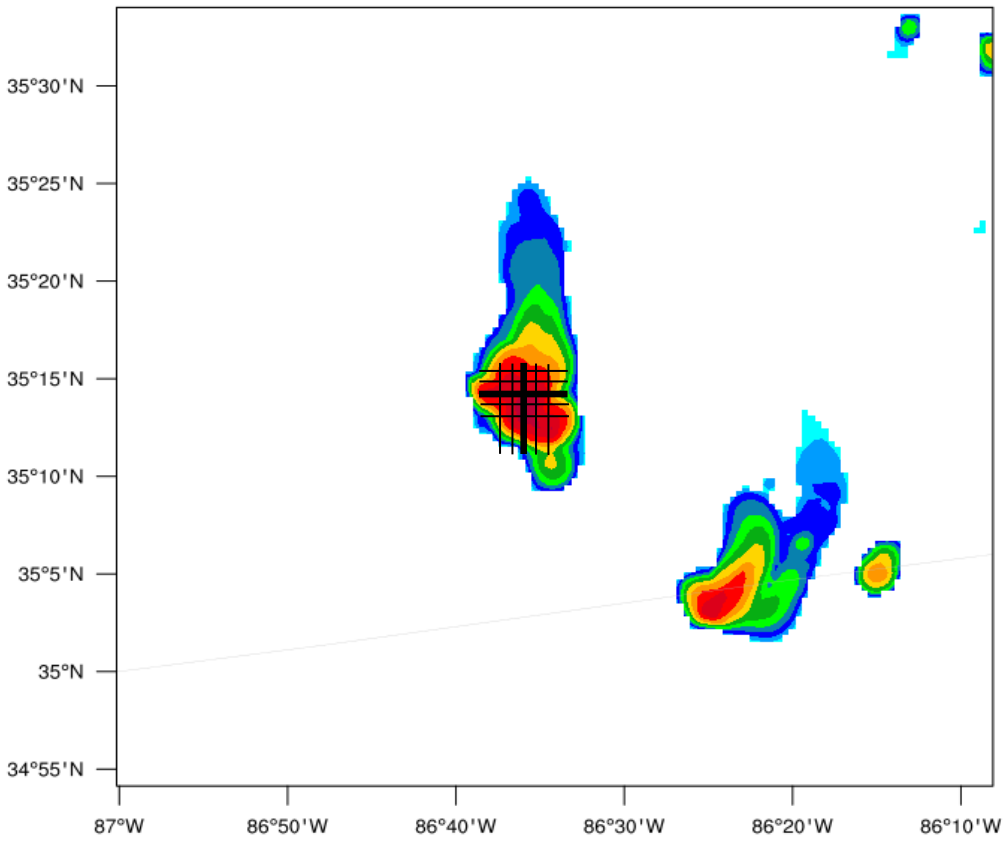

Figure S1.5: An example of the locations of the multiple vertical transects shown for Lin 261 - 285 K. The bolded black lines are the center point (same plot as Figure 1.5b).

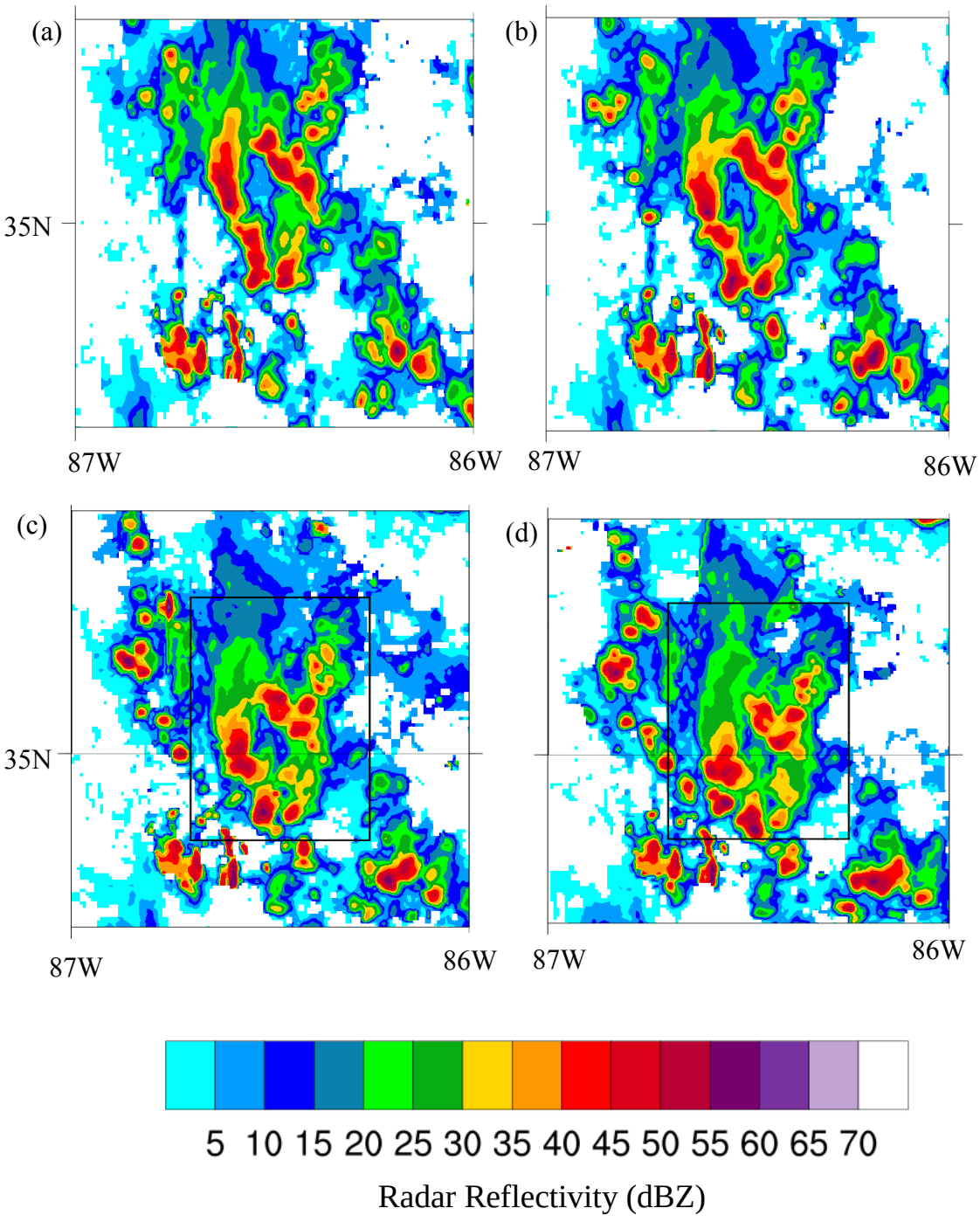

Figure S1.6: ARMOR maximum-column radar reflectivity for (a) 20:51 UTC, (b) 20:59 UTC, (c) 21:06 UTC, and (d) 21:14 UTC. The black box outlines the area used for Figure 1.15.

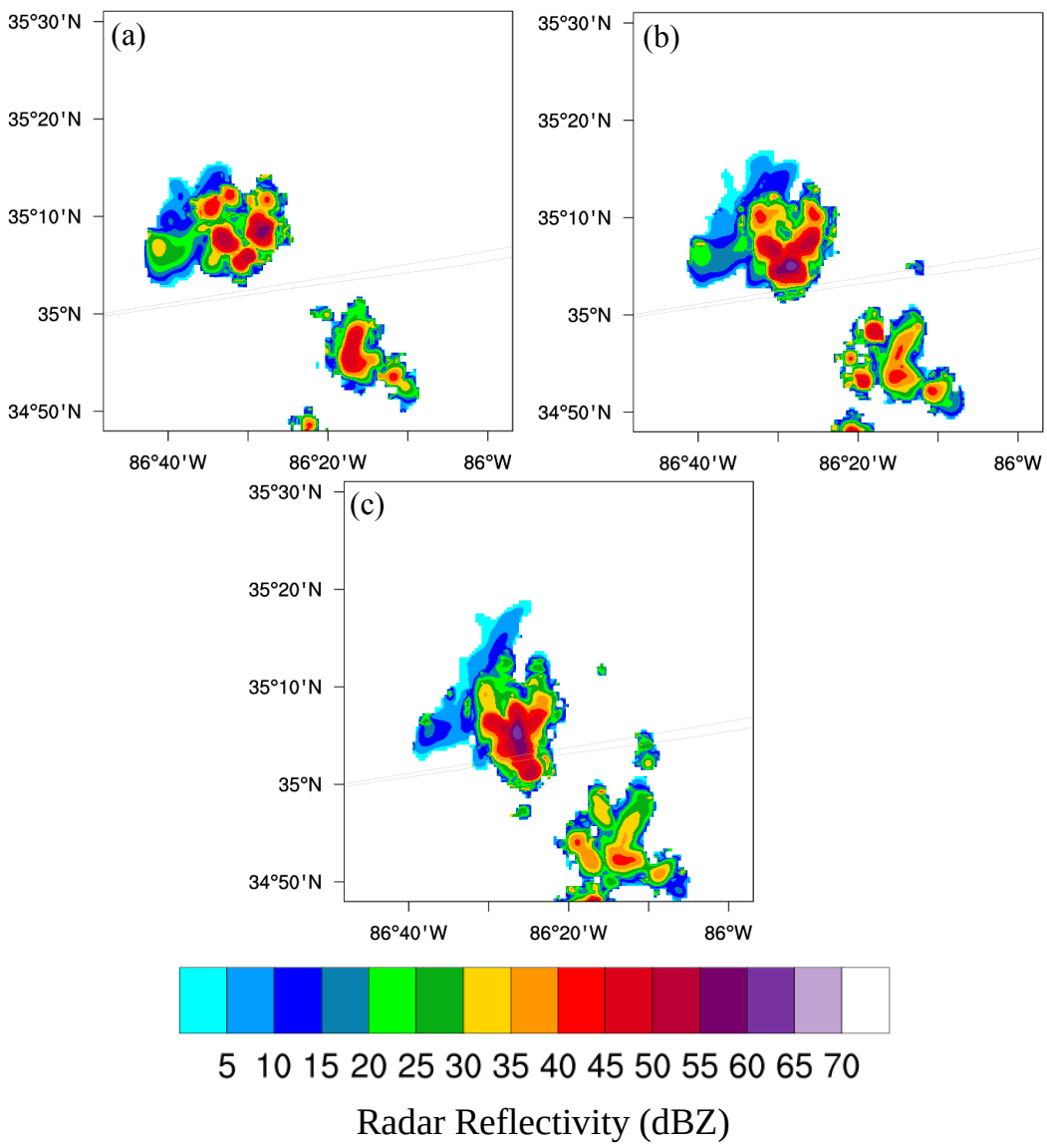

Figure S1.7: WRF-Chem maximum-column radar reflectivity for Morrison with LDA 261 - 291K for (a) 21:30 UTC, (b) 21:40 UTC, and (c) 21:50 UTC.

MANUSCRIPT 2

Convective Transport and Scavenging of Formic and Acetic Acid over the Central United States during DC3

By

Victoria Treadaway[1], Mary Barth[2], Brian Heikes[1]

To be submitted to Journal of Geophysical Research: Atmospheres

---

[1]Graduate School of Oceanography

[2]National Center for Atmospheric Research

Abstract

This study investigated the impact of deep convection on the transport and fate of formic and acetic acid using observations and models. This work was motivated by an observed increase in formic acid (HFo) to 700 ppt at 8 km, approximately 300 ppt in excess of boundary layer air, an increase which was not observed in other soluble species. Possible explanations for this including aqueous production and a pH dependent scavenging were investigated with the Weather Research and Forecasting Model v. 3.7 coupled with chemistry (WRF-Chem) and a photochemical box model. The scavenging efficiency (SE) for HFo and acetic acid (HAc), and multiple other soluble species (CH_2O, H_2O_2, CH_3OOH, HNO_3, SO_2 and NH_3), were calculated based on observations and compared with WRF-Chem storm results for two structures, a convective multicell complex and an isolated convective cell. Observed CH_2O and HNO_3 SEs were significantly different between the two storms. There was no significant difference in the WRF-Chem SE for any of the species between the two storms. There was no appreciable difference in HFo outflow due to aqueous chemistry though WRF-Chem only includes the CH_2O production source. A box model evaluated the influence of pH, temperature range of aqueous production, HFo aqueous sources. The box model was able to produce more HFo in the outflow compared to the inflow when a pH of 3.5, multiple HFo aqueous sources, and aqueous chemistry up to -40^{o}C were assumed. The aqueous production of HAc was pH dependent in the box model due to pyruvic acid being a principle precursor. HAc had the highest mixing ratio at a pH of 5.5coinciding with the maximum aqueous phase pyruvic acid, owing to its effective solubility at pHs greater than its pKa of 4.75. The combination of

observational and model work showed that HFo scavenging does differ between different storms in the same region and it is possible to have an outflow HFo that is greater than the inflow.

1 Introduction

Deep convection transports boundary layer (BL) chemicals to the upper troposphere (UT) and as a result impacts atmospheric composition far from their origin. The 2012 Deep Convective Clouds and Chemistry (DC3) field campaign sampled airmass and mesoscale deep convective systems to study how BL chemicals were redistributed and transformed to the UT (Barth et al., 2015). This redistribution is affected by scavenging, aqueous production, lightning NO_x, entrainment/detrainment, and ice processes. A simple schematic of a mature single cell thunderstorm highlighting some of these processes is presented in Figure 2.1. In the layer between 0 and -40^{o}C is a mixed-phase ice and water region within which both cloud water and ice exist. Above -40^{o}C there are only ice particles. Heavy precipitation is in the downdraft.

Scavenging efficiency (SE) is commonly used to quantify the removal of a soluble BL constituent by precipitation during its transport through a storm. SE quantifies the fraction of soluble species removed by precipitation in a storm by measuring soluble species in the storm inflow and outflow. SE determination is impacted by processes, other than removal by precipitation, which alter a species composition such as aqueous and ice chemistry, entrainment, and detrainment (purple arrows in Figure 2.1). Entrainment and detrainment are typically accounted for using an insoluble tracer, e.g. n-butane, that is not altered by chemistry or scavenging over a

storm's lifetime, by normalizing the soluble species to the insoluble tracer thus accounting for entrainment and detrainment (e.g., Fried et al., 2016).

Transport and SE of the soluble trace gas species hydrogen peroxide (H_2O_2), methyl hydroperoxide (CH_3OOH), and formaldehyde (CH_2O) were evaluated for different DC3 storms (Barth et al., 2016; Bela et al., 2016, 2018; Fried et al., 2016). One case study was an airmass storm sampled at the Alabama/Tennessee border on May 21, 2012 (Bela et al., 2016, 2018; Fried et al., 2016). Fried et al. (2016) found a significantly higher formaldehyde SE (81$\pm$5%) for the airmass storm relative to larger DC3 storms (48-67%). Fried et al. (2016) remarked the potential disconnect between inflow and outflow measurements based on butane and pentane ratios. It was also suggested the high formaldehyde SE could be due to aqueous chemistry. Formaldehyde is considered the primary aqueous chemistry source for formic acid (HFo); therefore, HFo production would be a formaldehyde sink. While a formaldehyde aqueous chemistry sink was mentioned, Fried et al. (2016) simulations did not include this formaldehyde loss and HFo source.

Prior modeling work suggested that clouds could be a significant source of HFo (Jacob, 1986) via an aqueous CH_2O - HO reaction although observational evidence is mixed. Laj et al. (1997) reported a pH dependent aqueous production of HFo and release to the gas phase. Keene et al. (1995) found that clouds are a net sink for HFo and fail to provide significant production. HFo and the other dominate carboxylic acid, acetic acid (HAc), are considered to be significantly scavenged in clouds via wet deposition (Paulot et al., 2011) but this scavenging is pH dependent. When the pH is lower than 5, aqueous HFo is volatilized to the gas phase (Jacob,

1986) and cloud production could provide a UT HFo source. For completeness, the primary aqueous production of HAc is from pyruvic acid (Carlton et al., 2006) and aqueous HAc production is not considered to be a significant source of HAc (Jacob & Wofsy, 1988) to the atmosphere.

While there are uncertainties regarding the possibility of aqueous phase production, both organic acids have natural and anthropogenic gas phase sources including biogenic emissions, motor vehicle exhaust, agricultural emissions, and biomass burning (Khare et al., 1999; Paulot et al., 2011). Secondary gas phase production from biogenic precursors is considered to be a significant source for both organic acids though full reaction mechanisms and yields remain uncertain (Millet et al., 2015; Paulot et al., 2011; Yuan et al., 2015). In addition, both acids help set the natural acidity of rainwater. HFo and HAc comprise 16% and 64% of the volume weighted free acidity of precipitation in urban (Keene & Galloway, 1984) and remote (Keene et al., 1983) regions, respectively. It is likely that with decreasing SO_x and NO_x emissions the acid composition of precipitation has changed with organic acids playing a larger role even in urban regions.

Wet and dry deposition are the dominant organic acid sinks (Paulot et al., 2011). Because of this, traditionally HFo and HAc are thought to be removed through convective systems. If HFo and HAc were transported to the UT, their lifetime would increase from a few days to 20+ days as the main gas phase sink is reaction with HO which is quite slow (Paulot et al., 2011). To our knowledge, there have been no convectively influenced UT measurements of either organic acid in the United States on storm timescales. Talbot et al. (1990) reported a 200+ ppt increase in HFo

measured in convective outflow over the Amazon that was not seen in HAc. Convective outflow was sampled on two separate occasions but there was only an increase in HFo for one flight (Talbot et al., 1990). This suggests that there were different processes for the two storms which impacted HFo scavenging differently. Treadaway et al. (2018) reported the successful UT measurement of HFo and HAc during DC3 using the peroxide chemical ionization mass spectrometer (PCIMS). During the May 21st flight, the PCIMS detected a higher than expected plume in HFo (700 ppt) near convective outflow. This peak in HFo was not associated with the convective outflow discussed by Bela et al. (2016; 2018), Fried et al. (2016), and Li et al. (2017). A difference in HFo outflow suggests the potential for a different inflow chemical composition or different storm dynamics.

HAc measurements are confounded by a potential isobaric interference from hydroxyacetaldehyde, or glycolaldehyde (GA). PCIMS data collected as HAc is now operationally defined as the acetic acid equivalent sum (AAES). There are limited GA measurements and we are unaware of any published results for GA above 3 km. Lee et al. (1998) reported a GA vertical profile up to 3 km in the southeastern United States in a region with mixed biogenic and anthropogenic emissions. They found GA in the lower free troposphere had a pronounced decrease in concentration from that in the boundary layer. This was attributed to scavenging by cloud droplets due to its high solubility.

This paper examines the potential for HFo, HAc, and GA transport and transformation to the UT for the airmass case study using observations and model results. Here we combine observations and model results from the Weather Research

and Forecasting Model coupled with chemistry (WRF-Chem) and a photochemical box model (Barth et al., 2003; 2016) to investigate potential causes for the HFo peak noted aloft. WRF-Chem simulations provided insight into potential SE changes for organic acids for isolated convection compared to a convective complex. The WRF-Chem simulations are also used to discuss the likely HAc and GA contributions to the AAES measurements and how both are transported through the airmass storm. The box model is used to discuss the influence of pH and HFo aqueous production on HFo gas phase mixing ratios.

2 Methods

2.1 Campaign Info

The Deep Convective Clouds and Chemistry (DC3) Experiment was conducted in May and June 2012 over the continental United States focused in Colorado, west Texas to central Oklahoma, and Alabama. There were three instrumented aircraft that participated in DC3: the German Aerospace Center (DLR) Falcon, the National Aeronautics and Space Administration (NASA) Douglas DC-8, and the National Science Foundation (NSF) National Center for Atmospheric Research (NCAR) Gulfstream-V aircraft (GV). In addition to the three aircraft, ground stations recorded lightning location and storm properties with radars, and mobile units released weather balloons. A description of the program and available platforms can be found in Barth et al. (2015). The meteorological data used in this work was described in detail in Manuscript 1. The radar source was the Next Generation Weather Radar (NEXRAD) Weather Surveillance Radar-1988 Doppler (WSR-88D) stationed at Hytop, Alabama

(KHTX). The NEXRAD horizontal radar profiles presented were prepared using the NOAA Weather and Climate Toolbox and Google Earth with the NEXRAD data.

2.2 Aircraft Measurements

Aircraft measurements for chemical, aerosol, and cloud physics parameters were collected by the NASA DC8 and NSF/NCAR GV. A list of the species used in this study, instruments, and detection information are in Tables 2.1 and 2.2. Inflow measurements were obtained by the DC8 (Table 2.1). Outflow measurements were obtained with the GV (Table 2.2). CO and O_3 were used to remove stratospherically influenced air (O_3/CO > 1.25) from GV outflow measurements. Aircraft samples were also categorized as clear or cloudy. This was determined using liquid water content (LWC) and ice water content (IWC) on the GV. Only IWC was measured on the DC8 and a subjective cloud indicator was used for portions of the flight when IWC or LWC was unavailable. The cloud indicator is based on the front facing camera and is not as reliable for thin or patchy clouds. The extent of entrainment was determined using n-butane as it serves as an insoluble tracer gas over the lifetime of the storm following Fried et al. (2016) and Bela et al. (2016; 2018). An in-depth discussion of the CH_2O instrument intercomparison during DC3 is presented in Fried et al. (2016). Barth et al. (2016) mentioned a disagreement between the peroxides measurements onboard the DC8 and GV. Peroxide results with both aircraft should be taken with caution.

The observed scavenging efficiencies (SE) for soluble trace gases including CH_2O, H_2O_2 (HP), CH_3OOH (MHP), CH_3COOH (HAc), HCOOH (HFo), HNO_3, and SO_2 were estimated from DC8 and GV measurements as outlined below (Section

2.4). There are two caveats to the organic acid measurements presented. First, as discussed in Treadaway et al. (2018) the GV measurements for HAc must be represented as acetic acid equivalent sum (AAES) as the measurements for that mass represent a combination of HAc and GA. The possible division between HAc and GA will be evaluated with literature data and model results (Section 4.2). Second, there were no reported organic acid measurements on the DC8. Inflow measurements for HFo and AAES were estimated from 1) the GV spiral over Tennessee as representative of the region and 2) HFo measurements collected during the summer 2013 SENEX (Southeastern Nexus) campaign. HFo SENEX measurements from two CIMS instruments (Lee et al., 2014; Neuman et al., 2002, 2010) below 1000 m between 35 and 36 ^{o}N and -85 and -87.5 ^{o}W were averaged to represent the inflow region.

2.3 Simulation Set-up and Model Description

This study used the Weather Research and Forecasting Model version 3.7 coupled with chemistry (WRF-Chem). The model set-up details are presented in Table 2.3 and briefly described here. Simulations were run with one-way nesting for the three domains. There were 40 vertical levels with a model top of 70 hPa. The simulation was started before the analysis time to allow the chemistry and physics to stabilize. The 15 km domain used the Grell 3D cumulous parameterization (Grell, 1993; Grell & Dévényi, 2002) and the 3 km and 0.6 km treated convection explicitly. The WRF-Chem simulation set-up was the same as Bela et al. (2016; 2018) and Li et al. (2017) with the exception of the lightning data assimilation temperature range, cloud microphysics scheme, and chemical mechanism.

The Morrison double moment scheme was used for cloud microphysics for reasons outlined in Manuscript 1. Lightning data assimilation was used following the Fierro et al. (2012) and Li et al. (2017) methods and modified as discussed in Manuscript 1. These simulations used the Model for Ozone And Related chemical Tracers version 4 gas phase chemical mechanism with the Model for Simulating Aerosol Interactions and Chemistry aerosol mechanism (MOZART-MOSAIC). The coupled MOZART-MOSAIC chemistry includes aqueous chemistry where T>258 K (-15^{o}C) (Fahey & Pandis, 2001). As discussed in Manuscript 1 with the addition of chemistry and aerosols the lightning data assimilation temperature range had to be increased to 261 – 291 K to promote convection.

Biogenic emissions data used the Model of Emissions of Gases and Aerosols from Nature v2.04 (MEGAN; Guenther et al., 2006). Fire emissions were generated from the Fire INventory of NCAR (FINN; Wiedinmyer et al., 2011). This is based on MODIS fire count data with 1 km horizontal grid spacing, and plume rise was calculated online every 30 min. Anthropogenic emission data were from the 2011 National Emissions Inventory (NEI).

The WRF-Chem wet deposition scheme is based on the Neu and Prather (NP) method (Neu & Prather, 2012). The trace gas removal is calculated by multiplying the effective Henry's Law equilibrium aqueous concentration by the net precipitation formation (defined as the conversion of cloud water to precipitation minus evaporation of precipitation). Because WRF-Chem does not keep track of aqueous or ice chemical mixing ratios between grid cells or time steps, this removal scheme results in an overestimation of wet removal. For example, if a trace gas is scavenged to the aqueous

phase it is not possible to re-release the gas when the hydrometeor evaporates or freezes.

The WRF-Chem results discussed here are with zero ice retention. Although Bela et al. (2018) tested five different ice retention factors, they could not determine ice retention coefficients for the May 21st storm due in part to the simulated storm's large scavenging efficiency standard deviations. Ice retention was eliminated from these simulations to limit the interplaying variables though this should be investigated in the future in combination with aqueous chemistry. For a discussion on the impacts of ice retention on trace gas transport see Bela et al. (2018).

WRF-Chem was unable to produce sufficient HFo (Section 4.1). Peroxide chemical ionization mass spectrometer HFo median altitude profiles in the boundary layer (BL) and free troposphere (FT) were used as the HFo altitude profile implemented into WRF-Chem following the same method as Bela et al. (2016). BL was defined as altitude $\leq$ 2 km and q_{total} < 0.01 g/kg from 21:00 – 22:00 UTC which was during a spiral before returning to base. FT was defined as altitude > 3km, q_{total} <0.01 g/kg, and O_3/CO<1.25, from 17:00-19:00 UTC. The lowest altitude median was applied for all model layers below GV measurements down to the surface. The GV focused on storm outflow therefore not all altitude bins had HFo measurements. For altitude bins without measurements, the median from the bin below was used. This is why the HFo background profiles (Figure 2.3) decrease < 20 ppt from 3-7 km. For altitudes above the aircraft, results from the global chemistry transport model MOZART (Emmons et al., 2010) were used.

2.4 Observational Scavenging Efficiency Calculation

The observed inflow and outflow times are from Bela et al. (2016) and Fried et al. (2016) and referred to as the literature times for the convective complex. The DC8 measured inflow from 19:30:43 – 19:38:00 UTC at 1.18 – 1.22 km. The inflow period only includes cloud free points. The GV outflow period was from 20:50:30 – 21:14:30 UTC at 10.04 – 10.06 km for cloudy points (q_{ice} > 0.01 g/kg) and stratospheric air removed (O_3/CO>1.25). This work uses the n-butane scavenging efficiency (SE) method (e.g. Bela et al., 2016; Fried et al., 2016). This determines SE based on the inflow and outflow soluble species mixing ratios relative to n-butane. n-Butane is transported and not changed chemically during the time period of transport from the BL to the top of the storm. However, entrainment will alter n-butane mixing ratios as air moves from cloud base to top. Therefore its mixing ratio will not be the same in the inflow and outflow regions because of entrainment. The n-butane method calculates SE using the average ratio of the soluble species to n-butane for the inflow and outflow for all observations meeting the above criteria as shown below.

$$SE\ (\%) = 100 * (1 - \frac{mean\frac{S_j}{n\text{-}butane_j}_{outflow}}{mean\frac{S_j}{n\text{-}butane_j}_{inflow}}) \qquad (2.1)$$

S_j and n-$butane_j$ are the individual observed mixing ratios (ppb) for n-butane and other chemical species S. The n-butane mixing ratio is assumed to be negligible in the entrained air. All variables introduced are in the list of abbreviations at the beginning of the dissertation.

Another possible SE method calculates the entrainment rate (%/km) throughout the storm. See Fried et al. (2016) for a detailed description of this method. It requires a background air profile (obtained from the DC8 for the whole flight), the

inflow mixing ratio, and outflow mixing ratio. Through iterations the entrainment rate is found for n-butane, i-butane, n-pentane, and i-pentane. Fried et al. (2016) only used n-butane for the altitude entrainment method for the May 21st storm due to discrepancies between the inflow and outflow mixing ratios for the other species. This study only determined the observed SE with the n-butane method. The WRF-Chem entrainment rate will be compared to the Fried et al. (2016) entrainment rate in Section 4.4.

2.5 WRF-Chem Scavenging Efficiency Calculation

The WRF-Chem SE method used here differs from Bela et al. (2016; 2018) and Barth et al. (2016). They calculated SE for the WRF-Chem grid points corresponding to the location and timing of the observed outflow sampled by the GV. Due to the difference in microphysics scheme and chemical mechanism the location and timing of the simulated storm differed from observed storm and, as a result, the observed outflow region was not near the simulated storm. In addition, as discussed in Manuscript 1 the simulation set-up differences resulted in the primary storm being produced 30 minutes after the observed storm. For these reasons WRF-Chem SE used a chemical characterization based on HNO_3 and NH_3 for a defined storm region. A chemical threshold for HNO_3 (SE>60%) and NH_3 (SE>=10%) was used. SE values were determined for a box encompassing the whole storm and only included model grid points where the summed mass mixing ratio of cloud water (q_{cloud}) and ice (q_{ice}) was greater than 0.01 g/kg.

Historically, HNO_3 and SO_2 oxidation (H_2SO_4) control the pH of precipitation with some neutralization by NH_3 (Charlson & Rodhe, 1982; Galloway et al., 1982).

HNO_3 was chosen as the acidic SE threshold because it was measured onboard the DC8 and GV unlike SO_2. Different HNO_3 SE thresholds were tested (20, 40, 60, and 80%) and it was found that 60% best replicated the observed HNO_3 SE (~75%) for the convective complex. The isolated convection had a lower HNO_3 SE but the WRF-Chem HNO_3 average SE was around 70% regardless of the threshold. Lowering the threshold only increased the variance. The NH_3 criterion was chosen because it is the primary base neutralizing precipitation acidic chemical species (e.g. HNO_3). The overall SE for the different soluble species did not change drastically with or without the NH_3 criterion. However, with this additional parameter the variance was smaller as large outlying SE values were eliminated.

SE was calculated for a box encompassing the storm and extending vertically from 8 – 11 km for the convective complex and 6 – 9 km for the isolated convection. This expands the SE area from previous literature work that used the grid cells closest to the aircraft sampled outflow location. WRF-Chem SE values for species *j* were calculated using the mean outflow mixing ratios (q) for a simulation with precipitation scavenging on ($q_{j,scav}$) and a simulation with precipitation scavenging off ($q_{j,noscav}$).

$$SE\ (\%) = 100 * (\frac{q_{j,noscav} - q_{j,scav}}{q_{j,noscav}}) \qquad (2.2)$$

SE was averaged for the entire outflow period. The convective complex outflow period was from 21:30 – 21:50 UTC. The isolated convection outflow period was from 21:00-21:20 UTC.

2.6 WRF Passive Tracers

Passive tracers were used to calculate the entrainment ratio through the simulated storm. Tracers were released in 1-km bins from the surface to 20 km (Barth

et al., 2016; Bela et al., 2016). Tracers were set to 1.0 in clear air outside the storm defined by total water mixing ratio (q_{total}) < 0.01 g/kg (Bela et al., 2016). This was done for one time step an hour before the end of the outflow period for a box encompassing the storm. For example, the convective complex tracers were released from 20:40-20:50 UTC for the 21:30-21:50 UTC outflow period. Entrainment was calculated by taking the average percent contribution of each 1 km altitude layer within the outflow box described in Section 2.5. This was done for all points that met the chemical scavenging criteria (HNO_3 SE>60%, NH_3 SE>=10%, and $q_{cloud} + q_{ice}$ > 0.01 g/kg) and at the top of the storm core which is defined as within the 40 dbz radar contour.

2.7 Box Model

The impact of aqueous chemistry, temperature, and pH on organic acid distribution were evaluated using a gas-aqueous box model described by Barth et al. (2003; 2016). The box model uses WRF-Chem output data for the liquid water content, hydrometeor partitioning, temperature, pressure, and altitude. The initial chemical conditions are set by WRF-Chem output results as well. The WRF-Chem data were averaged at each model level during the outflow period for the storm box when vertical velocity was greater than 5 m/s. The box model simulation is run for 10 minutes in the boundary layer to reach photochemical equilibrium. The photolysis rates vary with altitude and are based on 36 ^{o}N at 12 UTC time (approx.0700 local time). The photolysis rates are adjusted to account for cloud scattering assuming a cloud optical depth of 500 m, cloud base of 2 km, and cloud top of 15 km. Supplemental Table 2.1 lists the aqueous phase reactions for HFo, HAc, and GA. The

Henry's Law gas-aqueous equilibrium coefficients come from Sander (2015). The box model has only aqueous reactions and not gas phase reactions for HFo. While WRF-Chem only has the CH_2O to HFo aqueous formation pathway, the box model also includes additional sources and sinks. Neither WRF-Chem nor the box model included heterogeneous reactions, e.g. $CH_2OO + H_2O$, which is potentially a large HFo source. It is likely both models underpredicted HFo.

3 Meteorological and Chemical Description of the Observed Storm

The Alabama airmass storm meteorology has been described in detail in Mecikalski et al., (2015), Bela et al. (2016), Li et al. (2017), and Manuscript 1, among others. The meteorological foundation of the Alabama storm simulation was discussed in Manuscript 1 including comparisons to previous simulations (Bela et al., 2016; Li et al., 2017) and observations (Mecikalski et al., 2015). This was a critical step necessary before the chemical discussion presented here. Thus, only a brief meteorological overview is presented with the necessary context to understand the chemistry.

On May 21, 2012, Research Flight 03 (RF 03), the objective was to sample airmass storms in the Alabama region. The storm of interest, referred to as B2 here and in Mecikalski et al. (2015), was part of the second round of convection that day. B2 formed in Tennessee by the merging of two smaller storms at 20:15 UTC and by 20:20 UTC the maximum vertical velocity was 12 m/s. Unlike the other DC3 case studies, the May 21st storm was an airmass storm, characterized by vertical velocity less than 20 m/s and a much smaller horizontal scale relative to a mesoscale convective storm or supercell (Barth et al., 2015).

Figure 2.2a shows the flight path for the GV and DC8 for RF 03. While waiting for a storm to initiate the DC8 and GV flew a trapezoidal pattern at different altitudes to characterize the chemistry of the region. As isolated convection began the GV flight path was altered to sample the outflow region in a southwest-northeast wall flight pattern. The DC8 inflow period, 19:30 – 19:38 UTC, is defined as a boundary layer flight leg where the wind is moving into the storm (Bela et al., 2016; Fried et al., 2016). For May 21st, this time period is before the formation of B2. This still should serve as representative sampling of the region and this will be discussed further in Section 4.5. As B2 moved southward towards the Alabama border and decayed, it formed a convective complex, shaped like a ring, with other small storms in the region. The GV sampled this convective ring during the outflow period (20:50 – 21:15 UTC) which is defined as cloudy flight segments where the wind is coming from the storm core towards the GV (Bela et al., 2016; Fried et al., 2016).

Figure 2.2b shows the HFo and AAES time series for RF 03 shown as the 1 minute moving average with stratospheric air removed (O_3/CO>1.25). There was an increase in both species during a spiral down to 0.96 km on the way back to base (21:40 UTC). This spiral will be used later for a scavenging efficiency comparison (Sections 4.5 and 4.6). AAES was highly variable throughout the whole flight and was greater than HFo with one exception. During the southeast-northwest wall pattern, the GV flew past an isolated storm northeast of B2 with an enhancement in HFo (20:00 UTC) but with no similar peak detected in available GV measurements. While this storm was not the primary target and was on the edge of the KHTX radar it appears to be a roughly similar size and strength to B2 based on maximum column radar

reflectivity. Figure 2.3 shows the HFo measured from 20:00-21:00 UTC overlaid on a Google map with the maximum column radar reflectivity for 19:46 UTC. This is 15 minutes before the HFo peak and shows a storm just south of the elevated HFo that was decaying by 20:00 UTC. The wind direction was from the storm towards the GV during the elevated HFo sampling period.

4 Results and Discussion

4.1 Formic acid model and observation discrepancy

WRF-Chem HFo mixing ratios are substantially lower than expected, less than 10 ppt, throughout the background profile and storm outflow. Observed HFo ranged from 28 – 724 ppt. Other authors have found similar discrepancies between observed and modeled HFo (e.g. Millet et al., 2015; Yuan et al., 2015). Yuan et al. (2015) found that a box model based on the Master Chemical Mechanism underestimated HFo by a factor of >10 based on observations at two ground sites measuring urban and oil and natural gas production. Millet et al. (2015) found a 2-3 times underestimation in GEOS-Chem (Goddard Earth Observing System) HFo for summertime boundary layer in the southern U.S. during SENEX. Both authors discuss that this discrepancy is mostly due to models missing secondary formation sources for HFo.

WRF-Chem MOZART gas phase mechanism has 10 gas phase production reactions for HFo. Biogenic precursor reactions with ozone include a-pinene, b-pinene, limonene, myrcene, methylbutenol (MBO), and b-caryophyllene. All biogenic reactions have a 5% yield of HFo with the exception of MBO which has a 25% HFo yield. The two non-biogenic sources are ethene and ethyne (acetylene). Ethene reacts with ozone to form HFo with a 50% yield. Acetylene reacts with HO to form HFo

with a 35% yield. The last two reactions involve the radical $HOCH_2OO$, from formaldehyde, reacting with NO and HO_2 in a 1:1 reaction. The only gas phase HFo sink is the reaction with HO.

A HFo pseudo steady state (pss) mixing ratio was calculated using the MOZART reactions and available low altitude aircraft data. DC8 Whole Air Sampler (WAS) data during the inflow period were used for ethene and acetylene. GV TOGA data during the spiral were used for a-pinene, b-pinene, and MBO. The pss mixing ratio was determined for each HFo formation reaction and the total production based on DC8 and GV data were summed separately. There was no wet or dry deposition accounted for in this approximation. Some minor source species measurements were unavailable during the inflow period, e.g. limonene, mycrene, beta-caryophyllene, and $HOCH_2OO$. However, measurements of the main MOZART gas phase sources, e.g. ethene, acetylene, and MBO, were available. The majority of the pss HFo came from ethene and acetylene (205 $\pm$ 12 ppt) with an additional 19 $\pm$ 0.4 ppt attributed to biogenic sources. For comparison, the measured HFo during the GV spiral was 332 $\pm$ 15 ppt. While the MOZART mechanism appears to do reasonable job of capturing the HFo mixing ratio it was still lower than observed. If deposition was included, the calculated pss would be even lower still, further increasing the discrepancy between observed and calculated. Paulot et al. (2011) estimated an HFo combined wet and dry deposition sink that was 4 times the photochemical sink. The HO reaction photochemical loss rate was 0.014 day^{-1} using GV data. Based on Paulot et al. (2011), the combined wet and dry deposition was 0.056 day^{-1}.

The biogenic pss was recalculated assuming a 31% HFo yield from the isoprene ozonolysis (Yuan et al., 2015). The new mixing ratio (570 $\pm$ 196 ppt) was substantially higher though with a much larger standard deviation. This large standard deviation is due to only having two isoprene measurements (602 and 292 ppt) during the GV spiral as a result of TOGA's two minute sampling rate. If only the lower isoprene measurement is used, the biogenic HFo pss is 363 $\pm$ 13 ppt - much closer to the observed HFo mixing ratio (332 $\pm$ 15 ppt). The isoprene ozonolysis reaction produces the Criegee biradical which reacts with water to form HFo. This improved production supports previous work, e.g. Millet et al. (2015) and Yuan et al. (2015), showing that the Criegee biradical is important for HFo secondary production.

This analysis was expanded beyond the low altitude data to encompass the whole flight. HFo pss mixing ratio was calculated the same as above with the addition of limonene. The HFo pss mixing ratio presented here used the maximum value representing an upper limit. This includes the MOZART reactions plus the 31% yield from isoprene ozonolysis. Figure 2.4 compares the observed HFo to the maximum HFo pss mixing ratio for the isoprene ozonolysis, anthropogenic precursors (ethene and acetylene), and biogenic precursors (a-pinene, b-pinene, limonene, and MBO). The production from the combined biogenic sources is negligible for the majority of the HFo range. The total calculated HFo is overestimated when the observed HFo was between 300-400 ppt. This is not surprising as there was no deposition. Yet the modeled production sources do not capture the observed high end of HFo (greater than 500 ppt) which includes the high altitude peak in HFo. If there was no isoprene production, as is the case for MOZART, the maximum possible calculated HFo was

~200 ppt – less than half what was observed. Millet et al. (2015) saw similar discrepancies for the high HFo measurements (greater than 1 ppb). Without the addition of isoprene HO oxidation, GEOS-Chem did not exceed 500 ppt and even with isoprene simulated HFo was up to 5 times underpredicted (Millet et al., 2015).

While it is likely there are missing HFo source terms, it is also important to consider how WRF-Chem replicates the mixing ratios for the available sources. Using observational precursors resulted in a similar order of magnitude between calculated and observed HFo. Consequently, it is likely that part of large inconsistency between WRF-Chem and observations could be due to underestimating a precursor source as well. Based on the pss calculations acetylene dominates the HFo production (159$\pm$10 ppt). DC8 inflow data for acetylene (~1 km) was 293 $\pm$ 21 ppt. However, for the simulated 1-2 km bin acetylene was 0.029 $\pm$ 0.0876 ppt. Clearly, this is quite a large difference in mixing ratios for a dominate HFo source in the MOZART mechanism. Acetylene comes from NEI anthropogenic emission data. Acetylene's lifetime is greater than the timescale of the simulation (20+ days); therefore, if acetylene emissions were accurately represented it should have been significantly closer to observations. In comparison, the ethene simulated mixing ratio in the 1-2 km bin was 105 $\pm$ 87 ppt and DC8 inflow average was 89$\pm$14 ppt. Therefore, while there are certainly missing gas phase sources in MOZART, if a precursor is underestimated it will impact secondary formation reactions. Until there is a better understanding of HFo sources WRF-Chem should be modified with observational data when available. Here WRF-Chem was modified with a GV HFo median altitude profile described in Section 2.3.

4.2 HAc and GA

The HAc PCIMS signal is sensitive to an isobaric interference from GA and the mass signal associated with HAc is reported as the acetic acid equivalent sum (AAES). Unfortunately, there is currently no pure GA standard available. GA is sold as the solid dimer and when dissolved in water leads to an aqueous mixture of monomer, dimer, and trimer. Treadaway et al. (2018) discussed two different methods used to quantify the GA PCIMS sensitivity. The PCIMS sensitivity was tested using an aqueous solution and Henry's Law constants and equilibrium work from Betterton and Hoffmann (1988) and Kua et al. (2013). This resulted in a 1:1 HAc:GA sensitivity for PCIMS indicating that AAES measurements represented a true sum of HAc and GA. Treadaway et al. (2018) also used melt "vapor pressure" experiments based on the work of Petitjean et al. (2010) and Magneron et al. (2005). Based on the melt experiments, the HAc:GA sensitivity was 1:10. Thus AAES would represent an upper limit to the sum of HAc and GA. If AAES was only GA then the reported AAES as HAc would overestimate GA by a factor of 10.

DC3 HAc PCIMS measurements must be reported as AAES representing a mixture of HAc and GA. This mixture is not known and unfortunately there are limited prior measurements available for HAc and GA in this region with which to compare to PCIMS. Treadaway et al. (2018) estimated HAc and GA mixing ratios based on literature data and the two PCIMS HAc:GA sensitives. The estimated HAc:GA ratio for the Southeastern United States based on literature surface data ranged from 0.9 to 10 and when using aircraft data from 1 to 14 (Khare et al. 1999;

Lee et al., 1995; Lee et al. 1998; Talbot et al. 1995). This indicates that previously collected data had at least equal mixing ratios with HAc likely to be greater than GA.

Here we estimate HAc and GA mixing ratios measured as AAES based on literature data. Table 2.4 compares potential HAc and GA mixing ratios with two different literature ratios at the low (1:1) and high (14:1) end of prior observations. The literature 1:1 ratio indicates there are equal proportions of HAc and GA measured. The 14:1 ratio means that for every 14 ppb HAc present there is 1 ppb GA. These literature ratios are convolved for the two different PCIMS sensitivity ratios and the GV whole flight AAES median of 0.450 ppb to estimate the potential proportionality of HAc and GA measured as AAES during RF 03 (Table 2.4). With the exception of using both 1:1 ratios, the AAES measurement would have been dominated by HAc by at least a factor of 10. Talbot et al. (1995) measured between 0.17 and 6.3 ppb HAc from a tower in Shenandoah National Park. Lee et al. (1998) measured a maximum GA of 2.8 ppb in the BL with an average of 0.15 ppb above the BL. It is unlikely that GA measurements were less than 0.04 ppb as estimated in Table 2.4. AAES could represent equal measurements of HAc and GA of 0.24 ppb but more likely it is in between the extremes presented here.

In addition to the literature measurements, relative proportions of HAc and GA were estimated with WRF-Chem results using both the background profiles defined in Section 4.3 and the convective outflow average mixing ratios for the convective complex and isolated convection. The convective outflow HAc and GA mixing ratios were within 100 ppt of each other thus the ratios were about 1:1. Figure S2.1 shows the HAc:GA ratio for the WRF-Chem north and south background profiles discussed

in Section 4.3 with a 1:1 line. The ratio is greater than 1:1 below 8 km. Only above 8 km does the ratio fall below the 1:1 line in the northern profile corresponding with the GA increase (Figure 2.5a). The increase in the ratio above 11 km corresponds to less than 10 ppt for both so does not reflect what would be measurable. WRF-Chem results support literature measurements that found similar mixing ratios between HAc and GA with it more likely that HAc would be greater than GA.

If AAES was only GA and there was a 1:10 sensitivity then GV GA median would be 0.045 ppb which is lower than the previously reported data for the region and what was predicted by WRF-Chem. Based on this assessment the PCIMS sensitivity likely represents closer to a true sum. Previous measurements and WRF-Chem results suggest greater HAc relative to GA in the BL but equal proportions above the BL.

4.3 WRF-Chem Background Profiles

Non-convective air chemical profiles are important as they help us understand the general chemical composition for the region and what could be entrained into the storm. The data chosen were in clear air (q_{cloud} <0.01 g/kg and q_{ice} < 0.01 g/kg) for a 324 km^2 box. Two regions were chosen that were to the north and south of modeled convective storms to give a general representation of the region. Figure 2.5 shows WRF-Chem background mixing ratios for HAc, HFo, and GA for the northern profile (Figure 2.5a) and southern profile (Figure 2.5b). Figure S2.2 has the background mixing ratios for HP, MHP, and CH_2O for both the northern (Figure S2.2a) and southern (Figure S2.2b) regions. The increase in HFo at 11 km could be the result of

using GV data with the drop-off above 11 km the switch to MOZART global data (above 12 km).

Background air appeared to be convectively influenced, e.g. GA increased around 10 km in both profiles and HAc increased in the southern profile around 10 km. This convective influence and mixing are why two profiles are used to characterize the region. As a check that this is not UT gas phase chemistry, a simulation without gas phase chemistry was performed. The background profile structure was similar with and without gas phase chemistry. This indicates that the chemical profile was due to mixing and not *in situ* production.

4.4 Entrainment Fraction

WRF-Chem passive tracers are used to calculate the lateral entrainment rate through the simulated storms as defined in Section 2.6. The storm core entrainment rate was calculated for the convection complex (Figure 2.6a) and isolated convection (Figure 2.6b). The entrainment rates were calculated over a large area encompassing the whole storm and included model points where radar reflectivity was greater or equal to 40 dbz from 7-10 km and 6-9 km for the complex and isolated convection, respectively. Barth et al. (2016), Bela et al. (2018), and Fried et al. (2016) calculated the WRF-Chem entrainment rate for model points greater than 40 dBZ but only points directly upwind from the aircraft outflow sampling location.

The WRF-Chem convective complex average entrainment rate is shown as the blue line in Figure 2.6 with the Fried et al. (2016) average (0.089+0.027/km) as the red line. Despite the differences in storms and entrainment area calculations the WRF-Chem convective complex average entrainment rate (0.10$\pm$0.092/km) was the same as

Bela et al. (2018) (0.10±0.092/km). The convective complex entrainment was relatively evenly distributed from 0-6 km with the highest fraction coming from the 0-1 km bin. This differed from Bela et al. (2018) where the highest entrainment was at 5-6 km (0.19) and 9-10 km (0.27).

The majority (~0.7) of the entrainment for the isolated convection came from the bottom 2 km. The rest of the entrainment came from mostly the 4-5 km bin. The isolated convection average entrainment rate (0.11±0.17/km) was similar to the convective complex. The cloud top height for the isolated convection was 6-8 km which is why there was no entrainment at higher altitudes.

4.5 Scavenging Efficiency of Convective Complex

Table S2.2 shows the values used to calculate scavenging efficiency (SE) for the convective complex (observation and WRF-Chem). The observational SE calculations represent downwind SE where the outflow measurements were collected and not the storm core. This differs from Fried et al. (2016) who discussed the SE at the storm core. Fried et al. (2016) also discussed the disconnect between the inflow and outflow measurements for the May 21st storm based on the pentane ratios. Butane and pentane ratios are commonly used to match inflow and outflow periods because they have a low reactivity for the convective transport scale (less than 30 minutes) and low solubility. They also have lower mixing ratios in the UT than BL with few chemical sources outside the BL (Fried et al., 2016). Given that the GV sampled the outflow of a convective complex and not an isolated storm an hour after the inflow measurements it is reasonable that there was a disconnect between the inflow and

outflow chemical signatures. For this reason observational SE calculations were performed for the downwind SE instead of tracing back to the storm core.

Given the change in storm structure and time between the DC8 inflow measurements and GV outflow measurements, the DC8 inflow serves as a characterization of the region. Species that were only present onboard the GV, ex. HFo and AAES, were not measured during the DC8 inflow period; therefore, the GV spiral is used as a second representative inflow. GV measurements from the spiral on the way back to base (170 km west of storm) provided inflow measurements over Tennessee for HFo, HAc, CH_2O, and HP. MHP was not available. The DC8 inflow period was before the convection and that from the GV was after. The GV inflow measurements may be lower than DC8 for more soluble species. The discrepancy in pentane ratio (Table 2.5) between the DC8 inflow and GV outflow reflected potentially different airmass source (Fried et al., 2016). When using the butane and pentane ratios for the GV spiral, the inflow and outflow pentane ratio align (Table 2.5). Therefore it is reasonable to assume that the GV spiral inflow region was of a similar chemical composition to the airmass sampled in the outflow.

Figure 2.7 presents the average SE for organic acids and the soluble species reported in Bela et al. (2016; 2018) for both observations and WRF-Chem simulations along with one standard deviation. The observational data in Figure 2.7 used the Bela et al. (2016) defined inflow and outflow flight segments, the GV spiral as a representative inflow, and SENEX data for HFo inflow. The WRF-Chem SEs were calculated as the difference between two simulations, one with wet scavenging and one without. WRF-Chem SEs were averaged from 21:30 – 21:50 UTC. The AAES

GV spiral SE is listed for both HAc and GA in Figure 2.7 as it is some combination of both. Simulation results are for WRF-Chem with and without cloud aqueous chemistry. SE was higher for all species with aqueous chemistry although the standard deviation was greater than the difference between SE with and without aqueous chemistry. The SE with aqueous chemistry was higher because aqueous reactions let to an aqueous loss of the species allowing more dissolution from the gas phase as the equilibrium shifted.. The WRF-Chem HNO_3 SE criterion is based on the measured HNO_3 SE of 75 $\pm$ 7.4%. A threshold of 60% ensures a reasonable sampling region compared to measured but does not assume WRF-Chem scavenging has to be as high as observed (i.e. setting it to 75%). The 10% NH_3 SE threshold prevents too strict of an SE criterion since there was no measured NH_3 SE to compare to as with the HNO_3 criterion. The choice of 10% ensured that the grid cells had some basic chemical scavenged from the gas phase preventing the inclusion of model points with unrealistic scavenging. Adding the NH_3 criterion did not substantially change the overall SE but it did lower the standard deviation by removing unrealistic SE values.

As mentioned in Section 2.5 all chemicals in these WRF simulations were prescribed to have an ice retention of zero. Bela et al. (2018) discussed different retention factors and how the soluble species responded differently to the ice retention. Bela et al. (2018) did not determine the best soluble species ice retention coefficients for the May 21st storm due to discrepancies between the inflow and outflow chemical signatures for the observed storm and large standard deviation for the SE of the simulated storm. This study did not use the same observed location to determine the SE so a direct comparison cannot be made between this work and Bela et al. (2016;

2018). In addition, Bela et al. (2016; 2018) simulations and this one used different cloud microphysics schemes as discussed in Manuscript 1 which impact the hydrometeors– and thus the trace gas scavenging.

Bela et al. (2018) reported the WRF-Chem predicted SE for the different ice retention factors. The 0 ice retention simulation had MHP (0$\pm$45%), HP (8$\pm$28%), CH_2O (3$\pm$34%), HNO_3 (20$\pm$22%), and SO_2 (-14 $\pm$ 148%). Based on HNO_3 this work aligns with an ice retention of 0.5 – 1. Bela et al. (2018) found that CH_2O and HP were not sensitive to ice retention as CH_2O was nearly completely scavenged, and HP was completely scavenged, when the retention factor was greater than or equal to 0.25. Bela et al. (2018) found that MHP was very sensitive to ice retention. Unfortunately, there were no MHP observations during this flight to compare to either simulation. Our WRF-Chem MHP SE aligned better with retention factor 0-0.25 than 0.5 though both Bela et al. (2018) and this work reported WRF-Chem MHP SE with standard deviations larger than the average.

The CH_2O and HP WRF-Chem convective complex SEs were higher than Bela et al. (2018) reported for the 0 ice retention factor simulation. However, CH_2O and HP were not completely scavenged like Bela et al. (2018) found for any ice retention factor greater than 0. The DC8 inflow HP SE was the same as the simulation with cloud chemistry and within the standard deviation of the simulation without cloud chemistry. The HP GV spiral SE was 90$\pm$1.4% and greater than WRF-Chem even when accounting for the standard deviation. The GV spiral inflow HP mixing ratio was double the DC8 inflow (Table S2.2). One potential reason for the different HP SE with the DC8 and GV inflow was a difference in reported measurements for peroxides

on the two aircraft (Barth et al., 2016). Another possibility is there is a difference in chemical composition between the two regions. Both observed CH_2O SEs were higher than WRF-Chem. The WRF-Chem CH_2O SE reflects the range that Fried et al. (2016) expected for the DC3 storms. As mentioned above, the airmass storm had the highest CH_2O SE of any of the DC3 test cases by ~30% (Fried et al., 2016). Since this difference is for both observed SE it is potentially the result of *in situ* chemistry and not just the disconnect between inflow and outflow.

The simulated SO_2 SE was substantially lower than observations (92$\pm$3.6%). The WRF-Chem SO_2 SE was higher than Bela et al. (2018) simulations and with a smaller standard deviation. The 0.25 retention factor simulation (41$\pm$92%) was closest to our WRF-Chem simulations. The SO_2 SE was higher when using cloud chemistry but given the large standard deviations there was no appreciable difference between the simulation with cloud chemistry (46$\pm$22%) or without (31$\pm$23%). Future work should compare different ice retention factors with the larger SE sampling range of this study to quantify the impact of ice retention on the larger scale. It is possible this chemical criteria SE method based on HNO_3 scavenging accounted for part of the impact of ice retention because the WRF-Chem SE was bounded by observational HNO_3 SE.

The HFo GV spiral SE was negative (-22 $\pm$ 17%). A negative SE means there was more HFo in the outflow than the inflow suggesting *in situ* aqueous production. The difference between the inflow and outflow was small, 30 ppt, with the outflow higher than inflow. The HFo SENEX SE was around 80% and within the one standard deviation for both WRF-Chem simulations. The drastic difference between the

observe HFo SE is due in part to the difference in sampling conditions. SENEX's goal was to quantify the impact of natural and anthropogenic emissions on tropospheric O_3 and aerosol formation; therefore, sampling on warm, dry days was preferable. The GV spiral was at the end of the flight, after several hours of convective activity in the region that would have washed out some HFo. The SENEX and GV spiral provide potential upper and lower bounds to HFo inflow. The WRF-Chem HFo SE was in between SENEX and GV.

The almost identical HFo in the storm inflow and outflow using the GV inflow suggests that there is some *in situ* production countering the scavenging. WRF-Chem was unable to replicate the observed CH_2O SE. The similarity between the DC8 and GV CH_2O SE implies it is not a difference of mismatch between inflow and outflow but of storm dynamics or chemistry. The similarity of butane and pentane ratios (Table 2.5) for the GV data support that this was not a mismatch between the inflow and outflow. It is possible that the higher than expected CH_2O SE was because of *in situ* production of HFo and therefore loss of CH_2O.

The AAES GV spiral SE is lower than HAc and GA WRF-Chem SE. As discussed in Treadaway et al. (2018) the PCIMS sensitivity to HAc relative to GA is somewhere between 1:1 and 1:10. The HAc and GA WRF-Chem SE are almost identical and was unexpected given the GA Henry's Law constant is an order of magnitude higher. Though the SEs are similar the outflow average is almost two times higher for HAc than GA. The similar SE is surprising based on the Henry's Law constants for the two but some of the difference might be lost due to the substantial standard deviations.

4.6 Isolated Convection Scavenging Efficiency

The SE for a second simulated storm along the Alabama/Tennessee border was determined to investigate how different storm sizes and dynamics could influence organic acid SE (Figure 2.8). The WRF-Chem SE for this storm was determined from 21:00 – 21:20 UTC while the storm was still an isolated convective cell. The WRF-Chem SE was determined using the box in Figure S2.3. The wind is confirmed to be moving from SW-NE at high altitude so the box is "sampling" outflow. The q_{ice} and q_{cloud}, stratospheric air removal, HNO_3>60%, and $NH_3 \geq 10\%$ criteria were applied. The observed HNO_3 SE was ~60%. To confirm that 60% HNO_3 wasn't too strict the criterion was lowered to 40%. This slightly lowered the WRF-Chem SE averages and the standard deviation magnitudes increased.

This simulated storm is assumed to be similar to the isolated convection to the northeast of the convective complex (B2) where the HFo plume was sampled (Section 3). The HFo plume was encountered on the second pass further out from the storm (20:00 UTC). Observations are replicated using the DC8, SENEX, and GV spiral inflow data from Section 4.5. The DC8 inflow sampling area was near the isolated storm (to the west of the storm) and 20 minutes before the isolated storm outflow period. The outflow measurements are from near isolated convection to the northeast of B2. NEXRAD radar (Figure 2.3) and aircraft flight videos show that there was isolated convection that was decaying by 20:00 UTC near the HFo plume (720 ppt). The outflow measurements are GV data between 19:49 – 19:57 UTC coinciding with flying by the storm outflow as seen on the aircraft video. The outflow data still meet the stratospheric air ($O_3/CO < 1.25$) and $q_{cloud} > 0.01$ g/kg criteria. There is only one

measurement available during this period for the butanes and pentanes. The i/n butane ratio was 0.387 which is closer to the DC8 inflow butane ratio (0.363 $\pm$ 0.0198) though there was only one measurement (Table 2.5). The i/n pentane ratio is lower than either inflow region suggesting a disconnect between the inflow and outflow. There was limited data for organic acids during this time. The HFo outflow mixing ratio (323$\pm$22.5 ppt) was similar to the convective complex. The AAES outflow mixing ratio (341 $\pm$ 64.1 ppt) was lower but within the uncertainty of the convective complex. For both observations and simulations, the only difference in scavenging between the two storms, after accounting for standard deviation, was the observed CH_2O and HNO_3. The CH_2O SE was 7% higher for the isolated storm than convective complex. The HNO_3 SE was 18% lower for the isolated storm relative to the convective complex.

There are large standard deviations for WRF-Chem species for both storms suggesting the storm areas sampled are heterogeneous. The isolated convection calculated SE over 70.6 km^2 and the convective complex over 303 km^2. Despite a difference in storm size and entrainment structure the SE for the WRF-Chem species presented must be considered equivalent when considering the standard deviation. All simulated species had a higher SE when using cloud chemistry except for HNO_3 for the isolated storm. However, the standard deviation for the cloud chemistry HNO_3 SE was 27%. The HNO_3 SE threshold was lowered to 50% for the isolated convection because the observed HNO_3 was lower (57$\pm$9.4%) than the convective complex (75$\pm$7.4%). This did not change the average HNO_3 SE and only increased the standard deviation. In fact, this threshold change did not alter any of the reported SE

dramatically but only increased the standard deviation. Calculating SE over large areas increases the heterogeneity and thus increases the standard deviation but also reflects that SE is not a uniform process.

The higher observed CH_2O SE and lower HNO_3 SE in the isolated convection was not captured by WRF-Chem. This suggests that there are processes differing between the storms that WRF-Chem is unable to represent. One possible explanation for the decrease in HNO_3 SE is a difference in cloud water pH between the two storms. If the observed isolated convection cloud water pH was lower (more acidic) than the convective complex that would lower the HNO_3 solubility resulting in a lower SE. There was a slightly lower SO_2 SE for the isolated convection, another indicator of lower pH, but it was not statistically significant. It is possible that the DC8 SO_2 inflow is not accurately reflecting a similar inflow as the isolated convection would have had. The SO_2 inflow period ranged from 250 – 550 ppt and sampled one of the highest measurements of SO_2 for the flight. If the SO_2 inflow for the isolated convection was lower than what the DC8 sampled this would have lowered the SO_2 SE. There are concrete plants near the inflow region which would increase SO_2. The plants are scattered in the area and if the measured inflow air mass differed from the true inflow for the isolated convection it is possible the SO_2 inflow would be lower if not near a concrete plant source. A lower SO_2 SE has been attributed to a lower pH (Calvert et al., 1985).

If the aqueous HFo was the result of CH_2O production, this would be a net sink for CH_2O. HFo SE was negative for both storms with the GV spiral inflow signifying a higher HFo in the outflow than inflow. HFo Henry's Law constant is higher than

CH_2O for the majority of the storm cloud. Only near the top of the supercooled droplet range (-40^{o}C/233 K) are the two constants equal. Therefore, it would be assumed that HFo SE would be higher than CH_2O. As mentioned above, for the convective complex the inflow and outflow HFo difference was only 21 ppt and only 10 ppt for the isolated convection. Even if treating this as no difference between inflow and outflow this suggests there is no HFo scavenging in either storm which is unrealistic. Both storms have a higher CH_2O SE than expected (Fried et al., 2016). Further, 700 ppt HFo was measured near the isolated convection outflow. It is possible there was *in situ* aqueous production of HFo from CH_2O that was released from evaporated cloud water as HFo.

There is no observational or WRF-Chem pH available. Unfortunately, WRF-Chem v. 3.7 does not keep track of the proportion of soluble chemicals in the aqueous phase between time steps and uses a prescribed pH of 5. There is observational data (NADP, 2019) collected to the east of the storm in Great Smoky National Park (pH of 4.96 collected from 5/22-5/29/2012) and to the west in Hatchie National Wildlife Refuge (pH of 5.27 collected from 5/8/5/15/2012). The Barth box model is used to evaluate the influence of pH on HFo and HAc formation and release in clouds (Section 4.7).

4.7 Box Model

Barth et al. (2016) developed a box model that simulates scavenging through a cloud and allows for tuning parameters in a more computationally cost effective manner than with WRF-Chem. The model uses the WRF-Chem meteorological data to set the vertical profile for the simulated storm conditions (temperature, pressure,

hydrometeor mixing ratios, and vertical velocity). The model also uses the near surface gas phase chemical mixing ratios to set the initial conditions. The model is run twice for each experiment. One run assumes that there is no cloud (no aqueous chemistry or scavenging) and the other includes a cloud (includes scavenging and aqueous chemistry). This model allows for simple changes such as altering the gas phase initial mixing ratios or prescribed hydrometeor mixing ratios. This model does not include any gas phase chemistry for HFo.

The parcel model assumes that when the cloud evaporates at high altitude all the aqueous phase species are released to the gas phase. This results in an outflow spike just above the top of the cloud (q_{cloud} = 0 g/kg). The parcel model partitions the soluble species between the gas and cloud water; therefore, what is released at the cloud top is an upper limit as it assumes there is no scavenging in rain, snow, etc. Results of the experiments were compared for the model point right before the cloud evaporates to compensate for some removal as the parcel model does not account for precipitation scavenging. The parcel model was used to test 1) aqueous HFo sources, 2) the influence of pH on aqueous production, and 3) the WRF-Chem assumption that aqueous chemistry only occurs when the temperature is greater than 258K (-15^{o}C).

A base run was done first to replicate the WRF-Chem conditions. The box model was run for the WRF-Chem middle outflow time period for both the convective complex and isolated convection for model grid points with radar reflectivity greater than 40 dbz. The base run had a constant pH of 5, aqueous chemistry up to 258 K, and only CH_2O as an aqueous HFo source. Figures 2.9 and 2.10 show the hydrometeor, HFo, HAc, and GA mixing ratios for the convective complex and isolated convection.

The black line is only gas phase chemistry with no scavenging. The gray lines indicate the cloud top bottom and top. The cloud top height was lower for the isolated convection compared to the complex as discussed above. This resulted in a lower outflow altitude for the isolated convection. The blue lines in Figures 2.9 and 2.10 b, c, and d are the gas phase mixing ratio in the presence of a cloud and aqueous chemistry. The blue lines will be primarily used to compare the "outflow" results between the experiments.

4.7.1 HFo Aqueous Production

The WRF-Chem aqueous chemistry mechanism used has only one aqueous source for HFo – the CH_2O + HO reaction. However, other aqueous reactions have been suggested including glyoxal and HO, HP and glyoxal, and HP and glyoxylic acid. These are included in Barth's box model (Table S2.1) as well as a second loss reaction of HP and HFo though this reaction is slow. The difference in outflow HFo is compared between just CH_2O production and the additional production and loss sources. Both experiments were performed with the WRF-Chem initial mixing ratios, a pH of 5, and aqueous production to 258 K (-15^{o}C). This would prevent changes in HFo production and loss due to pH.

In the CH_2O only experiment, HFo at the top of the cloud decreased by 50% for the isolated convection and 80% for the convective complex compared to the inflow. The maximum amount of cloud water was similar between the two storms but the convective complex had a higher cloud top height. This allows for more removal of the soluble species to the cloud water, the analogy for scavenging in this model.

With the addition of other HFo aqueous production sources, the gas phase HFo was the same as the CH_2O only experiment before the cloud evaporated. HFo increased ~10 ppt for both convective systems relative to the inflow value when the cloud evaporated. This is a very small increase in the outflow that still cannot account for the observed HFo plume. There was no difference in HAc and GA as a result of these changes. The next step is to test different pH values to see how that impacts HFo, HAc, and GA.

4.7.2 Cloud Water pH

Four pH experiments were performed at 5.5, 4.5, 3.5, and 2.5 to cover the pKa range for HFo (3.75) and HAc (4.75). This also covered the natural precipitation range which can be between 5 – 5.5 and acid rain range which is typically 4.2 – 4.4 (EPA, accessed 3/3/19). The pH experiment used the WRF-Chem near surface mixing ratios and stopped aqueous production at temperatures lower than 258 K (-15^{o}C). This also only used the CH_2O HFo production source.

There was no difference in GA mixing ratios for the different pH values even though the aqueous source was HAc which is pH dependent. HFo acted as expected for the pH experiments with the highest pH having the greatest scavenging impact. At the higher pH the equilibrium shifts towards formate allowing more HFo uptake. HFo was almost completely scavenged in the convective complex at the highest pH (5.5). HFo decreased 80% in the isolated convection for the 5.5 pH experiment. Isolated convection had the biggest HFo increase in the outflow when the pH dropped from 5.5 to 4.5. The HFo outflow gas phase mixing ratio increased almost 100 ppt. The HFo outflow for the convective complex increased ~30 ppt for each drop in pH from 5.5 to

3.5. There was very little difference in HFo for either storm when the pH was lowered from 3.5 to 2.5. Previous model work found the maximum total HFo at a pH of 3.5 (Jacob, 1986). The HFo outflow increased only a few ppt when the pH was lowered to 2.5 relative to the 3.5 pH outflow. The isolated convection HFo outflow was almost back to the inflow value when the pH was 3.5 or lower. The convective complex HFo outflow never reached the inflow value. There was ~a 25% decrease between the inflow and outflow even at a pH of 2.5.

The surprise came with HAc. At the top of the cloud there appeared to be a maximum HAc at a pH greater than the pKa. The 5.5 simulation had the greatest gas phase mixing ratio in the outflow. There is HAc gas phase production, unlike HFo, though it doesn't produce a drastic enough difference in mixing ratio to cause this. The primary HAc aqueous source is pyruvic acid. The other aqueous reaction is acetaldehyde with HO. A pH of 5.5 had the maximum total (gas + aqueous) pyruvic acid of all the pH runs for both storms. The gas phase mixing ratio of pyruvic acid is small (4 orders of magnitude lower than total). The majority is in the aqueous phase and the maximum pyruvic acid is at 5.5 therefore the HAc maximum is a function of pyruvic acid formation. In the model aqueous pyruvic acid is formed by reaction of ozone and MVK.

4.7.3 Aqueous Chemistry Temperature Minimum

WRF-Chem assumes that all aqueous chemistry occurs while the temperature is greater than 258 K (-15^{o}C) but this may be an underestimation. HFo, HAc, and GA production is compared at a constant pH (5.0) for three different temperature ranges: 258 K (-15^{o}C), 248 K (-20^{o}C) and 233 K (-40^{o}C). This experiment also used the WRF-

Chem gas phase near surface values and only the CH_2O source of HFo. The temperature profile was the same for the two storms. The 258 K simulation stopped aqueous chemistry at 6200 m. The 248 K simulation stopped aqueous chemistry at 7600 m. The 233 K simulation stopped aqueous chemistry at 9400 m. The 233 K simulation was chosen as the upper limit of aqueous chemistry. This is the lowest temperature usually considered for supercooled droplets to exist. As there was no cloud water above 7000 m for the isolated convection, and therefore no aqueous production, this comparison will only be for the convective complex.

There was no difference in GA for the three temperature experiments. GA has one aqueous loss and formation reaction in the box model and the reaction rate between the aqueous formation ($k = 1.2x10^9$ M s^{-1}) and loss are similar though the loss is temperature dependent ($A = 1.2x10^9$ M s^{-1}, $E/R = -1.3x10^3$ K). Consequently, it is expected that there would be little change in concentration as a function of temperature. The gas phase mixing ratio decreased in the cloud for all three simulations but the total concentration remained the nearly constant throughout the storm. This indicates that for GA the box model both gas and aqueous phase chemistry played a very small role compared to scavenging.

There was also no difference in HFo between the temperature simulations. Again, there is only one aqueous production and loss source. The CH_2O reaction rate constant is about an order of magnitude higher than the HFo loss rate constant in cloud temperature range so there should have been net production. Both rate constants decrease with temperature and the rate constant at 233 K is about half the 258 K rate constant. The 233 K experiment allows for aqueous chemistry for 3200 m more than

the 258 K experiment. This does not compensate for the decreasing reaction rate enough to cause a notable gas phase mixing ratio increase at the cloud top because the cloud water mixing ratio is so small.

In comparison to HFo and GA, HAc has multiple aqueous formation reactions and one loss. The HAc cloud top mixing ratio was higher than the cloud bottom for all box model simulations indicating the HAc aqueous reactions rates were faster than HFo or GA leading to more production. There was a 12% increase in HAc at the cloud top relative to the cloud base for convective complex 233 K simulation. This was the largest increase in the HAc outflow. The cloud top HAc increased 8% for the 248 K simulation and 4% for the 233 K simulation. There was only a 16 ppt difference between the 258 K and 248 K simulations even though this corresponds with a 1400 m altitude difference. Gas phase production was small enough to not impact this temperature difference (less than 4 ppt). The 258 K WRF-Chem temperature constraint is likely an overly conservative estimate for the aqueous chemistry range within a storm. However, if there isn't substantial liquid water content to produce a desired species in the aqueous phase increasing the temperature range is irrelevant.

4.7.4 Best Combined Scenario

In the experiments described above, only one factor was altered at a time to see what the influence was on HFo, HAc, and GA cloud top mixing ratios. None of the above experiments found a similar relative outflow HFo mixing ratio to explain the HFo plume of 700 ppt. The HFo peak observed during RF03 is likely not the product of one difference but a combination of situations that would increase HFo. The final experiment used multiple HFo aqueous reactions at a constant pH of 3.5 with aqueous

chemistry up to 233 K. In essence this assumes aqueous production for the whole cloud for both storms.

Figure 2.11 and 2.12 show the box model results for the convective complex and isolated convection respectively. Neither storm was able to reproduce the same large increase though the isolated convection did have HFo production higher than the surface mixing ratio. It is important to remember that there are no HFo gas phase reactions in the box model and this model is used to look at HFo aqueous production. The convective complex had a similar mixing ratio at the cloud base and cloud top (Figure 2.11) when accounting for the 100% degassing at the cloud top. Otherwise, there was still an overall decrease in HFo. However, there was a 9% increase in HFo at the cloud top for the isolated convection. There was a 15% increase when the cloud evaporated.

While it is not the same large increase as observed, the modified box model produced higher HFo at the cloud top than cloud bottom for the isolated convection. This was not possible for the convective complex. The cloud top HAc was ~40 ppt higher than the cloud bottom for both storms. In other words, there was no appreciable difference in HAc in the "outflow" between the storms but there was for HFo which is similar to observations even if the magnitude could not be replicated. Another possibility not considered here was the updraft region had a significantly higher HFo mixing ratio than sampled during the GV spiral. The observed HFo plume is likely a combination of higher HFo inflow than accounted for here as well as *in situ* aqueous production and subsequent release to the gas phase when the cloud evaporated.

5 Summary

The primary goal of this study was to understand how convective storms affect organic acids and what potential there is for either organic acid (HFo and HAc) to be transported to the UT. The photochemical lifetime of HFo and HAc increases to 20+ days in the UT; therefore, if they are transported they could influence chemistry far from the original source. Conventionally, because both organic acids are fairly soluble, they are treated as scavenged in a storm and thus not present in the convective outflow. Observational evidence from DC3 found elevated HFo (700 ppt) at 8 km near isolated convection. In comparison, there was ~300 ppt HFo sampled in the outflow of a nearby convective complex. There was not sufficient observational data to explore the cause for this HFo peak and the influence that different storm structures have on scavenging.

A regional chemical model (WRF-Chem) and box model provided insight to how organic acids are altered in convective storms by comparing a convective complex and isolated convection. There was no difference in scavenging efficiency after accounting for the standard deviation for either organic acid between the two storms with or without aqueous chemistry. The impact of pH, adding HFo aqueous production sources, and aqueous chemistry temperature range were all tested with a box model. Cloud top HFo for the isolated convection was higher than the cloud bottom with a pH of 3.5, multiple aqueous chemistry sources, and allowing aqueous chemistry to occur for the whole cloud. The convective complex still had an overall decrease in HFo. HAc at the cloud top was greater than the cloud base for all experiments with the majority of formation from pyruvic acid. There was little difference in the cloud top HAc between the two storms reflecting observations which

had similar HAc outflow mixing ratio for both storms. GA was not altered significantly in the box model experiments and was lower than HAc in both models.

References

Amelynck, C., Schoon, N., & Arijs, E. (2000). Gas phase reactions of CF3O-and CF3O-H2O with nitric, formic, and acetic acid. *International Journal of Mass Spectrometry*, *203*(1–3), 165–175. https://doi.org/10.1016/S1387-3806(00)00321-3

Apel, E. C., Hornbrook, R. S., Hills, A. J., Blake, N. J., Barth, M. C., Weinheimer, A., et al. (2015). Upper tropospheric ozone production from lightning NO_x-impacted convection: Smoke ingestion case study from the DC3 campaign. *Journal of Geophysical Research: Atmospheres*, *120*(6), 2505–2523. https://doi.org/10.1002/2014JD022121

Barth, M. C., Sillman, S., Hudman, R., Jacobson, M.Z., Kim, C.H., Monod, A., Liang, J. (2003). Summary of the cloud chemistry modeling intercomparison: Photochemical box model simulation. *Journal of Geophysical Research*, *108*(D7), 4214. https://doi.org/10.1029/2002JD002673

Barth, M. C., Cantrell, C. A., Brune, W. H., Rutledge, S. A., Crawford, J. H., Huntrieser, H., et al. (2015). The Deep Convective Clouds and Chemistry (DC3) Field Campaign. *Bulletin of the American Meteorological Society*. https://doi.org/10.1175/BAMS-D-13-00290.1

Barth, M. C., Apel, E. C., Hornbrook, R. S., Hills, A. J., Blake, N JWeinheimer, A., Cantrell, C., et al. (2016). Journal of Geophysical Research : Atmospheres. *Journal of Geophysical Research: Atmospheres*, *121*, 4272–4295. https://doi.org/10.1002/2014JD022121.Received

Bela, M. M., Barth, M. C., Toon, O. B., Fried, A., Homeyer, C. R., Morrison, H., et al. (2016). Wet scavenging of soluble gases in DC3 deep convective storms using WRF-Chem simulations and aircraft observations. *Journal of Geophysical Research: Atmospheres*, *121*(8), 4233–4257. https://doi.org/10.1002/2015JD024623

Bela, M. M., Barth, M. C., Toon, O. B., Fried, A., Ziegler, C., Cummings, K. A., et al. (2018). Effects of Scavenging, Entrainment, and Aqueous Chemistry on Peroxides and Formaldehyde in Deep Convective Outflow Over the Central and Southeast United States. *Journal of Geophysical Research: Atmospheres*, *123*(14), 7594–7614. https://doi.org/10.1029/2018JD028271

Betterton, E. A., & Hoffmann, M. R. (1988). Henry's law constants of some environmentally important aldehydes. *Environmental Science and Technology*,

22(1), 1415–1418. https://doi.org/10.1021/es00177a004

Blake, N. J., Blake, D. R., Simpson, I. J., Meinardi, S., Swanson, A. L., Lopez, J. P., et al. (2003). NMHCs and halocarbons in Asian continental outflow during the Transport and Chemical Evolution over the Pacific (TRACE-P) Field Campaign: Comparison With PEM-West B. *Journal of Geophysical Research*, *108*(D20), 8806. https://doi.org/10.1029/2002JD003367

Calvert, J. G., Lazrus, A., Kok, G. L., Heikes, B. G., Walega, J. G., Lind, J., & Cantrell, C. A. (1985). Chemical mechanisms of acid generation in the troposphere. *Nature*, *317*, 27–35. https://doi.org/10.1038/317027a0

Carlton, A. G., Turpin, B. J., Lim, H. J., Altieri, K. E., & Seitzinger, S. (2006). Link between isoprene and secondary organic aerosol (SOA): Pyruvic acid oxidation yields low volatility organic acids in clouds. *Geophysical Research Letters*, *33*(6), 2–5. https://doi.org/10.1029/2005GL025374

Charlson, R. J., & Rodhe, H. (1982). Factors controlling the acidity of natural rainwater. *Nature*, *295*, 683–685. https://doi.org/10.1038/295683a0

St. Clair, J. M., McCabe, D. C., Crounse, J. D., Steiner, U., & Wennberg, P. O. (2010). Chemical ionization tandem mass spectrometer for the in situ measurement of methyl hydrogen peroxide. *Review of Scientific Instruments*, *81*(9), 094102. https://doi.org/10.1063/1.3480552

Crounse, J., McKinney, K., Kwan, A., & Wennberg, P. . (2006). Measurement of gas-phase hydroperoxides by chemical ionization mass spectrometry. *Analytical Chemistry*, *78*(19), 6726–6732. Retrieved from http://pubs.acs.org/doi/abs/10.1021/ac0604235

Crounse, J. D., McKinney, K. A., Kwan, A. J., & Wennberg, P. O. (2006). Measurement of Gas-Phase Hydroperoxides by Chemical Ionization Mass Spectrometry. *Analytical Chemistry*, *78*(19), 6726–6732. https://doi.org/10.1021/ac0604235

Diskin, G. S., Podolske, J. R., Sachse, G. W., & Slate, T. A. (2002). Open-path airborne tunable diode laser hygrometer. In A. Fried (Ed.) (p. 196). https://doi.org/10.1117/12.453736

Emmons, L. K., Walters, S., Hess, P. G., Lamarque, J. F., Pfister, G. G., Fillmore, D.,

et al. (2010). Description and evaluation of the Model for Ozone and Related chemical Tracers, version 4 (MOZART-4). *Geoscientific Model Development*, *3*(1), 43–67. https://doi.org/10.5194/gmd-3-43-2010

EPA. (n.d.). Acid Rain. Retrieved March 3, 2019, from https://www.epa.gov/acidrain/what-acid-rain

Fahey, K. M., & Pandis, S. N. (2001). Optimizing model performance : variable size resolution in cloud chemistry modeling. *Atmospheric Environment*, *35*, 4471–4478. https://doi.org/10.1016/S1352-2310(01)00224-2

Fierro, A. O., Mansell, E. R., Ziegler, C. L., & MacGorman, D. R. (2012). Application of a Lightning Data Assimilation Technique in the WRF-ARW Model at Cloud-Resolving Scales for the Tornado Outbreak of 24 May 2011. *Monthly Weather Review*, *140*(8), 2609–2627. https://doi.org/10.1175/MWR-D-11-00299.1

Fried, A., Barth, M. C., Bela, M., Weibring, P., Richter, D., Walega, J., et al. (2016). Convective transport of formaldehyde to the upper troposphere and lower stratosphere and associated scavenging in thunderstorms over the central United States during the 2012DC3 study. *Journal of Geophysical Research*, *121*(12), 7430–7460. https://doi.org/10.1002/2015JD024477

Galloway, J. N., Likens, G. E., Keene, W. C., & Miller, J. M. (1982). The composition of precipitation in remote areas of the world. *Journal of Geophysical Research*, *87*(C11), 8771–8786. https://doi.org/10.1029/JC087iC11p08771

Gerbig, C., Schmitgen, S., Kley, D., Volz-Thomas, A., Dewey, K., & Haaks, D. (1999). An improved fast-response vacuum-UV resonance fluorescence CO instrument. *Journal of Geophysical Research: Atmospheres*, *104*(D1), 1699–1704. https://doi.org/10.1029/1998JD100031

Grell, G. A. (1993). Prognostic Evaluation of Assumptions Used by Cumulus Parameterizations. *Monthly Weather Review*. https://doi.org/10.1175/1520-0493(1993)121<0764:PEOAUB>2.0.CO;2

Grell, G. A., & Dévényi, D. (2002). A generalized approach to parameterizing convection combining ensemble and data assimilation techniques. *Geophysical Research Letters*, *29*(14), 38-1-38–4. https://doi.org/10.1029/2002GL015311

Guenther, A., Karl, T., Harley, P., Wiedinmyer, C., Palmer, P. I., & Geron, C. (2006).

Estimates of global terrestrial isoprene emissions using MEGAN (Model of Emissions of Gases and Aerosols from Nature). *Atmospheric Chemistry and Physics*, *6*, 3181–3210. https://doi.org/10.5194/acp-6-3181-2006

Huey, L. G. (2007). Measurement of Trace Atmospheric Species by Chemical Ionization Mass Spectrometry: Speciation of Reactive Nitrogen and Future Directions. *Mass Spectrometry Reviews*, *26*, 166–184. https://doi.org/10.1002/mas

Huey, L. G., Villalta, P. W., Dunlea, E. J., Hanson, D. R., & Howard, C. J. (1996). Reactions of CF 3 O - with Atmospheric Trace Gases. *The Journal of Physical Chemistry*, *100*(1), 190–194. https://doi.org/10.1021/jp951928u

Jacob, D. J. (1986). Chemistry of OH in remote clouds and its role in the production of formic acid and peroxymonosulfate. *Journal of Geophysical Research*, *91*(D9), 9807–9826. https://doi.org/10.1029/JD091iD09p09807

Jacob, D. J., & Wofsy, S. (1988). Photochemistry of biogenic emissions over the Amazon forest. *Journal of Geophysical Research Atmospheres*, *93*(D2), 1477–1486. https://doi.org/10.1029/JD093iD02p01477

Keene, W. C., & Galloway, J. N. (1984). Organic acidity in precipitation of North America. *Atmospheric Environment*, *18*(11), 2491–2497. https://doi.org/10.1016/0004-6981(84)90020-9

Keene, W. C., Galloway, J. N., & Holden, J. D. (1983). Measurements of Weak Organic Acidity in Precipitation From Remote Areas of the World. *J. Geophys. Res.*, *88*(C9), 5122–5130.

Keene, W. C., Mosher, B. W., Jacob, D. J., Munger, J. W., Talbot, R. W., Artz, R. S., et al. (1995). Carboxylic acids in clouds at a high-elevation forested site in central Virginia. *Journal of Geophysical Research*, *100*(D5), 9345. https://doi.org/10.1029/94JD01247

Khare, P., Kumar, N., Kumari, K., & Srivastava, S. (1999). Atmospheric formic and acetic acids: An overview. *Reviews of Geophysics*, *32*(2), 227–248. Retrieved from http://www.agu.org/pubs/crossref/1999/1998RG900005.shtml

Kim, S., Huey, L. G., Stickel, R. E., Tanner, D. J., Crawford, J. H., Olson, J. R., et al. (2007). Measurement of HO 2 NO 2 in the free troposphere during the

Intercontinental Chemical Transport Experiment–North America 2004. *Journal of Geophysical Research*, *112*(D12), D12S01. https://doi.org/10.1029/2006JD007676

Korolev, A. V., Emery, E. F., Strapp, J. W., Cober, S. G., Isaac, G. A., Wasey, M., & Marcotte, D. (2011). Small Ice Particles in Tropospheric Clouds: Fact or Artifact? Airborne Icing Instrumentation Evaluation Experiment. *Bulletin of the American Meteorological Society*, *92*(8), 967–973. https://doi.org/10.1175/2010BAMS3141.1

Kua, J., Galloway, M. M., Millage, K. D., Avila, J. E., & De Haan, D. O. (2013). Glycolaldehyde monomer and oligomer equilibria in aqueous solution: Comparing computational chemistry and NMR data. *Journal of Physical Chemistry A*, *117*(14), 2997–3008. https://doi.org/10.1021/jp312202j

Laj, P., Fuzzi, S., Facchini, M. C., Lind, J. A., Orsi, G., Preiss, M., et al. (1997). Cloud processing of soluble gases. *Atmospheric Environment*, *31*(16), 2589–2598. https://doi.org/10.1016/S1352-2310(97)00040-X

Lance, S., Brock, C. A., Rogers, D., & Gordon, J. A. (2010). Water droplet calibration of the Cloud Droplet Probe (CDP) and in-flight performance in liquid, ice and mixed-phase clouds during ARCPAC. *Atmospheric Measurement Techniques*, *3*(6), 1683–1706. https://doi.org/10.5194/amt-3-1683-2010

Lee, B. H., Lopez-Hilfiker, F. D., Mohr, C., Kurtén, T., Worsnop, D. R., & Thornton, J. a. (2014). An iodide-adduct high-resolution time-of-flight chemical-ionization mass spectrometer: Application to atmospheric inorganic and organic compounds. *Environmental Science and Technology*, *48*(11), 6309–6317. https://doi.org/10.1021/es500362a

Lee, Y.-N., Zhou, X., & Hallock, K. (1995). Atmospheric carbonyl compounds at a rural southeastern United States site. *Journal of Geophysical Research*, *100*(D12), 25933. https://doi.org/10.1029/95JD02605

Lee, Y. N., Zhou, X., Kleinman, L. I., Nunnermacker, L. J., Springston, S. R., Daum, P. H., et al. (1998). Atmospheric chemistry and distribution of formaldehyde and several multioxygenated carbonyl compounds during the 1995 Nashville/Middle Tennessee Ozone Study. *J. Geophys. Res.*, *103*(D17), 22449. https://doi.org/10.1029/98JD01251

Li, Y., Pickering, K. E., Allen, D. J., Barth, M. C., Bela, M. M., Cummings, K. A., et

al. (2017). Evaluation of deep convective transport in storms from different convective regimes during the DC3 field campaign using WRF-Chem with lightning data assimilation. *Journal of Geophysical Research: Atmospheres*, *122*(13), 7140–7163. https://doi.org/10.1002/2017JD026461

Magneron, I., Mellouki, A., Le Bras, G., Moortgat, G. K., Horowitz, A., & Wirtz, K. (2005). Photolysis and OH-Initiated oxidation of glycolaldehyde under atmospheric conditions. *Journal of Physical Chemistry A*, *109*(20), 4552–4561. https://doi.org/10.1021/jp044346y

Mecikalski, R. M., Bain, A. L., & Carey, L. D. (2015). Radar and Lightning Observations of Deep Moist Convection across Northern Alabama during DC3: 21 May 2012. *Monthly Weather Review*, *143*(7), 2774–2794. https://doi.org/10.1175/MWR-D-14-00250.1

Millet, D. B., Baasandorj, M., Farmer, D. K., Thornton, J. A., Baumann, K., Brophy, P., et al. (2015). A large and ubiquitous source of atmospheric formic acid. *Atmospheric Chemistry and Physics*, *15*(11), 6283–6304. https://doi.org/10.5194/acp-15-6283-2015

National Atmospheric Deposition Program (NRSP-3). (2019). NADP Program Office, Wisconsin State Laboratory of Hygiene, 465 Henry Mall, Madison, WI 53706.

Neu, J. L., & Prather, M. J. (2012). Toward a more physical representation of precipitation scavenging in global chemistry models : cloud overlap and ice physics and their impact on tropospheric ozone. *Atmospheric Chemistry and Physics*, *12*, 3289–3310. https://doi.org/10.5194/acp-12-3289-2012

Neuman, J. A., Huey, L. G., Dissly, R. W., Fehsenfeld, F. C., Flocke, F., Holecek, J. C., et al. (2002). Fast-response airborne in situ measurements of HNO 3 during the Texas 2000 Air Quality Study. *Journal of Geophysical Research*, *107*(D20). https://doi.org/10.1029/2001JD001437

Neuman, J. A., Nowak, J. B., Huey, L. G., Burkholder, J. B., Dibb, J. E., Holloway, J. S., et al. (2010). Bromine measurements in ozone depleted air over the Arctic Ocean. *Atmospheric Chemistry and Physics*, *10*, 6503–6514. https://doi.org/10.5194/acp-10-6503-2010

O'Sullivan, D. W., Silwal, I. K. C., McNeill, A. S., Treadaway, V., & Heikes, B. G. (2018). Quantification of gas phase hydrogen peroxide and methyl peroxide in ambient air: Using atmospheric pressure chemical ionization mass spectrometry

with O2−, and O2−(CO2) reagent ions. *International Journal of Mass Spectrometry*, *424*, 16–26. https://doi.org/10.1016/j.ijms.2017.11.015

Paulot, F., Wunch, D., Crounse, J. D., Toon, G. C., Millet, D. B., DeCarlo, P. F., et al. (2011). Importance of secondary sources in the atmospheric budgets of formic and acetic acids. *Atmospheric Chemistry and Physics*, *11*(5), 1989–2013. https://doi.org/10.5194/acp-11-1989-2011

Petitjean, M., Reyès-Pérez, E., Pérez, D., Mirabel, P., & Le Calvé, S. (2010). Vapor pressure measurements of hydroxyacetaldehyde and hydroxyacetone in the temperature range (273 to 356) K. *Journal of Chemical and Engineering Data*, *55*(2), 852–855. https://doi.org/10.1021/je9004905

Richter, D., Weibring, P., Walega, J. G., Fried, A., Spuler, S. M., & Taubman, M. S. (2015). Compact highly sensitive multi-species airborne mid-IR spectrometer. *Applied Physics B*, *119*(1), 119–131. https://doi.org/10.1007/s00340-015-6038-8

Ridley, B. A., & Grahek, F. E. (1990). A Small, Low Flow, High Sensitivity Reaction Vessel for NO Chemiluminescence Detectors. *Journal of Atmospheric and Oceanic Technology*, *7*(2), 307–311. https://doi.org/10.1175/1520-0426(1990)007<0307:ASLFHS>2.0.CO;2

Ridley, B. A., Grahek, F. E., & Walega, J. G. (1992). A Small High-Sensitivity, Medium-Response Ozone Detector Suitable for Measurements from Light Aircraft. *Journal of Atmospheric and Oceanic Technology*, *9*(2), 142–148. https://doi.org/10.1175/1520-0426(1992)009<0142:ASHSMR>2.0.CO;2

Ryerson, T. B., Williams, E. J., & Fehsenfeld, F. C. (2000). An efficient photolysis system for fast-response NO 2 measurements. *Journal of Geophysical Research: Atmospheres*, *105*(D21), 26447–26461. https://doi.org/10.1029/2000JD900389

Sachse, G. W., Hill, G. F., Wade, L. O., & Perry, M. G. (1987). Fast-response, high-precision carbon monoxide sensor using a tunable diode laser absorption technique. *Journal of Geophysical Research*, *92*(D2), 2071. https://doi.org/10.1029/JD092iD02p02071

Sander, R. (2015). Compilation of Henry's law constants (version 4.0) for water as solvent. *Atmospheric Chemistry and Physics*, *15*(8), 4399–4981. https://doi.org/10.5194/acp-15-4399-2015

Talbot, R. W., Andreae, M. O., Berresheim, H., Jacob, D. J., & Beecher, K. M. (1990). Sources and sinks of formic, acetic, and pyruvic acids over central Amazonia: 2. Wet season. *Journal of Geophysical Research*, *95*(D10), 16799. https://doi.org/10.1029/JD095iD10p16799

Talbot, R. W., Mosher, B. W., Heikes, B. G., Jacob, D. J., Munger, J. W., Daube, B. C., et al. (1995). Carboxylic-Acids in the Rural Continental Atmosphere over the Eastern United-States During the Shenandoah Cloud and Photochemistry Experiment. *Journal of Geophysical Research-Atmospheres*, *100*(D5), 9335–9343.

Treadaway, V., Heikes, B. G., McNeill, A. S., Silwal, I. K. C., & O'Sullivan, D. W. (2018). Measurement of formic acid, acetic acid and hydroxyacetaldehyde, hydrogen peroxide, and methyl peroxide in air by chemical ionization mass spectrometry: Airborne method development. *Atmospheric Measurement Techniques*, *11*(4), 1901–1920. https://doi.org/10.5194/amt-11-1901-2018

Weibring, P., Richter, D., Fried, A., Walega, J. G., & Dyroff, C. (2006). Ultra-high-precision mid-IR spectrometer II: system description and spectroscopic performance. *Applied Physics B*, *85*(2–3), 207–218. https://doi.org/10.1007/s00340-006-2300-4

Weibring, P., Richter, D., Walega, J. G., & Fried, A. (2007). First demonstration of a high performance difference frequency spectrometer on airborne platforms. *Optics Express*, *15*(21), 13476. https://doi.org/10.1364/OE.15.013476

Wiedinmyer, C., Akagi, S. K., Yokelson, R. J., Emmons, L. K., Orlando, J. J., & Soja, A. J. (2011). Model Development The Fire INventory from NCAR (FINN): a high resolution global model to estimate the emissions from open burning. *Geoscientific Model Development*, *4*, 625–641. https://doi.org/10.5194/gmd-4-625-2011

Yuan, B., Veres, P. R., Warneke, C., Roberts, J. M., Gilman, J. B., Koss, et al. (2015). Investigation of secondary formation of formic acid: urban environment vs. oil and gas producing region. *Atmospheric Chemistry and Physics*, *15*(4), 1975–1993. https://doi.org/10.5194/acp-15-1975-2015

Zondlo, M. A., Paige, M. E., Massick, S. M., & Silver, J. A. (2010). Vertical cavity laser hygrometer for the National Science Foundation Gulfstream-V aircraft. *Journal of Geophysical Research*, *115*(D20), D20309. https://doi.org/10.1029/2010JD014445

Table 2.1: DC8 instrumentation used as observation data in this study

Species	Instrument	LLOD	Uncertainty	Citation
H_2O vapor	DLH		5% or 1 ppmv	Diskin et al. (2002)
Cloud Indicator		N/A	N/A	N/A
IWC	2D-S IWC	N/A	N/A	N/A
O_3	ESRL		0.040 ppbv + 3%	Ryerson et al. (2000)
CO	DACOM		2 ppb or 2%	Sachse et al. (1987)
H_2O_2	CIT-CIMS		+-(50% of measurement value + 75 pptv)	Amelynck et al. (2000); St. Clair et al. (2010); Crounse et al. (2006); Huey et al. (1996)
CH_3OOH	CIT-CIMS		+-[30pptv + following function of DLH water: DLH=0-230ppmv: 40% of MHP; DLH>230pptv: (-9.1+ 20.8*log10(DLH))%]	Amelynck et al. (2000); St. Clair et al. (2010); Crounse et al. (2006); Huey et al. (1996)
CH_2O	DFGAS	51 ppt	2% or 2 ppbv	Weibring et al. (2006; 2007)
SO_2	GT-CIMS	2 pptv	15%	Kim et al. (2007)
HNO_3	CIT-CIMS		+-(50% of measurement value + 100 pptv)	Amelynck et al. (2000); St. Clair et al. (2010); Crounse et al. (2006); Huey et al. (1996)
n-butane	WAS	3 ppt		Blake et al. (2003)

Table 2.2: Gulfstream V instrumentation used as observation data in this study

Species	Instrument	LLOD	Uncertainty	Citation
H_2O vapor	VCSEL		5%	Zondlo et al. (2010)
Ice Water Content	2DC			Korolev et al. (2011)
Liquid Water Content	CDP			Lance et al. (2010)
O_3	chemiluminescence		5%	Ridley et al. (1992); Ridley & Grahek (1990)
CO	UV fluorescence		3 ppb $\pm$ 3%	Gerbig et al. (1999)
H_2O_2	PCIMS		30%	O'Sullivan et al. (2018)
CH_3OOH	PCIMS		50%	O'Sullivan et al. (2018)
HCOOH	PCIMS		30%	Treadaway et al. (2018)
CH_3COOH	PCIMS		30%	Treadaway et al. (2018)
CH_2O	CAMS	20-30 ppt		Richter et al. (2015)
SO_2	GT-CIMS	13.8ppt	15%	Kim et al. (2007)
HNO_3	GT-CIMS	48.4ppt	20%	Huey (2007)
n-butane	TOGA	1 ppt	15%	Apel et al. (2015)

Table 2.3: The Weather Research and Forecasting (WRF) coupled to chemistry model set-up for three domains. Acronyms are explained in the text.

Horizontal grid resolution (km)	15	3	0.6
Model top height (hPa)	70	70	70
Domain Size (dx x dy x dz)	415x325x40	361x301x40	481x481x40
Time step (s)	75	15	3
Model Run Time (UTC)	00 – 22	12 – 22	15 – 22
Initial/Boundary Conditions	3 hr resolution GFS analysis	3 hr resolution GFS analysis	3 hr resolution GFS analysis
Cloud Microphysics	Morrison	Morrison	Morrison
Convection Parameterization	Grell 3D	Explicit	Explicit
Planetary Boundary Layer	YSU	YSU	YSU
Land Surface	Noah	Noah	Noah
Shortwave & longwave radiation	RRTMG	RRTMG	RRTMG
Photolysis	Madronich F-TUV	Madronich F-TUV	Madronich F-TUV
Gas Chemistry	MOZART	MOZART	MOZART
Aerosol Scheme	MOSAIC	MOSAIC	MOSAIC
Wet Deposition	Neu and Prather	Neu and Prather	Neu and Prather
Lightning Options	Neutral Buoyancy (PR92)	max_w (PR92)	max_w (PR92)
Intracloud/cloud-to-ground	Boccippio	Boccippio	Boccippio
Lightning NOx	DeCaria et al.	DeCaria et al.	DeCaria et al
Emissions & Inputs			
Chemistry Boundary and Initial Conditions	MOZART-4	MOZART-4	MOZART-4
Anthropogenic	EPA NEI 2011	EPA NEI 2011	EPA NEI 2011
Biogenic	Megan v2	Megan v2	Megan v2
Biomass Burning	FINN	FINN	FINN
Lightning Data Assimilation	Not Used	ARMOR, 18-22 UTC, 261-291 K	ARMOR, 18-22 UTC, 261-291 K

Table 2.4: HAc and GA ratios based on literature data from the southeastern United States convolved with the 1:1 and 1:10 HAc:GA PCIMS sensitivity.

	1:1 Literature Ratio		14:1 Literature Ratio	
PCIMS Sensitivity	HAc (ppb)	GA (ppb)	HAc (ppb)	GA (ppb)
1:1	0.24	0.24	0.42	0.030
1:10	0.41	0.041	0.43	0.019

Table 2.5: Aircraft i/n-butane and pentane ratios for the convective complex and isolated convection

		Convective Complex		Isolated Convection	
Type	Aircraft	i-butane/ n-butane	i-pentane/ n-pentane	i-butane/ n-butane	i-pentane/ n-pentane
Inflow	DC8	0.363 $\pm$ 0.0198	2.23 $\pm$ 0.0389	0.363 $\pm$ 0.0198	2.23 $\pm$ 0.0389
Inflow	GV	0.415 $\pm$ 0.0132	1.31 $\pm$ 0.0887	0.415 $\pm$ 0.0132	1.31 $\pm$ 0.0887
Outflow	GV	0.423 $\pm$ 0.0014	1.23 $\pm$ 0.0815	0.3865*	0.9902*

*There was only one measurement during the outflow period

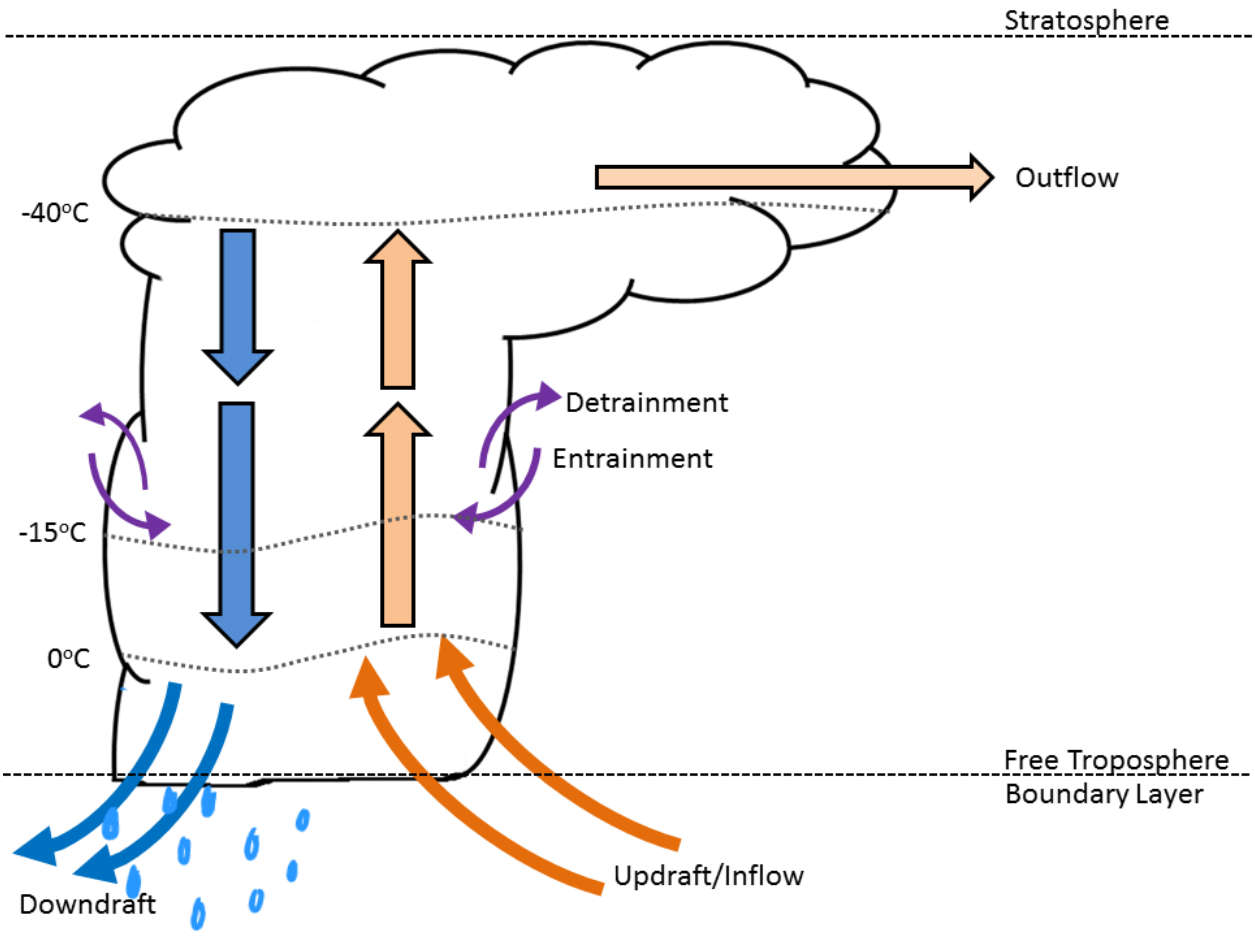

Figure 2.1: Simple schematic of a mature thunderstorm highlighting inflow (orange arrows), outflow (light orange arrow), and downdraft (blue arrows). Entrainment and detrainment along the cloud sides are represented by purple arrows.

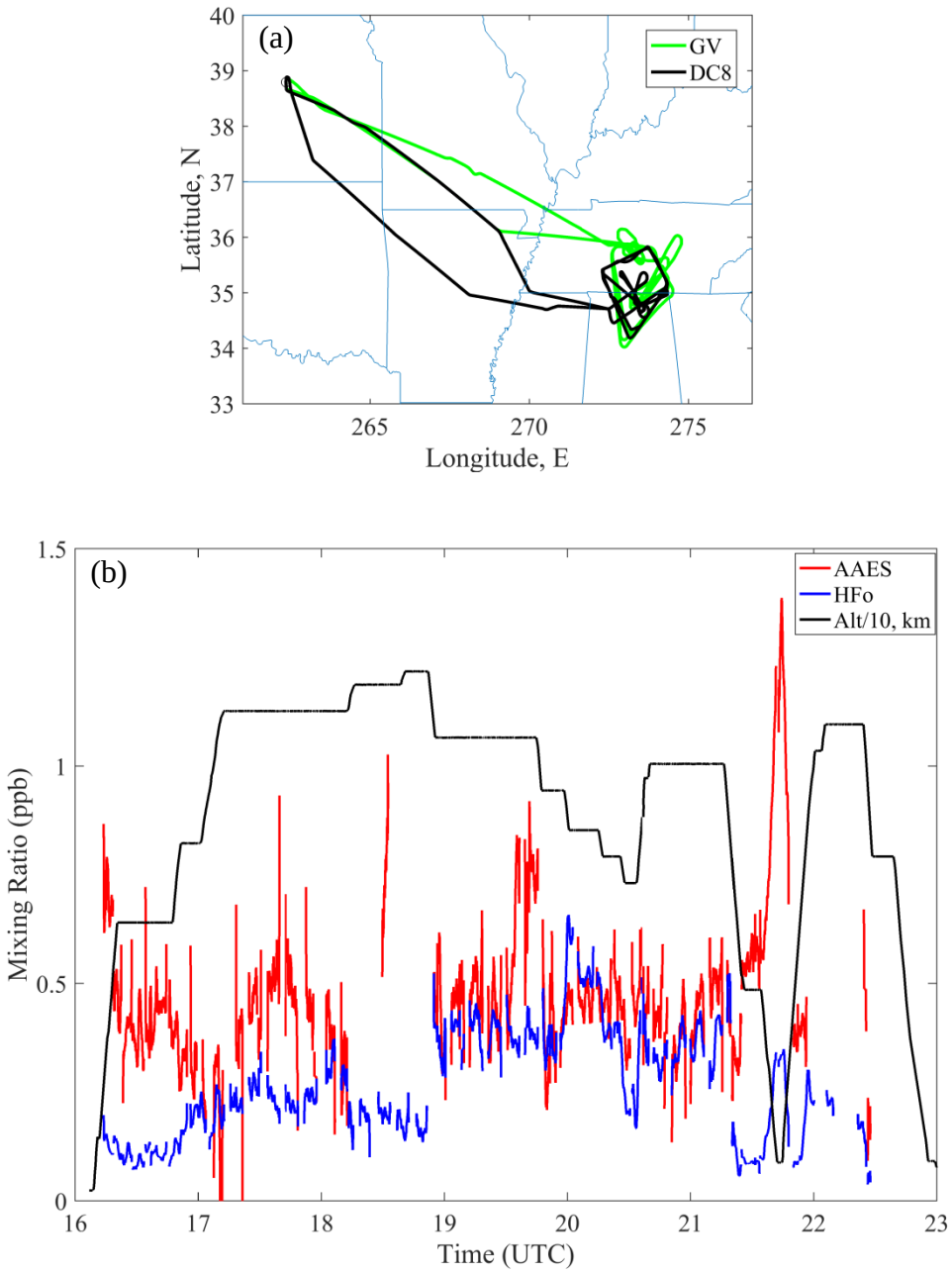

Figure 2.2: a) Map of DC8 (black) and Gulfstream V (GV, green) flight tracks for RF 03, May 21, 2012, b) Time series of 1 minute moving mean for formic acid (HFo) and acetic acid equivalent sum (AAES) mixing ratios (ppb) along with the flight track (km/10)

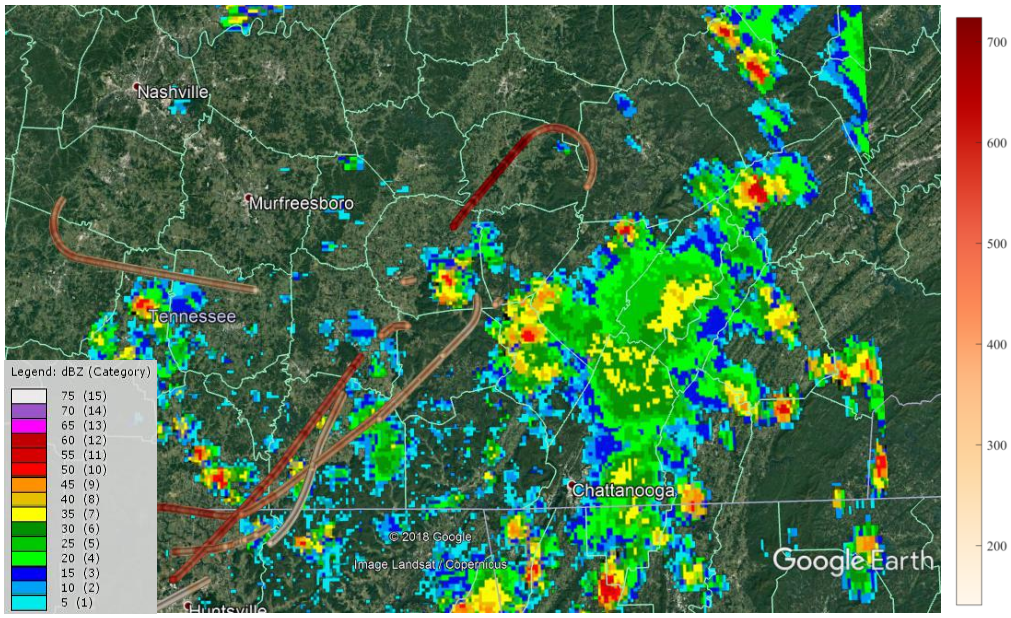

Figure 2.3: NEXRAD 19:46 UTC maximum column radar reflectivity superimposed on Google Earth. The formic acid mixing ratio (ppt) plotted along the Gulfstream V flight track on May 21, 2012 from 20:00-21:00 UTC is shown as well. The convection nearest the formic acid peak is highlighted by a white box.

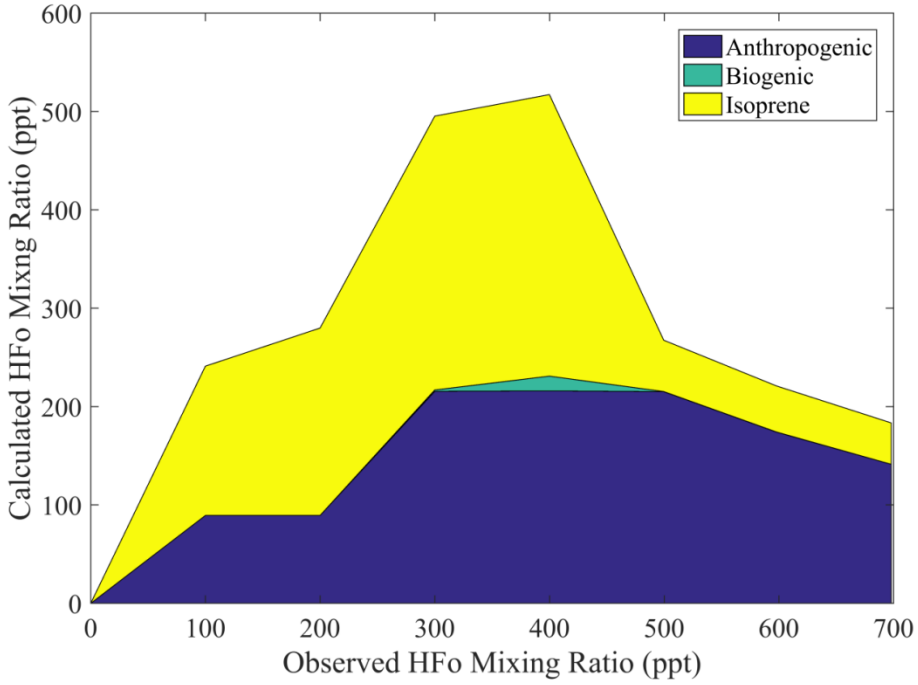

Figure 2.4: Observational formic acid (HFo) mixing ratios (ppt) compared to a pseudo steady state maximum HFo (ppt) calculation using DC3 aircraft data and the MOZART gas phase reactions. The anthropogenic sources include ethene and acetylene. The biogenic sources are a-pinene, b-pinene, limonene, and MBO. A 31% HFo production from isoprene ozonolysis is shown as well. The only gas phase loss is HFo+HO.

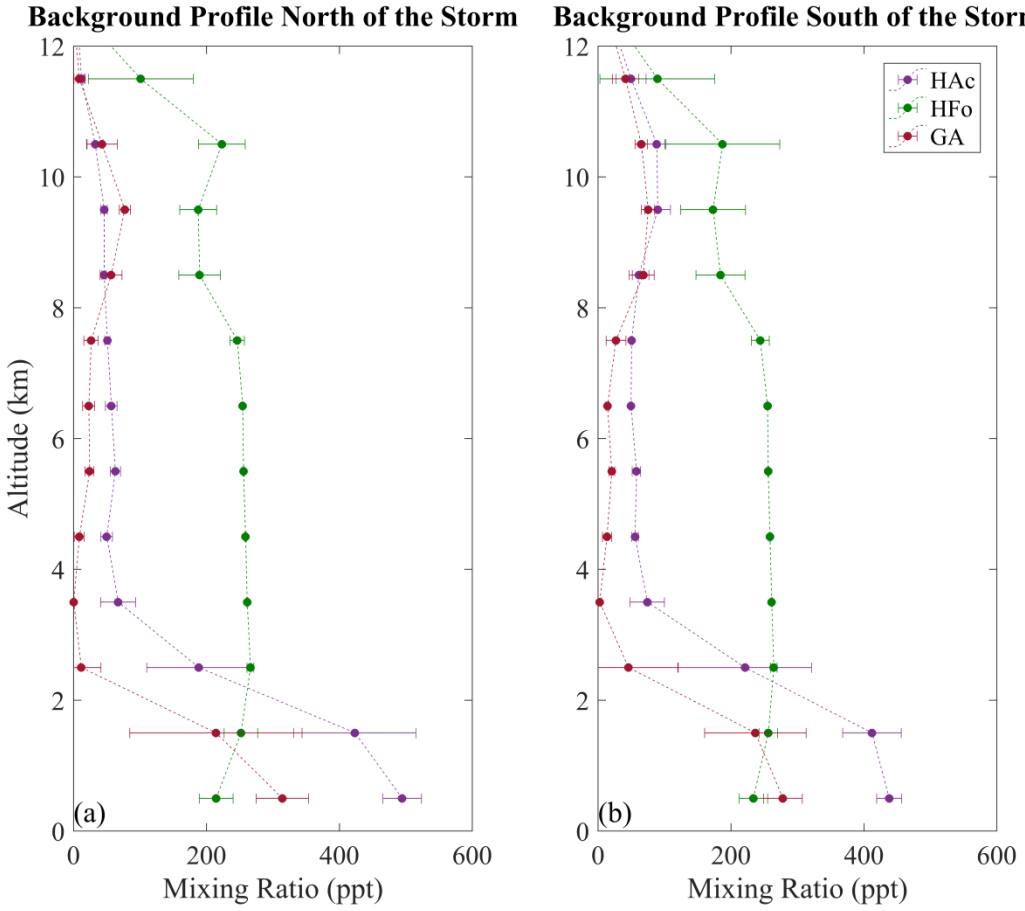

Figure 2.5: WRF-Chem non-convective, or background, air altitude profiles (km) to the north (a) and south (b) of the main storm for formic acid (HFo), acetic acid (HAc), and glycolaldehyde (GA) (ppt). Background air is defined as having an ice and cloud mixing ratio < 0.01 g/kg and radar reflectivity of zero. Data are averaged over 1 km bins from the surface to 12 km which is the maximum altitude of the simulated storm outflow. Error bars represent 1 standard deviation.

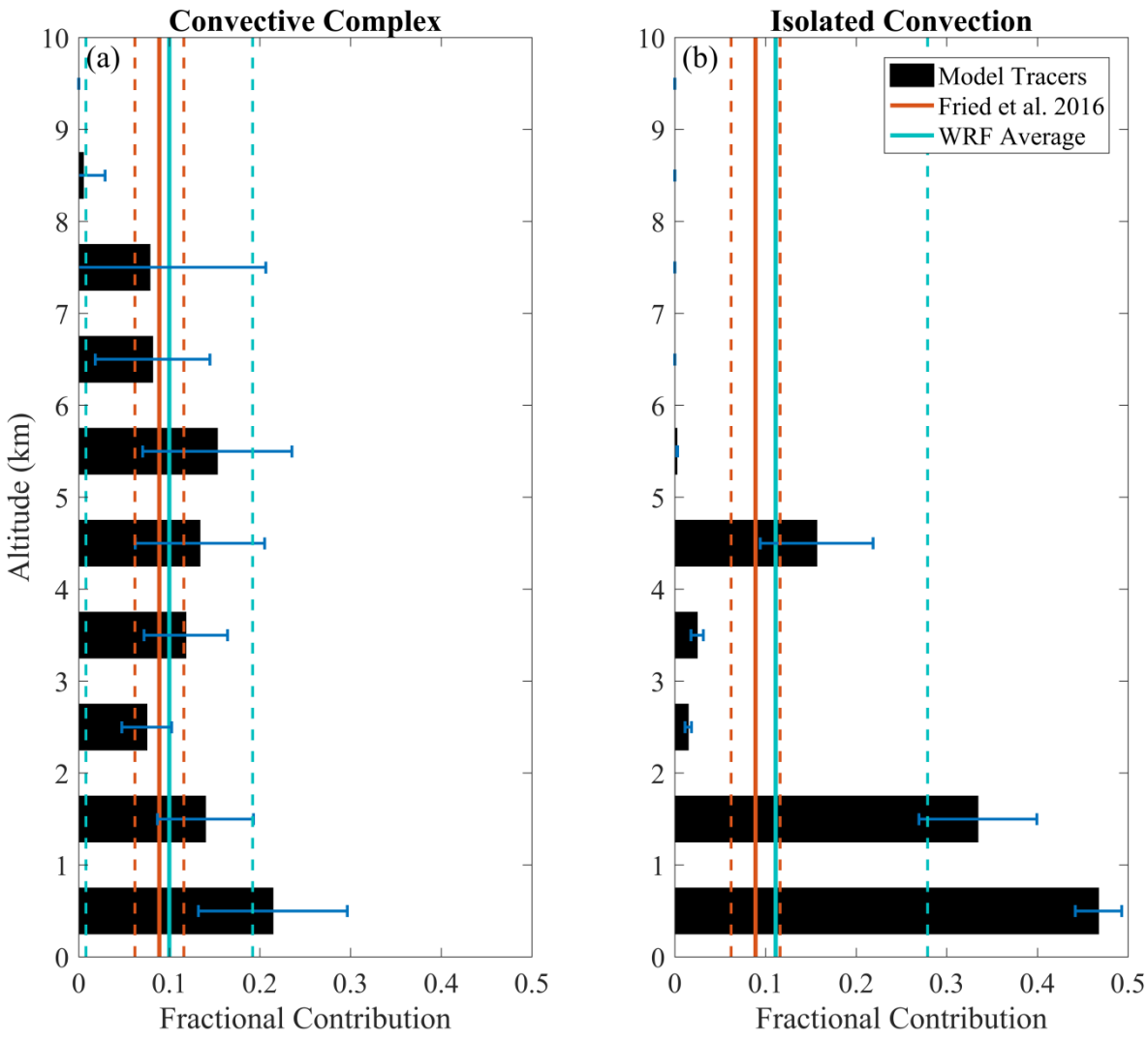

Figure 2.6: WRF-Chem passive tracers altitude profiles representing the entrainment fraction (black bar) as a function of altitude (km) for (a) the convective complex and (b) isolated convection. Tracers were released in 1 km bins from the surface to ~18 km and set to 1.0 in clear air outside the storm (defined by cloud water mixing ratio < 0.01 g/kg). Entrainment is calculated for each 1 km altitude layer by taking the average percent contribution of each within the outflow. Error bars represent 1 standard deviation. The average WRF-Chem entrainment rate for the whole profile (solid cyan line) is provided as well along with 1 standard deviation (dashed cyan line). The observational average entrainment rate (solid red line), calculated in Fried et al. 2016, along with the 1 standard deviation (dashed red line) is shown as well. The convective complex tracers were added at 20:50 UTC. The isolated convection tracers were added at 19:40 UTC. Note the difference in x-axis.

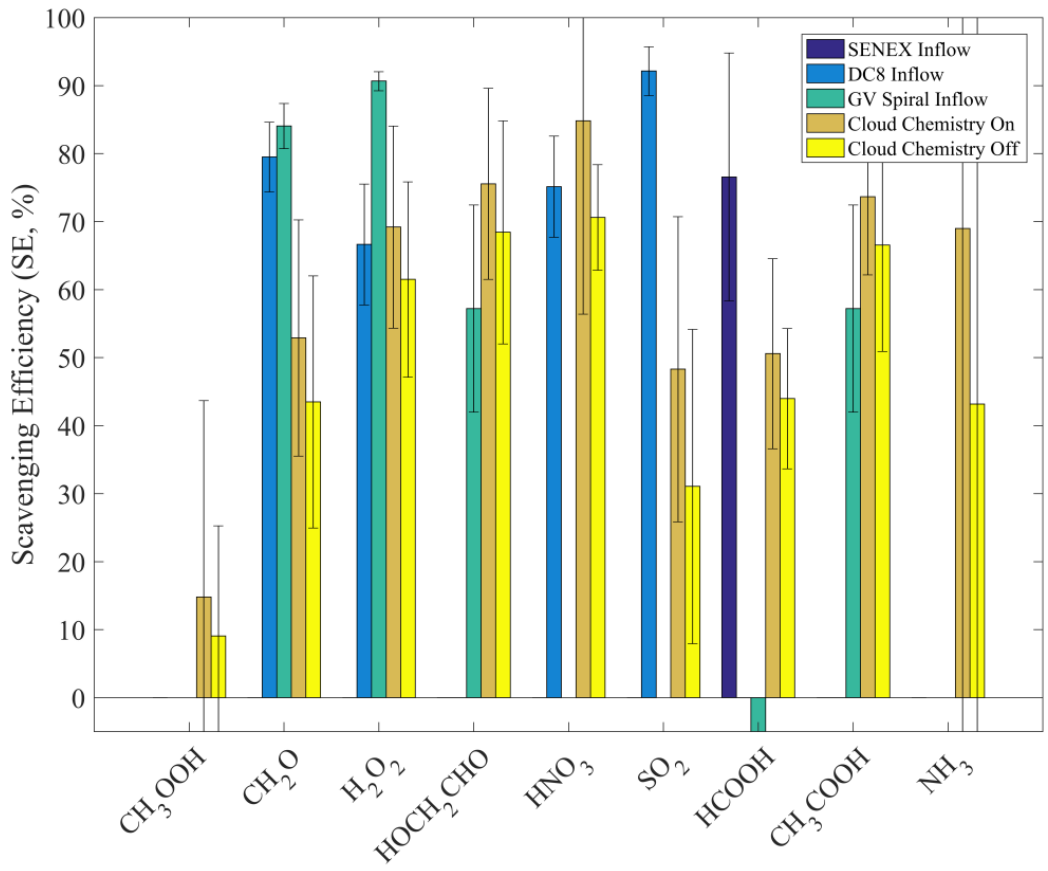

Figure 2.7: The convective complex WRF-Chem (orange and brown) and observed (blues and green) average scavenging efficiencies (SE) for soluble species. Error bars represent one standard deviation. All observed SE used the Bela et al. (2016) defined outflow period (GV measurements from 20:50:30-21:14:30, 10 km). DC8 Inflow SE values used the Bela et al. (2016) defined inflow period (DC8 measurements from 19:30:43 – 19:38:00). GV Spiral Inflow used the GV spiral data (below 1 km) for the storm inflow. SENEX (Southeastern Nexus) Inflow used formic acid data below 1 km for the inflow value. Cloud Chemistry On and Cloud Chemistry Off refer to the two WRF-Chem simulations. SE was determined using two simulations – one with precipitation scavenging and one without. Cloud Chemistry On refers to the addition of aqueous chemistry.

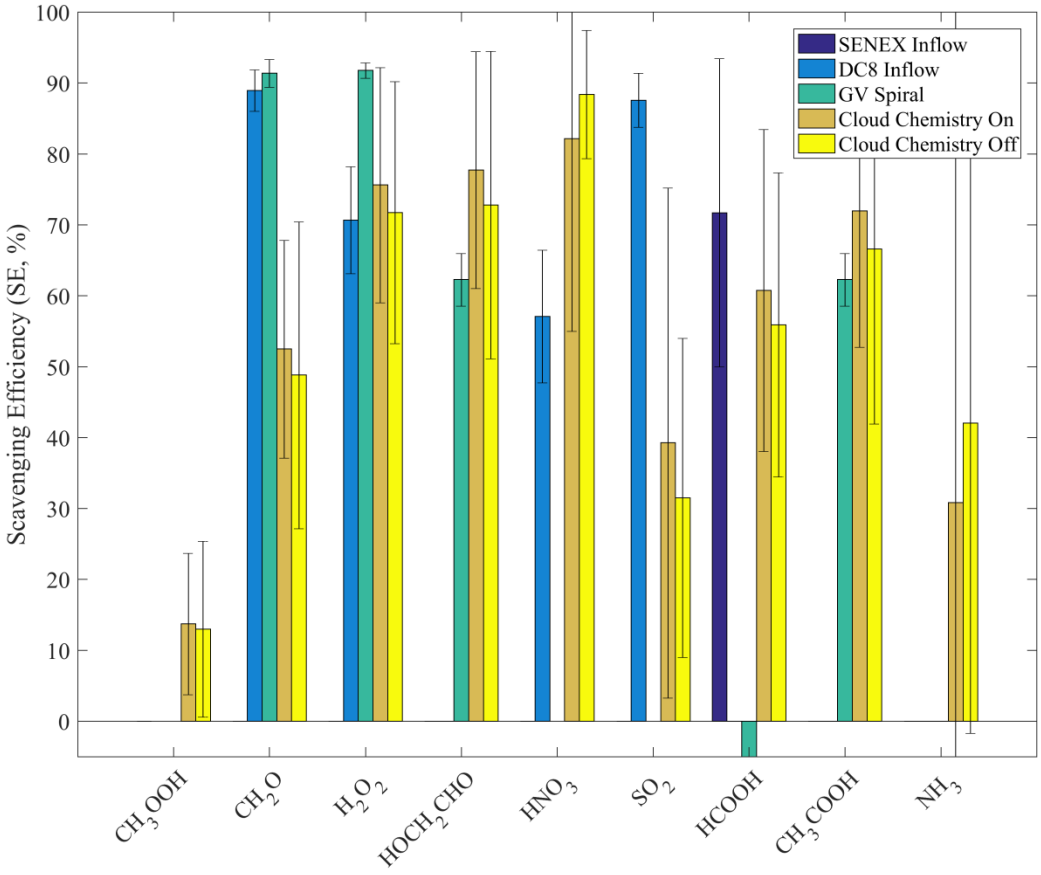

Figure 2.8: Similar to Figure 2.7 but for the isolated convection. The same observed inflow categories as Figure 2.7. The observed outflow values are from the isolated convection sampled (19:48 – 20:27 UTC) east of the main storm. WRF-Chem SE values are calculated for the isolated storm at the AL/TN border just south of the main storm.

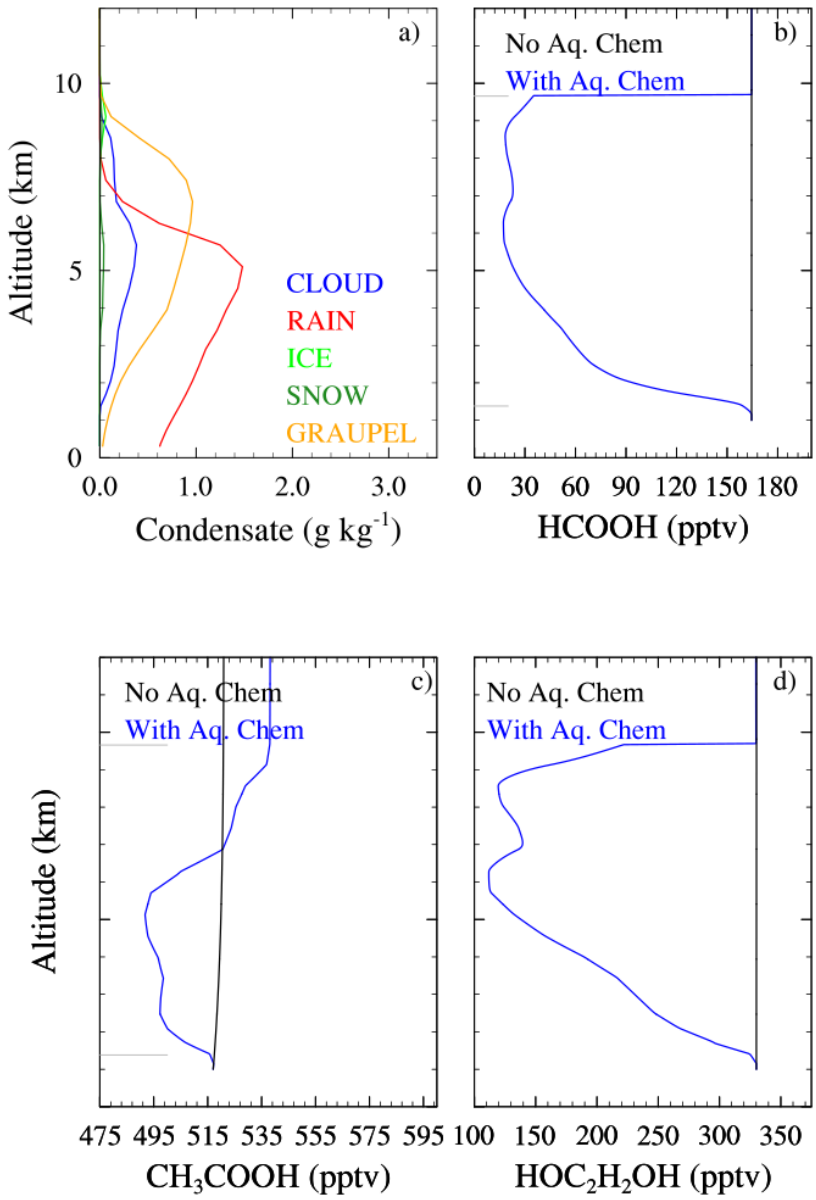

Figure 2.9: Box model simulation for the convective complex using WRF-Chem surface mixing ratios and hydrometeors for 21:40 UTC. This simulation was for a constant pH of 5, only CH_2O as an HFo source, and aqueous chemistry to 258 K. The different plots represent: (a) the storm hydrometeors, (b) HFo mixing ratio, (c) HAc mixing ratio, (d) GA mixing ratio. For b-d the black line represents no cloud and the blue line is with a cloud. The gray lines are the cloud bottom and top.

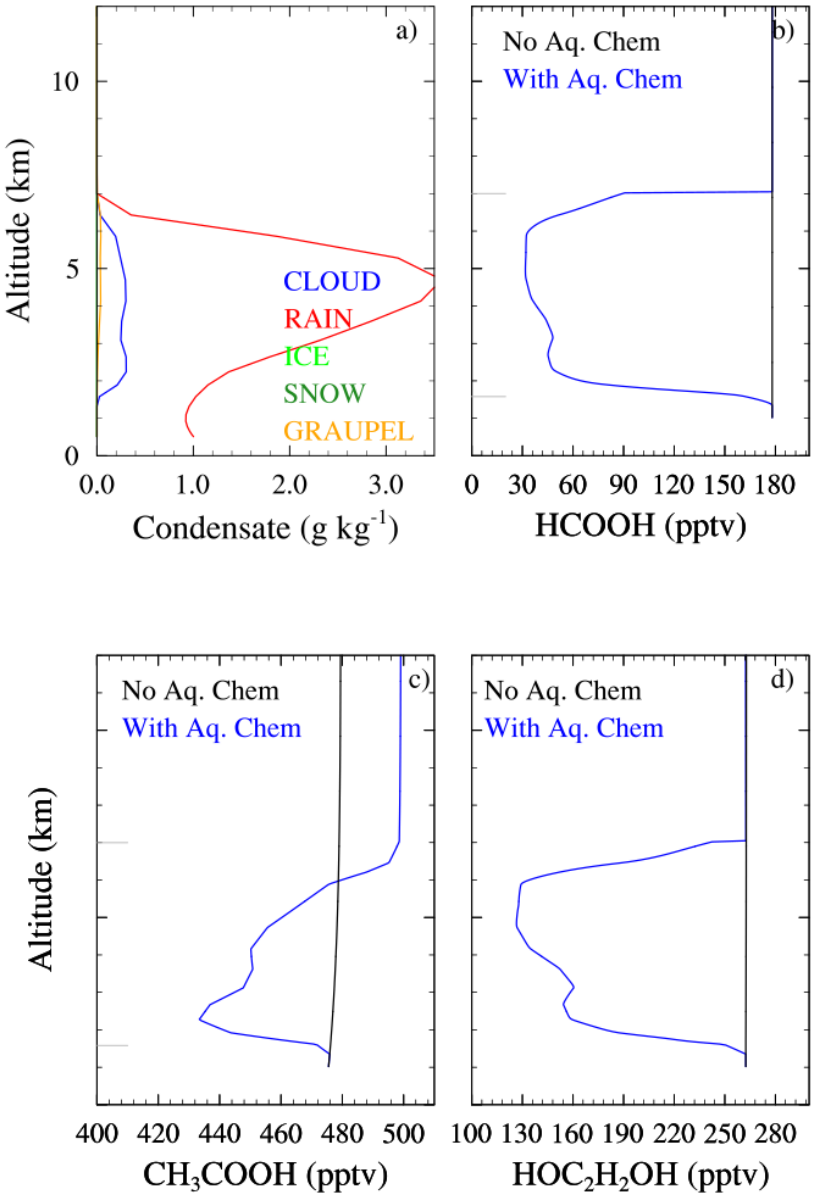

Figure 2.10: Similar to Figure 2.9 but for the isolated convection.

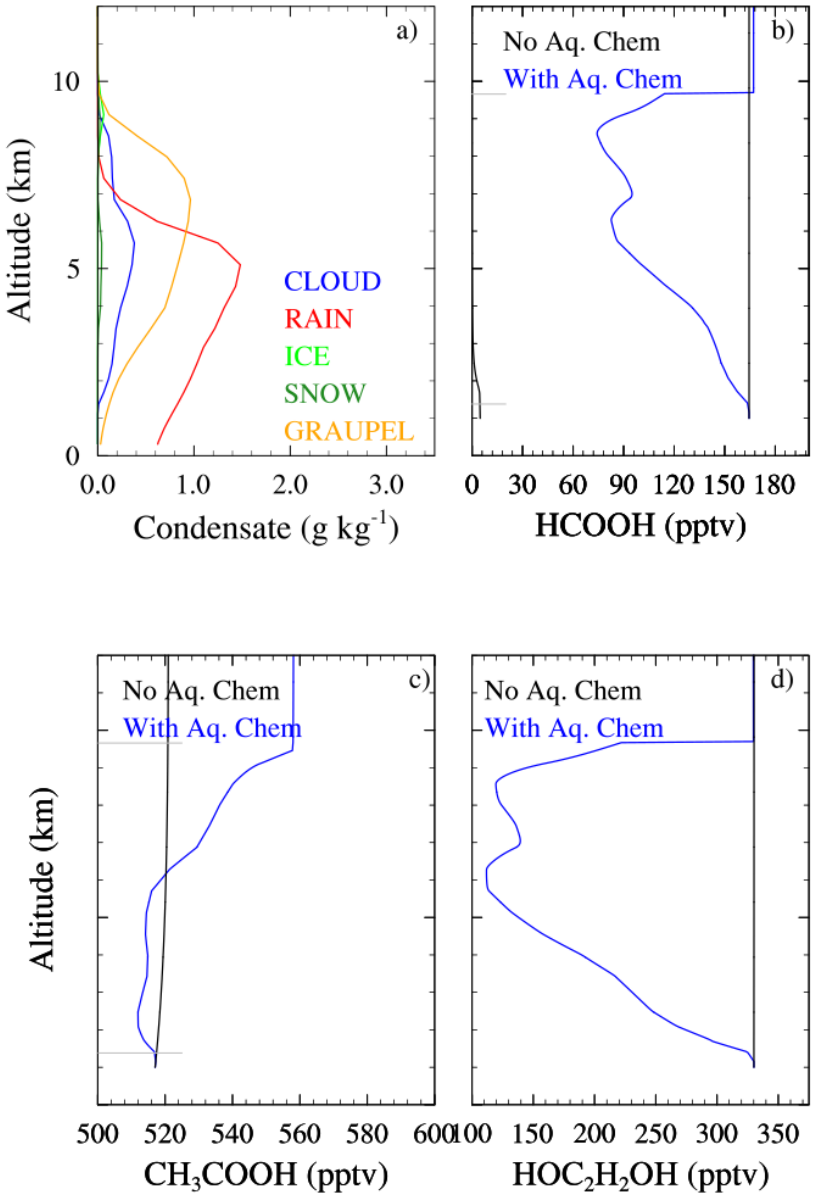

Figure 2.11: Box model simulation for the convective complex using WRF-Chem surface mixing ratios and hydrometeors for 21:40 UTC. This simulation was for a constant pH of 3.5, multiple HFo aqueous sources, and aqueous chemistry to 233 K. The different plots represent: (a) the storm hydrometeors, (b) HFo mixing ratio, (c) HAc mixing ratio, (d) GA mixing ratio. For b-d the black line represents no cloud and the blue line is with a cloud. The gray lines are the cloud bottom and top.

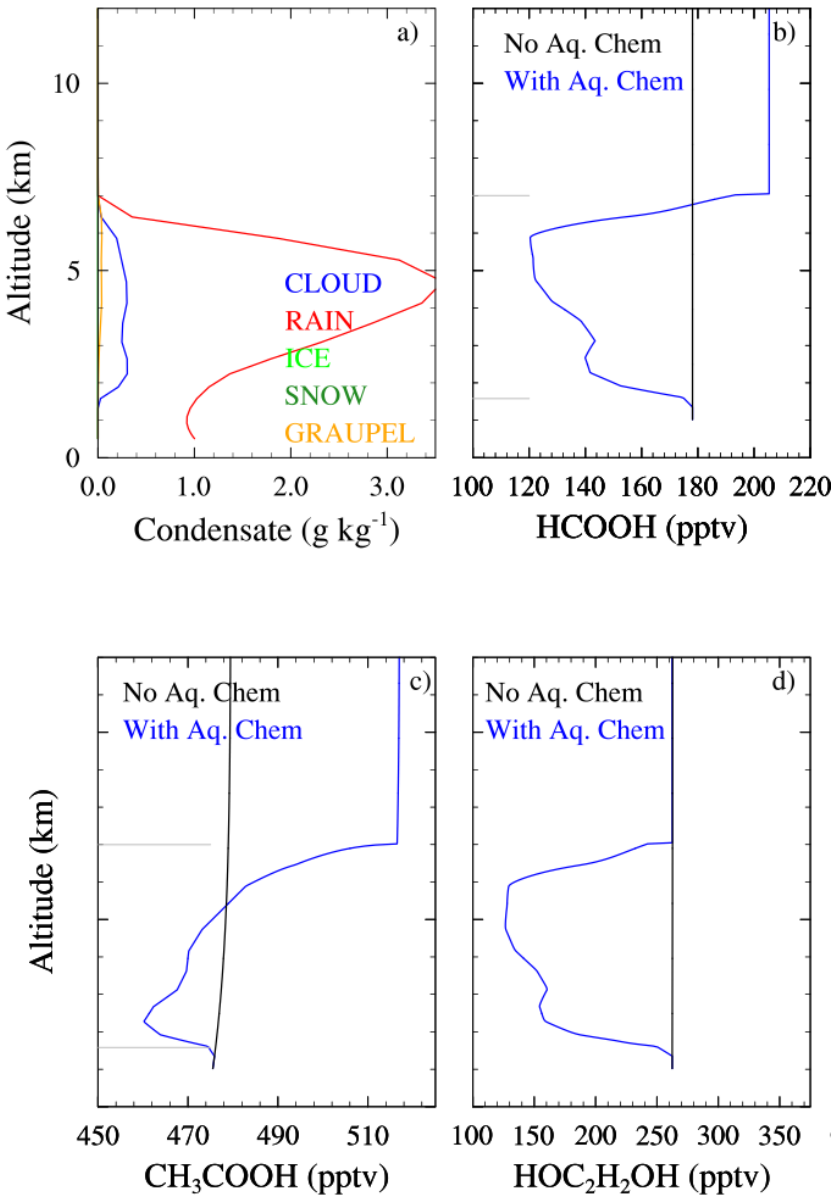

Figure 2.12: Similar to Figure 2.11 but for the isolated convection.

Supplemental Information

Table S2.1: Box Model Aqueous Reactions for Formic Acid, Acetic Acid, and Glycolaldehyde

Formic Acid (HCOOH)
CH_2O + HO → **HCOOH** + HO_2
HO + OCHCHO → 2 **HCOOH**
H_2O_2 + OCHCHO → 2 **HCOOH**
H_2O_2 + OCHCOOH → **HCOOH** + CO_2
HCOOH + HO → CO_2 + HO_2
HCOOH + H_2O_2 → CO_2
Acetic Acid (CH_3COOH)
HO + $CH_3COCOOH$ → **CH_3COOH** + HO_2 + CO_2
HO + CH_3CHO → HO_2 + **CH_3COOH**
H_2O_2 + $CH_3COCOOH$ → **CH_3COOH** + CO_2
HO + **CH_3COOH** → HO_2 + 0.15 CH_2O + 0.85 $H_2COHCHO$
Glycolaldehyde ($H_2COHCHO$)
HO + CH_3COOH → HO_2 + 0.15 CH_2O + 0.85 **$H_2COHCHO$**
HO + **$H_2COHCHO$** → HO_2 + HOCOCOH

Table S2.2: Convective Complex Inflow and Outflow Values (ppb) used for Scavenging Efficiency Calculation

Type	Source	n-butane	HNO_3	CH_2O	H_2O_2	CH_3OOH	SO_2	HCOOH	CH_3COOH	$HOCH_2CHO$
DC8 Inflow	DC8	0.214 ± 0.0386	1.18 ± 0.111	2.36 ± 0.476	1.15 ± 0.287	N/A	0.317 ± 0.0940	2.77 ± 1.63*	N/A	N/A
Spiral Inflow	GV	0.171 ± 0.0176	N/A	2.76 ± 0.292	3.02 ± 0.323	N/A	N/A	0.332 ± 0.0157	1.32 ± 0.161	N/A
Outflow	GV	0.127 ± 0.0085	0.240 ± 0.0660	0.296 ± 0.0780	0.197 ± 0.0121	0.313 ± 0.0565	0.0167 ± 0.0093	0.311 ± 0.0398	0.391 ± 0.153	N/A
Scav On Cloud Chem Off	WRF	N/A	0.0730 ±0.0187	0.416 ±0.106	0.789 ±0.265	0. 415 ±0.0391	0.203 ±0.0444	0.1361 ±0.0244	0.0682± 0.0299	0.0390 ± 0.0193
Scav On Cloud Chem On	WRF	N/A	0.0209± 0.0303	0.3754 ±0.0751	0.588 ± 0.219	0.410±0.0759	0.0612 ±0.0143	0.1204 ±0.0317	0.0577 ±0.0188	0.0327 ± 0.0168

*SENEX

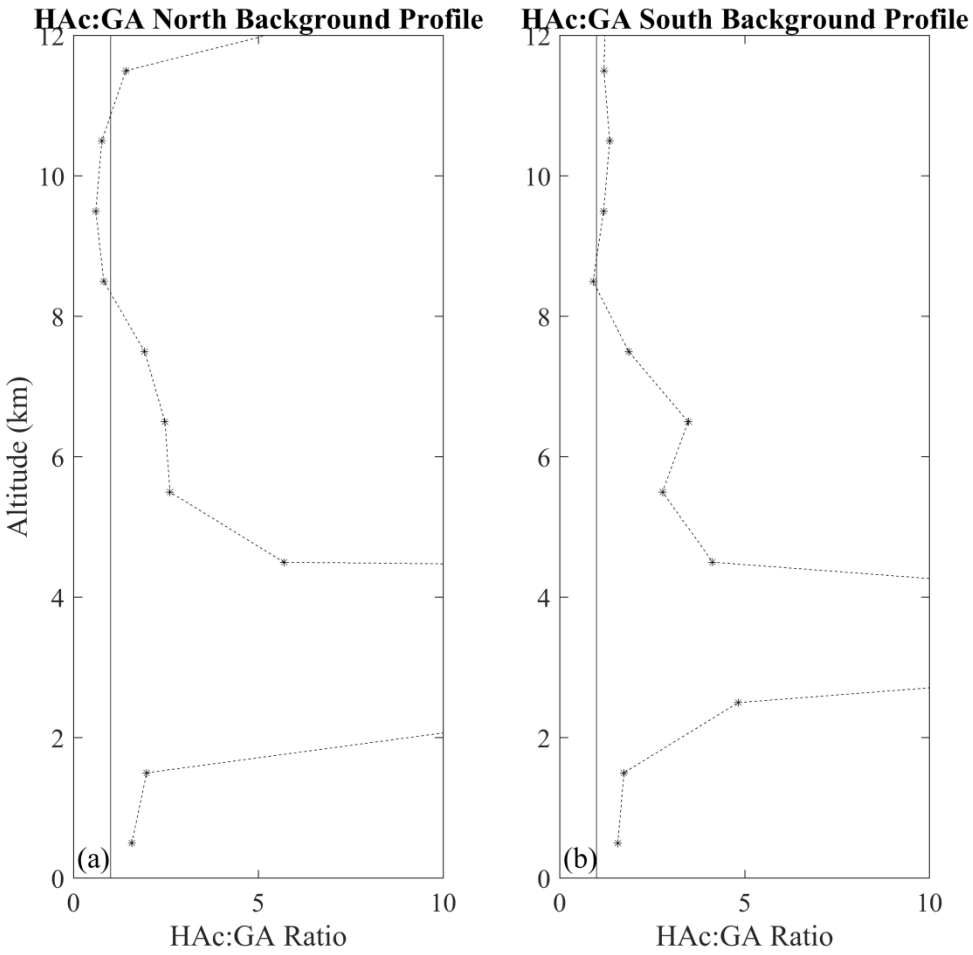

Figure S2.1: HAc:GA ratio in the WRF-Chem background profile (a) to the north of the storms and (b) to the south of the storms. Background air is defined as having a cloud mixing ratio < 0.01 g/kg and radar reflectivity of zero. Data are averaged over 1 km bins from the surface to 12 km which is the maximum altitude of the simulated storm outflow. Error bars represent 1 standard deviation.

Figure S2.2: WRF-Chem background air altitude profiles (km) to the north (a) and south (b) of the main storm for hydrogen peroxide, methyl hydroperoxide, and formaldehyde (ppt). Background air is defined as having a cloud mixing ratio < 0.01 g/kg and radar reflectivity of zero. Data are averaged over 1 km bins from the surface to 12 km which is the maximum altitude of the simulated storm outflow. Error bars represent 1 standard deviation.

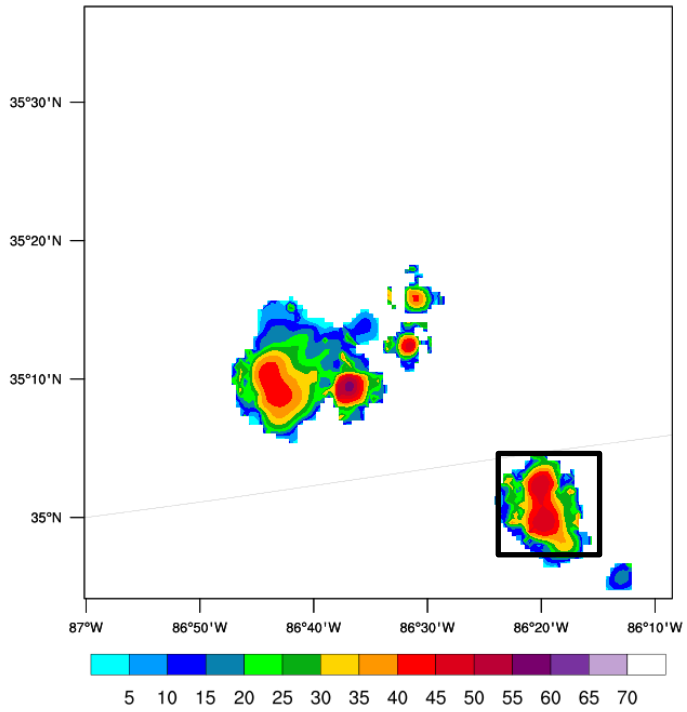

Figure S2.3: WRF-Chem maximum column radar reflectivity at 21:10 UTC with a black box designating the region used to calculate the scavenging efficiency for isolated convection

MANUSCRIPT 3

Characterizing Formic and Acetic Acid Sources on the Colorado Front Range

By

Victoria Treadaway[1], Eric Apel[2], Rebecca Hornbrook[2], Brian Heikes[1]

To be submitted to Journal of Geophysical Research: Atmospheres

---

[1]Graduate School of Oceanography

[2]National Center for Atmospheric Research

Abstract

Formic acid (HFo) and acetic acid equivalent sum (AAES), the sum of acetic acid (HAc) and glycolaldehyde (GA), distributions on the Colorado Front Range are presented. Chemical ionization mass spectrometry data was collected during the Front Range Air Pollution and Photochemistry Éxperiment (FRAPPÉ) field campaign in July and August 2014 onboard the NCAR/NSF C-130. HFo and AAES distributions were evaluated for different sources using geographic divisions and chemical emission source markers. Overall, AAES was several parts per billion higher than HFo. HFo was highest near biogenic sources based on both classification systems with the Denver Metropolitan area the second highest region. AAES was highest in the Denver Metropolitan area based on the geographic divisions. Chemically AAES medians were highest, and almost identical, for the biogenic and oil and natural gas (O&NG) regions. HFo and AAES were assessed during two potential upslope flights, August 11th and 12th. These two were chosen because both were forecasted to be upslope, or mountain-valley, circulation flights; however, this was only observed on August 12th. AAES and HFo distributions on August 11th and 12th paralleled with the campaign-wide HFo and AAES distributions. Elevated HFo was found in the upslope and spillover (1.6 ppb) with a similar distribution pattern to ozone. The highest AAES was observed near anthropogenic sources (14 ppb in Greeley, CO) relative to the foothills and spillover. HFo, HAc, and GA secondary production was estimated using the Master Chemical Mechanism (MCM) version 3.3.1 for the two case study flights. The majority of HFo formation came from the Criegee intermediate with a mixture of biogenic (isoprene, MBO, and MVK) and anthropogenic (ibutene, propene, and

acrolein) sources. Isoprene ozonolysis represented a third of HFo production. PAN and acetaldehyde were the two primary HAc sources. MBO, MVK and acetaldehyde controlled GA production. GA estimated production was lower than HAc and GA loss was an order of magnitude higher. Based on gas phase processes HAc represented a greater portion of AAES than did GA.

1. Introduction

Formic (HFo) and acetic (HAc) acid are the most abundant carboxylic acids in the troposphere yet their production pathways remain uncertain. Both acids are underestimated in models which has been linked to missing sources (Millet et al., 2015; Stavrakou et al., 2012; Yuan et al., 2015). Organic acids contribute up to 60% of the natural acidity of precipitation in remote regions and 16% in urban areas (Khare et al., 1999). With the decrease of NO_x and SO_x emissions organic acids contributions to acidity should increase in urban to rural areas. Satellite evidence indicates that HFo represents between 30-50% of continental United States summertime rain acidity (Stavrakou et al., 2012). Both organic acids are photochemically long-lived (20+ days with respect to HO) but subject to dry deposition and episodic wet deposition at the Earth's surface resulting in a 1-10 day lifetime in the boundary layer. They represent a relatively long-lived intermediate product in the oxidation of organic matter and we need to understand their sources.

Primary emissions for both acids include vegetation, agriculture, and motor vehicle emissions (Khare et al., 1999; Paulot et al., 2011). Substantial HAc and HFo emissions are also associated with intensive animal farming (i.e. concentrated animal feedlot operations, CAFOs) (Mårtensson et al., 1999). The high ammonia emitted

from CAFOs may enhance uptake of HFo and HAc onto particulate matter as well. Both organic acids have been measured as primary emissions in motor vehicular exhaust with greater HAc relative to HFo (Kawamura et al., 1985). It is hypothesized that both organic acids are released as a result of incomplete combustion which is supported by the high organic acid concentration measured in used oil (Kawamura et al., 1985). Additionally, biomass burning plumes contain organic acids and these are the third most important emitted carbon reservoir (Yokelson et al. 2009).

Secondary production is also a significant source for both acids especially from biomass burning gases, secondary organic aerosols, and photochemical production from volatile organic compounds (VOCs) and oxygenated volatile organic compounds (OVOCs) of natural and anthropogenic origin (Khare et al., 1999; Paulot et al., 2011; Yuan et al., 2015). Reported HFo photochemistry sources include isoprene, methyl vinyl ketone (MVK), ethene, and acetylene. Reported HAc photochemistry sources include peroxyacetyl nitrate, acetaldehyde, and propene. Unfortunately, a great deal of uncertainty remains concerning the yield and mechanism of these various *in situ* chemical reactions although the critical component is the source strength and fate of the Criegee intermediate from alkene ozonolysis, e.g.,:

$$H_2C = CH_2 + O_3 \rightarrow HCHO + HCOO^- \quad (1)$$

(Millet et al., 2015). This pathway impacts ozone photochemistry and is potentially a significant HO_x source in urban environments (Finlayson-Pitts & Pitts Jr, 1997).

HAc measurements with our chemical ionization mass spectrometer are sensitive to an isobaric interference with hydroxyacetaldehyde, or glycolaldehyde (Treadaway et al., 2018). Glycolaldehyde (GA) is directly emitted in smoldering

biomass burning plumes (Yokelson et al., 1997) and there are no other reported primary sources. Secondary production is important for GA with the highest reported mixing ratios associated with biogenic precursors including isoprene, MVK, and 2-methyl-3-buten-2-ol (MBO) (Lee et al., 1998; Tuazon & Atkinson, 1989), biomass burning emissions (Johnson et al., 2013; Yokelson et al., 1997), and the HO oxidation of unsaturated anthropogenic VOCs such as ethene (Niki et al., 1981). Peroxyacetyl nitrate and acetaldehyde are also listed as GA secondary sources in the Master Chemical Mechanism (MCM, 2018).

The Colorado Northern Front Range Metropolitan Area (NFRMA) has a variety of primary and secondary HFo, HAc, and GA sources including biogenic emissions, crude oil and natural gas production, CAFOs, and urban emissions from refineries, traffic, electrical generation, and manufacturing concentrated in the Denver Metropolitan area. Despite efforts to limit emissions of ozone precursors like NO_x and VOCs, NFRMA continues to have multiple ozone exceedances in summer (Flocke et al., 2013). The NFRMA is classified as a "moderate" nonattainment area by the EPA (EPA Federal Registrar, 2016) using the 2008 ozone standard, defined by an eight hour ozone average greater than 75 ppb. With the standard lowered to 70 ppb it is very likely NFRMA will have more exceedance days. The wide variety of precursor sources in Colorado and the failure of emission reductions to prevent ozone exceedance events make it essential to study how atmospheric composition impacts NFRMA air quality. Understanding HFo, HAc, and GA sources are important as they participate in ozone processing and add mechanistic details on the carbon cycle in this region.

To help characterize NFRMA air chemistry, the Front Range Air Pollution and Photochemistry Éxperiment (FRAPPÉ) sampled the atmosphere over northern Colorado in the summer of 2014. FRAPPÉ flights were centered over the NFRMA and were able to distinguish local, point-source emissions versus out-of-state emissions as well as assess air chemical evolution downwind. Simultaneously the NASA field campaign, Deriving Information on Surface Conditions from Column and Vertically Resolved Observations Relevant to Air Quality (DISCOVER-AQ), conducted one of their field experiments over the Colorado Front Range directly expanding the scope of measurements available. The two studies complement one another.

The NFRMA meteorology in summer often experiences local mountain-valley winds, or upslope-downslope, flow and isolated summer thunderstorms. Morning solar heating of high terrain and sun facing slopes causes a pressure gradient that draws air from the plains toward the Rocky Mountain eastern valley. The air is transported along the Front Range and can transport polluted air masses to the mountains. If the upslope event is strong enough the winds travel vertically up the eastern side of the Rocky Mountains and mix with prevailing westerlies or “spillover” onto the western side of the mountains. These upslope events can compound the air quality issue by transporting NFRMA pollution to the mountains. Furthermore, re-entrainment back into the boundary layer could bring part of the pollution back into the Front Range resulting in combining emissions from multiple days (Pfister et al., 2017). FRAPPÉ flew multiple upslope-downslope flights (Pfister et al., 2017; Sullivan et al., 2016).

Pfister et al. (2017) identified strong upslope events that were sampled by the C-130 including August 12th (RF 12) which is presented here.

This paper describes HFo and the combined HAc and GA, reported here as acetic acid equivalent sum (AAES), distributions during FRAPPÉ and how they vary under the influence of sources, photochemistry, and meteorology across the Colorado Front Range. Geographic divisions and literature defined chemical markers are used in this analysis to characterize dominant source types for HFo and AAES comparing natural and anthropogenic sources found on NFRMA. Two example flights are presented in which upslope flow was predicted with spillover into Granby on the western slope. Secondary production of HFo, HAc, and GA was explored using established secondary reaction pathways and aircraft measurements.

2. Methods

2.1 FRAPPÉ Field Campaign

In situ measurements during FRAPPÉ were made onboard the NSF/NCAR C-130. The C-130 flew 15 flights between July 17 and August 18, 2014 with 11 out of the 15 flights done in conjunction with NASA's DISCOVER-AQ program. The C-130 carried an extensive array of instrumentation. Chemical instrumentation and measurements used in this analysis are listed in Table 3.1. The data are available at https://www-air.larc.nasa.gov/cgi-bin/ArcView/discover-aq.co-2014?C130=1. Altitude is reported here as above ground level (a.g.l). This is the difference between the gps altitude and the elevation measured by the aircraft. This puts the altitude in relation to the surface regardless if along the plains or in the foothills. Some flights

were missing elevation data and they are eliminated from any boundary layer calculations.

2.2 Organic Acid Instrumentation

Organic acids were measured with the PCIMS (Peroxide Chemical Ionization Mass Spectrometer). PCIMS is a quadrupole negative ion mass spectrometer. PCIMS set-up including calibration, blanks, and ion cluster chemistry is explained in detail in Heikes et al. (2018), O'Sullivan et al. (2018), and Treadaway et al. (2018) and is only briefly discussed here. In flight, air was sampled with a HIAPER Modular Inlet (HIMIL) hard mounted on the fuselage, extending beyond the aircraft boundary layer. The HIMIL inlet surfaces were lined with PFA Teflon® tubing. The HIMIL and gas transfer lines were heated to 343K during FRAPPÉ to minimize artifacts caused by the adsorption and/or release of the target gases from or onto the inlet surface.

This was the first field deployment of the PCIMS explicitly using a dual-ionization scheme involving CO_2 and CH_3I. Reagent CO_2 (400 ppm, 0.080 slpm) in ultrapure air was mixed with a second reagent gas CH_3I (5 ppm in N_2, 0.0005 slpm) and carried by an N_2 stream. The reagent gas blend of CH_3I, CO_2, O_2, and N_2 yielded responses for water vapor, organic acids, hydroxyacetaldehyde (discussed below), and peroxides. Organic acids were quantified using the I^- clusters, I^-(HFo) and I^-(HAc) (Heikes et al., 2018; Treadaway et al., 2018). Peroxides, H_2O_2 and CH_3OOH, were quantified using $O_2^-(CO_2)$ and I^- clusters (Heikes et al., 2018; O'Sullivan et al., 2018).

The PCIMS measurement cycle was 720 sec. and included a 90 sec. blank, followed by a 75 sec. gas standard addition, and then a 555 sec. measurement period. Sixteen mass-to-charge ratios were serially sampled once every 3.5 seconds. Standard

additions to ambient air were performed by evaporating aqueous organic acids (5.88 mM HFo and HAc) and peroxides (15.9 mM H_2O_2, 14.9 mM CH_3OOH, and 14.9mM CD_3OOH) standards into sample air. Three different trap set-ups were deployed during FRAPPÉ for the field blank. Research flights (RF) 1 through 5 (July 26th – 31st) and 7 (August 3rd) used a Carulite 200® trap. RF06 (August 2nd) used a Carulite 200® and a $NaHCO_3$ trap in series. RF08 through RF 15 (August 6th – 18th) used a Carulite 200® followed by a NaOH trap and was found to be the most effective way to remove both peroxides and organic acids (Treadaway et al. 2018).

Post-campaign, hydroxyacetaldehyde, or glycolaldehyde (GA), was found to be an isobaric interferent for HAc at m/z 187. Its PCIMS sensitivity relative to HAc was between 1:1 and 1:10 for HAc:GA (Treadaway et al., 2018). HAc and GA are necessarily reported as the Acetic Acid Equivalent Sum (AAES) since only HAc was used in the field as a calibrant. Two other potential interferences examined post-mission were ethanol and propanol. Ethanol has a PCIMS response that was 3.3% that of HFo and was subtracted from all HFo data reported here (Treadaway et al., 2018). 1- and 2- propanol each gave a 1% response relative to HAc. 2-propanol was measured by the TOGA instrument (Rebecca Hornbrook personal communication) and has a large uncertainty ($\pm$100%). We used the 2-propanol to estimate the potential interference and subtracted 2%, representing 1- and 2-propanol, of the campaign 2-propanol maximum (509 ppt) from the AAES data.

2.3 Source Characterization

The Colorado Front Range was characterized using geographic and chemical parameters. Two potential boundary layer thickness were defined, 1000 m and 2300 m

a.g.l. (Bahreini et al., 2018; Vu et al., 2016). A map (Figure S3.1) highlights three defined geographic emission source regions representing primarily urban sources in the Denver Metropolitan area (red), forest vegetation including Rocky Mountain National Park (green), and CAFOs/oil and gas production in the Greeley area (blue). CAFO and oil and natural gas (O&NG) were co-located geographically and could not be separated.

A chemical identification scheme was developed to better identify source types and separate O&NG from CAFOs. The source type parameters (Table S3.1) were developed from literature work (Baker et al., 2008; Eilerman et al., 2016; Gilman et al., 2013; Hornbrook et al., 2015, 2017; Kim et al., 2010). Different authors have suggested and used different species and thresholds to develop source characterization. Table S3.1 summarizes this work. CAFOs are characterized by an enhancement in NH_3 and low oil and gas markers, propane/ethyne and i-/n-pentane ratios, to try and separate the oil and gas emissions from CAFO sources. Biogenic emissions are characterized by the presence of known biogenic markers such as isoprene, methyl vinyl ketone (MVK), 2-methyl-3-buten-2-ol (MBO), b-pinene, and methacrolein (MACR). Biogenic emissions are also marked by low values from anthropogenic sources, for example toluene/benzene < 1 accounts for the loss of toluene due to the shorter lifetime. Removal of anthropogenic sources ensures that the biogenic marker represents natural biogenic sources such as grasses, forest, etc. This eliminates biogenic sources that are co-located with anthropogenic sources. These chemical characterizations are likely more stringent than necessary either with the number of chemical markers needed for each source type or the mixing ratio ranges used.

However, the Front Range is a mixture of multiple sources in a relatively small region and narrow chemical classification ranges limits sampling of multiple source types together.

2.4 Chemical Production

HFo, HAc, and GA chemical production on the Front Range was evaluated using the Master Chemical Mechanism, MCM v 3.3.1 (MCM, 2018), via website: http://mcm.leeds.ac.uk/MCM. HFo (Table 3.2), HAc (Table 3.3), and GA production and loss gas phase reactions (Table 3.4) were not modified from the MCM. All available C-130 aircraft measurements are italicized and used as the precursor inputs for the MCM reactions. It was assumed that all intermediates formed the desired species. For example, all CH_2OO from ethene ozonolysis (Table 3.2) reacted to HFo and not another secondary product. This leads to an overestimation of HFo, HAc, and GA. MCM reactions were excluded from the calculation if there were more than two intermediate species in between the aircraft measured precursor and HFo, HAc, or GA. The majority of the precursors are from TOGA. Aircraft TOGA precursor measurements were available to drive the MCM calculations on a two minutes cycle.

3. Results and Discussion

The goal of this study is to understand the distribution of HFo and AAES on the Colorado Front Range. Figure 3.1 shows HFo and AAES altitude profiles for the whole campaign. Data are grouped in 1 km bins where the diamond represents the median mixing ratio, the thick line the interquartile, and the thin line the 10^{th} – 90^{th} percentile for each altitude bin. The maximum altitude sampled during FRAPPÉ was ~7.5 km above sea level thus the altitude profile is from 0 to 8 km. This is the only

altitude data not presented as a.g.l in order to use all available data. As discussed in Section 2.1 the elevation measurement is missing for some flights thus a.g.l could not be calculated. AAES mixing ratios were higher than HFo for the whole campaign. The maximum HFo and AAES were in the 3-4 km bin which is between ~1.5-2.5 km a.g.l. HFo and AAES mixing ratios were < 1 ppb above 6 km. The high altitude measurements have smaller interquartile ranges reflective of cleaner background air and fewer data points than near the surface (Table S3.2). FRAPPÉ focused on low altitude sampling because the goal was to characterize emissions on the Colorado Front Range. As a result, the majority of flights were in the BL. The BL was often turbulent which resulted in aircraft vibrations that affected the PCIMS mass flow controllers and thereby impacted instrument response (Treadaway et al., 2018). AAES had greater variance, represented by the length of the 10^{th}-90^{th} percentile line. This could in part be due to the instrumental noise and chemical contamination in the airport hangar before flights (Treadaway et al., 2018).

3.1 Geographic and Chemical Divisions

To better understand HFo and AAES distribution, the Front Range was divided geographically and chemically. The geographic divisions (Figure S3.1) represent different dominate emission types including: Rocky Mountain National Park representing a forest region (green), Denver Metropolitan area representing urban emissions (red), and Greeley which has joint oil and natural gas (O&NG) and concentrated animal feeding operations (CAFOs) sources (cyan). In the Greeley area, O&NG and CAFOs are interspersed thus they are reported together. The chemical markers used for biogenic, urban, O&NG, and CAFO emission sources are in Table

S3.1. Figures 3.2 and 3.3 are box-whisker plots (Matlab boxplot function was used; Matlab version R2016b), for the (a) geographic and (b) chemical breakdowns for HFo and AAES for all flights and encompasses all altitudes. The median mixing ratio is shown as the red line in both figures and the notches represent the confidence interval for the median. When the notches do not overlap the different medians are statistically different with 95% confidence. Outliers are shown as red plus markers. Tables 3.5 and 3.6 list the median, interquartile range (IQR), and number of points found for each geographic region and chemical source type for HFo and AAES. While four chemical source types were evaluated, there was only enough data for biogenic and O&NG emission sources for HFo and biogenic, CAFO, and O&NG for AAES. Urban emissions could not be chemically identified in this analysis.

The HFo median was highest in predominately biogenic regions whether represented as the forested region geographically or by biogenic emission sources. The highest HFo median (0.78 ppb) was the forested region 2300 m BL. The high HFo routinely found in BL forested regions could be explained by missing sources (Schobesberger et al., 2016). Net upward HFo fluxes over a boreal forest found that there was a missing primary source or fast high-yield production from monoterpenes (Schobesberger et al., 2016). Geographically, all three HFo medians are statistically different ($p<0.001$, Kruskal-Wallis (1952)) and the Denver Metropolitan area had the second highest HFo. Chemically, there was no HFo data available with the CAFO and urban source types. The HFo IQR and median for the combined geographic O&NG/CAFO and chemically classified O&NG region were quite similar (Table 3.5 and 3.6). This suggests that O&NG emissions dominate HFo production compared to

CAFO. The high HFo and AAES chemical O&NG outliers are from August 11th (RF 11) and August 12th (RF 12) which are case studies discussed below. The biogenic HFo median is greater than O&NG and the two are statistically different ($p<0.001$, Kruskal–Wallis (1952)). Kruskal-Wallis is a nonparametric version of classical one-way ANOVA (Kruskal & Wallis, 1952),

The forest AAES median was significantly lower ($p<0.001$, Kruskal Wallis (1952)) than either the joint O&NG/CAFO or Denver Metropolitan medians. There are substantially more AAES outliers than HFo especially for the joint O&NG/CAFO region and the Denver Metropolitan area and no statistical difference between the medians for these two regions (Figure 3.3a). The geographic O&NG/CAFO outliers could be the difference of sampling in the general region at higher altitude versus the Greeley missed approaches where AAES mixing ratios were high (Section 3.2). A missed approach is flown at an airport and permits sampling as low as 20 m a.g.l. or 65 ft. Normal flight operations cannot sample below 300 m (1000 ft.) a.g.l. The AAES forest region median was half the biogenic chemical AAES median. The highest AAES forest outlier was 4.6 ppb whereas the biogenic chemical signature highest outlier was 16.8 ppb. This suggests that AAES was lower in the mountainous forest region but was impacted by biogenic emissions elsewhere – such as on the plains. The AAES chemical biogenic and O&NG medians are not different though the CAFO median is significantly lower than either the biogenic and O&NG medians ($p<0.001$, Kruskal-Wallis (1952)). The AAES CAFO median was about half the O&NG median. Both had narrow IQRs and multiple outliers. While the CAFO IQR was smaller than

O&NG, there were substantially more data points with 43 points meeting the O&NG criteria and 288 points meeting the CAFO criteria.

The chemical characterization is for the whole FRAPPÉ domain. Because of the co-location of O&NG and CAFO in the Greeley region, the O&NG and CAFO chemical criteria (Table S3.1) were applied over that geographic region to separate the two chemical sources. The O&NG chemically defined HFo median in the Greeley area was 0.62 ppb (n=9) which is at the high end of the IQR for the geographically defined O&NG/CAFO. There was no data for the CAFO source type for HFo. For AAES, the CAFO median was 3.2 ppb (n=30) and the O&NG median was 9.2 ppb (n = 7). The AAES O&NG median was three times higher than the geographic O&NG/CAFO AAES median (2.8, n = 435) though there were very few data points. This supports the chemical characterization that showed AAES mixing ratios were higher when associated with O&NG and not CAFO air masses. Previous literature has discussed CAFOs as a substantial HAc source (McGinn et al., 2003, Ngwabie et al., 2008, Yuan et al., 2017). Previous literature reported 0.06 ppb/ppb (Ngwabie et al., 2008) and 0.0302 $\pm$ 0.0055 ppb/ppb (Yuan et al., 2017) for cattle (beef and dairy) feedlots. For chemically defined CAFO data in the Greeley region, the AAES/NH_3 median ratio was 0.12 ppb/ppb and the IQR ranged from 0.012-0.18 ppb/ppb.

The validity of the chemically defined source types was evaluated with a principal component analysis (PCA) for C-130 data including HFo, AAES, aircraft location, and a wide range of chemical species associated with anthropogenic and natural emissions. PCA was applied to all data for RF 4-15 to remove any potential instrumental bias when the C-130 cooling system malfunctioned for the first three

flights. Some anthropogenic chemical species representing CAFO (NH_3), traffic (ethyne and ethene), O&NG (ethane), and several other chemical species were included. Natural chemical species associated with biogenic emissions included isoprene, MVK, pinenes, and others. Stratospherically influenced air defined by $O_3/CO>1.25$ was removed.

Figure S3.2 shows the first three principal components for all the variables used. Principal component 1 explains 52% of the variance and reflects the mixed urban emission sources encountered. Principal component 2 explains 36% of the variance and reflects biogenic emissions, especially isoprene and isoprene photochemical products. HFo and AAES are positively correlated with both components 1 and 2 which is not surprising. Principal component 3 (5% of the variance) could also be linked to urban emissions and perhaps more specifically city emissions with the high NO_x loading anti-correlated to most biogenic markers. PCA was unable to distinguish the different anthropogenic emission types. This highlights the complicated mixed chemistry and source types in the region.

3.2 Upslope Case Studies

AAES and HFo are compared for August 11th (RF 11) and August 12th (RF 12). Both were predicted to be mountain-valley circulation, or upslope-downslope, flights with air transported from the plains into the foothills. The plan was to fly vertically stacked legs over the plains (Greeley, Denver Metro) and foothills. Then stacked legs would be flown over the Continental Divide and a missed approach into Granby looking for spillover. These stacked legs usually flew three different altitudes along the same longitudinal line. This would help characterize chemical composition

near sources and how that changes downwind and with altitude. Figures 3.4 and 3.5 show the HFo and AAES mixing ratios (ppb) as a function of altitude and longitude for both case studies. There was little variation in AAES and HFo as a function of latitude especially compared to longitude and altitude. Looking at it as a function of longitude and altitude shows patterns of transport across the Front Range and how that changed above the surface.

The expected upslope did not develop on August 11th. There was a storm near Rocky Mountain National Park and evidence of stratospherically influenced air over the mountains (-105.6 E). Therefore the rest of the mountain runs were scraped for more foothills passes. There was evidence of weak air mass transport from the plains towards the mountains and easterly winds to the foothills (-105.4 E). Both AAES and HFo had a clear decrease in mixing ratio above 2 km representative of background air. The highest AAES (> 10 ppb, Figure 3.5) was during the low altitude legs over the eastern portion of the FRAPPÉ domain. The highest HFo (Figure 3.4) was during the low altitude legs over the Denver Metropolitan area and foothills.

AAES was at least 9 ppb during the Greeley missed approach (altitude < 0.35 km a.g.l) with a median of 12 ppb. In comparison, HFo median during the missed approach was 0.82 ppb with a maximum of 0.99 ppb (Figure 3.4). Greeley has joint emissions from O&NG and CAFO sources. Ethane (C_2H_6), representative of oil and gas operations, maximum was 23 ppb during the Greeley missed approach. Ammonia (NH_3), representative of CAFOs, was up to 22 ppb during the Greeley missed approach. Using the median values, the AAES/NH_3 ratio was 0.67 ppb/ppb. This is significantly higher than the cattle HAc/NH_3 ratios found by Yuan et al. (2017) and

Ngwabie et al. (2008). The AAES/NH_3 ratio reported here includes O&NG as well. A chemical CAFO AAES/NH_3 ratio could not be determined as there were no data points for the chemical criteria during this missed approach. It is also likely the sampled CAFO emissions were a mix of multiple sources. The high AAES at the start of the flight, including the missed approach, might also be due to contamination in the airport hangar. The PCIMS was flushed with N_2 gas before each flight inside the hangar though this was not always completely effective in preventing contamination. Even with the minimum reported AAES during the missed approach (9.3 ppb) and the maximum NH_3 the ratio was 0.42, higher than previously reported ratios.

High HFo (>1 ppb) and AAES (>10 ppb) along the Denver Metropolitan track corresponded with elevated NO_x (8 ppb). The highest isoprene (0.40 ppb) was also encountered in the Denver Metropolitan area. In general, the primary biogenic tracers, isoprene, MBO, and MVK, were all highest during the Greeley missed approach and in the Denver Metropolitan area and not the foothills transect (-105.4 E). This serves as further evidence that the Colorado Front Range is a mixture of source types.

The weather cooperated on August 12th (RF 12) and the original flight plan was followed. A midflight refueling stop was needed (21:40-22:41 UTC, Broomfield). The first flight segment flew stacked legs over Greeley, the Denver Metropolitan area, and foothills similar to the day before. After refueling, a second stack was flown over Denver and the foothills before two legs over the Continental Divide and a missed approach into Granby (-106 E).

AAES (Figure 3.5b) variation was similar to the 11th with higher AAES near anthropogenic sources in Greeley (14 ppb) and Denver (>10 ppb). The highest

ammonia (maximum of 180 ppb) and ethane (maximum of 40 ppb) was during the Greeley missed approach and along the northeast flight segments. The ammonia and ethane were significantly higher on the 12th. As mentioned above, the missed approach was a mixture of O&NG and CAFOs. The AAES/NH_3 missed approach ratio was 0.27 ppb/ppb. This lower ratio reflects the substantially higher ammonia. While the wind speeds were similar during the missed approach for the 11th and 12th, the wind in the northeastern sampling region was slightly faster on the 11th (~5-6 m/s) than the 12th (3-4 m/s). This suggests that the 12th may have been more stagnant in the Greeley region resulting in higher ammonia. There were data meeting the CAFO ammonia criteria ($\Delta NH_3/\Delta CH_4$>0.17) resulting in a 0.089 ppb/ppb AAES/NH_3 which is more in line with literature data (Ngwabie et al., 2008; Yuan et al., 2017). The AAES/NH_3 ratio was lower on August 12th because the ammonia was higher and not due to changes in AAES. The HFo median during the Greeley missed approach was lower (0.68 ppb) on the 12th compared to the 11th (1.5 ppb).

RF 12 sampled upslope and spillover into Granby (-106 E, Pfister et al., 2017). Evidence of this includes NO_x (~3 ppb) and ozone (75 ppb) transport from Denver to Granby (Figure S3.3). Winds for the lower altitude legs were all easterly including into Granby. AAES was lower along the mountains and foothills with a slight increase in Granby (4 ppb). HFo (Figure 3.4b) was highest along the foothills track and in Granby (~1.6 ppb) compared to Greeley and Denver. There was clear transport of ethane towards the foothills with 20 ppb near Fort Collins and Loveland (-105 E) and 5 ppb along the northern end of the foothills. The biogenic signature over the foothills and mountain was stronger than the day before. The highest MVK was in the

southwest over the mountains (-105.6 E). There was ~200 ppt isoprene along this same track though the highest was in Greeley similar to the day before. The highest MBO (~200 ppt) was below 1.5 km along the foothills track. HFo has a similar pattern to ozone on the foothills track. Ozone was ~10 ppb higher on August 12th than the day before with 75 ppb in Granby and at least 70 ppb along the foothills. This had the potential to be an ozone exceedance event. In fact, the next day was an ozone exceedance day at two Denver area EPA sites based on the current 0.07 ppm 8-hour maximum (EPA 8 Hour Ozone Data, accessed 3/1/2019).

These two flights highlight the complicated chemistry and meteorology of the Front Range and also where similar patterns exist. HFo mixing ratios were similar both days along the Denver Metropolitan pass and on the plains. However, HFo was several hundred ppt higher on August 12th in the foothills and mountains. This difference is due to both the fact that there was less transport from the plains on the 11th as it was the weaker upslope day and the presence of stratospherically influenced air which would have a lower HFo mixing ratio. AAES had a similar pattern between the two days though higher mixing ratios on the 11th. AAES during the Greeley missed approach was similar between days even though ammonia was substantially higher on the 12th. The anthropogenic portions of the flights over the plains had higher AAES than the foothills and mountains. These patterns suggest that HFo formation is influenced more by biogenic secondary sources rather than anthropogenic sources while AAES is the opposite. In the next section, HFo and AAES secondary production is evaluated using the Master Chemical Mechanism.

3.3 HFo and AAES Modeled Production

HFo, HAc, and GA gas phase production was assessed using the Master Chemical Mechanisms (MCM, v 3.3.1). This analysis was limited by available C-130 measurements but includes known dominant production sources. Reaction pathways are in Tables 3.2-3.4 and C-130 measured species are italicized. Only HFo has direct formation from a measured precursor, acetylene + HO. All other formation is from intermediates which react with other species or decompose to form HFo, HAc, and GA. This work assumes HFo, HAc, and GA are the only intermediate loss pathways. For example, both HFo and HAc have formation from Criegee or peroxy acetyl intermediates which have multiple loss reactions beyond organic acids and these other reaction are excluded from this analysis. MCM reactions were omitted if there were more than two intermediates in between the C-130 measured precursor and HFo, HAc, or GA. Production was calculated for all available precursor measurements for the whole flight. For example, TOGA isoprene measurements were about every two minutes; therefore, HFo from isoprene ozonolysis was calculated every two minutes.

The majority of HFo production came from Criegee B, C, and E (Figure 3.6). There was little difference in the breakdown of the three main Criegee sources between the two days. HFo secondary formation is a mixture of biogenic (isoprene, MBO, and MVK) and anthropogenic (ibutene, propene, and acrolein). Criegee B is the dominant source representing 44% of HFo production for August 11th and 37% for August 12th. It is likely the dominant source because it has multiple precursors (Table 3.2). Isoprene ozonolysis (Criegee E) represents 26% and 32% of HFo production for August 11th and 12th. HFo has been shown by other authors (e.g. Millet et al., 2015; Yuan et al., 2015) to be underestimated by chemical mechanisms. Yuan et al. (2015)

modified MCM 3.2 and added additional HFo production reactions. No additional reactions were added here because of the assumption that HFo is the only result from Criegee loss though this is unlikely. HFo hourly production rate was estimated for both flights and the production rate was less than 10 ppt/hr for the majority of the flight. The highest production rate, 30 ppt/hr on August 12th and 20 ppt/hr on August 11th, was during the Greeley missed approach – close to sources.

Propene represented a negligible HAc source (<1%). Peroxyacetyl nitrate (PAN) and acetaldehyde were the two dominate HAc sources (Table 3.3). Overall PAN dominated HAc production with 61% on August 11th and 84% on August 12th (Figure 3.7). PAN and acetaldehyde have primarily anthropogenic sources (Fischer et al., 2014). PAN is a secondary product of VOCs and nitrogen oxides in photochemical smog. The higher portion on the 12th may reflect the higher mixing ratios of other anthropogenic markers in the region that day as discussed above.

GA is produced with various intermediates (Table 3.4) coming from MBO, MVK, ethene, and acetaldehyde. Unlike the organic acids these are reactions are all with HO and not O_3 or some combination. A substantial fraction of GA production was from biogenic sources on both days. GA formation is primarily from MBO, MVK, and acetaldehyde (Figure 3.8). Half of GA production was from acetaldehyde on August 11th (50%) with comparable proportions of MBO (22%) and MVK (25%). GA production was more evenly distributed on August 12th between MBO (28%), MVK (37%), and acetaldehyde (31%).

As discussed in Section 2.2, a caveat to the PCIMS measurements is that HAc and GA must be accounted for together and reported as the operationally defined

AAES. The contribution of HAc and GA to AAES are evaluated with the MCM. The HAc production rate was higher for both days. The HAc median production rate on the 12th was 44 ppt/hr and GA was 1 ppt/hr. The GA HO loss rate was an order of magnitude greater than HAc. Given the larger production HAc production rate and slower loss rate it is likely that HAc represented a greater portion of AAES measurements when assuming the mixing ratios are controlled by gas phase processes.

4. Conclusion

HFo and AAES along the Colorado Front Range highlight the impact of sources on formation. HFo was highest near biogenic sources regardless of a chemical or geographic classification though there were anthropogenic HFo sources. The Denver Metropolitan area had the second highest HFo. HFo natural and anthropogenic formation mixture was also found with MCM estimated production. HFo secondary formation was split between biogenic and anthropogenic sources. Isoprene ozonolysis alone accounted for a third of the total HFo production. AAES was highest near anthropogenic sources, in particular oil and natural gas. The highest AAES encountered during the two case studies was during the Greeley missed approach – an area dominated by oil and gas and concentrated animal feeding operations. MCM estimated HAc production showed that HAc production was controlled by PAN and acetaldehyde. MCM GA production was lower than MCM HAc production and the GA loss rate was an order of magnitude higher. Working in this gas phase framework, i.e. ignoring deposition, AAES represents a greater portion of HAc to GA. This work contributes to our understanding of HFo, HAc, and GA formation and provides insight into VOC reaction pathways which impact ozone and HO formation.

References

Apel, E. C., Hornbrook, R. S., Hills, A. J., Blake, N. J., Barth, M. C., Weinheimer, A., et al. (2015). Upper tropospheric ozone production from lightning NO_x -impacted convection: Smoke ingestion case study from the DC3 campaign. *Journal of Geophysical Research: Atmospheres*, *120*(6), 2505–2523. https://doi.org/10.1002/2014JD022121

Bahreini, R., Ahmadov, R., McKeen, S. A., Vu, K. T., Dingle, J. H., Apel, E. C., et al. (2018). Sources and characteristics of summertime organic aerosol in the Colorado Front Range: perspective from measurements and WRF-Chem modeling. *Atmospheric Chemistry and Physics*, *18*(11), 8293–8312. https://doi.org/10.5194/acp-18-8293-2018

Baker, A. K., Beyersdorf, A. J., Doezema, L. A., Katzenstein, A., Meinardi, S., Simpson, I. J., et al. (2008). Measurements of nonmethane hydrocarbons in 28 United States cities. *Atmospheric Environment*, *42*(1), 170–182. https://doi.org/10.1016/j.atmosenv.2007.09.007

Blake, N. J., Blake, D. R., Simpson, I. J., Meinardi, S., Swanson, A. L., Lopez, J. P., et al. (2003). NMHCs and halocarbons in Asian continental outflow during the Transport and Chemical Evolution over the Pacific (TRACE-P) Field Campaign: Comparison With PEM-West B. *Journal of Geophysical Research*, *108*(D20), 8806. https://doi.org/10.1029/2002JD003367

Eilerman, S. J., Peischl, J., Neuman, J. A., Ryerson, T. B., Aikin, K. C., Holloway, M. W., et al. (2016). Characterization of Ammonia, Methane, and Nitrous Oxide Emissions from Concentrated Animal Feeding Operations in Northeastern Colorado. *Environmental Science and Technology*, *50*(20), 10885–10893. https://doi.org/10.1021/acs.est.6b02851

EPA:Federal Registrar. (2016). *Determinations of Attainment by the Attainment Date, Extensions of the Attainment Date, and Reclassification of Several Areas for the 2008 Ozone National Ambient Air Quality Standards (Final Rule)*. Retrieved from https://www.federalregister.gov/documents/2016/05/04/2016-09729/determinations-of-attainment-by-the-attainment-date-extensions-of-the-attainment-date-and

Finlayson-Pitts, B. J., & Pitts Jr, J. N. (1997). Pollution : Tropospheric Air Airborne Toxics , Ozone , Aromatic Polycyclic and Particles Hydrocarbons ,. *Science*, *276*(5315), 1045–1052. https://doi.org/10.1126/science.276.5315.1045

Fischer, E. V., Jacob, D. J., Yantosca, R. M., Sulprizio, M. P., Millet, D. B., Mao, J., et al. (2014). Atmospheric peroxyacetyl nitrate (PAN): A global budget and source attribution. *Atmospheric Chemistry and Physics*, *14*(5), 2679–2698. https://doi.org/10.5194/acp-14-2679-2014

Flocke, F., Pfister, G., Committee, S., Crawford, J., Langley, N., Cohen, R., et al. (2013). *FRAPPÉ A Proposed Field Experiment in Colorado for Summer 2014*.

Gerbig, C., Schmitgen, S., Kley, D., Volz-Thomas, A., Dewey, K., & Haaks, D. (1999). An improved fast-response vacuum-UV resonance fluorescence CO instrument. *Journal of Geophysical Research: Atmospheres*, *104*(D1), 1699–1704. https://doi.org/10.1029/1998JD100031

Gilman, J. B., Lerner, B. M., Kuster, W. C., & De Gouw, J. A. (2013). Source signature of volatile organic compounds from oil and natural gas operations in northeastern Colorado. *Environmental Science and Technology*, *47*(3), 1297–1305. https://doi.org/10.1021/es304119a

de Gouw, J., & Warneke, C. (2007). Measurements of volatile organic compounds in the earth's atmosphere using proton-transfer-reaction mass spectrometry. *Mass Spectrometry Reviews*, *26*(2), 223–257. https://doi.org/10.1002/mas.20119

Heikes, B. G., Treadaway, V., McNeill, A. S., Silwal, I. K. C., & O'Sullivan, D. W. (2017). An ion-neutral model to investigate chemical ionization mass spectrometry analysis of atmospheric molecules - application to a mixed reagent ion system for hydroperoxides and organic acids. *Atmospheric Measurement Techniques Discussions*, *3*(September), 1–50. https://doi.org/10.5194/amt-2017-286

Heikes, B. G., Treadaway, V., McNeill, A. S., Silwal, I. K. C., & O'Sullivan, D. W. (2018). An ion-neutral model to investigate chemical ionization mass spectrometry analysis of atmospheric molecules – application to a mixed reagent ion system for hydroperoxides and organic acids. *Atmospheric Measurement Techniques*, *11*, 1851. https://doi.org/10.5194/amt-11-1851-2018

Hornbrook, R., Apel, E., Hills, A., Blake, D., Blake, N., Schroeder, J., et al. (2015). Observations of VOCs in the Colorado Front Range during FRAPPÉ.

Hornbrook, R., Apel, E., Hills, A., Blake, D., Blake, N., Schroeder, J., et al. (2017). The Impact of Oil and Natural Gas Activity on Ozone Formation in the Colorado Front Range.

Hornbrook, R. S., Crawford, J. H., Edwards, G. D., Goyea, O., Mauldin III, R. L., Olson, J. S., & Cantrell, C. A. (2011). Measurements of tropospheric HO2 and RO2 by oxygen dilution modulation and chemical ionization mass spectrometry. *Atmospheric Measurement Techniques*, *4*(4), 735–756. https://doi.org/10.5194/amt-4-735-2011

Johnson, T. J., Sams, R. L., Profeta, L. T. M., Akagi, S. K., Burling, I. R., Yokelson, R. J., & Williams, S. D. (2013). Quantitative IR spectrum and vibrational assignments for glycolaldehyde vapor: Glycolaldehyde measurements in biomass burning plumes. *Journal of Physical Chemistry A*, *117*(20), 4096–4107. https://doi.org/10.1021/jp311945p

Kawamura, K., Ng, L. L., & Kaplan, I. R. (1985). Determination of organic acids (C1-C10) in the atmosphere, motor exhausts, and engine oils. *Environmental Science and Technology*, *19*(11), 1082–1086. https://doi.org/10.1021/es00141a010

Khare, P., Kumar, N., Kumari, K., & Srivastava, S. (1999). Atmospheric formic and acetic acids: An overview. *Reviews of Geophysics*, *32*(2), 227–248. Retrieved from http://www.agu.org/pubs/crossref/1999/1998RG900005.shtml

Kim, S., Karl, T., Guenther, A., Tyndall, G., Orlando, J., Harley, P., et al. (2010). Emissions and ambient distributions of Biogenic Volatile Organic Compounds (BVOC) in a Ponderosa pine ecosystem: interpretation of PTR-MS mass spectra. *Atmospheric Chemistry and Physics*, *10*, 1759–1771. https://doi.org/10.5194/acpd-9-20819-2009

Kruskal, W. H., & Wallis, W. A. (1952). Use of Ranks in One-Criterion Variance Analysis. *Journal of the American Statistical Association*, *47*(260).

Lee, Y. N., Zhou, X., Kleinman, L. I., Nunnermacker, L. J., Springston, S. R., Daum, P. H., et al. (1998). Atmospheric chemistry and distribution of formaldehyde and several multioxygenated carbonyl compounds during the 1995 Nashville/Middle Tennessee Ozone Study. *J. Geophys. Res.*, *103*(D17), 22449. https://doi.org/10.1029/98JD01251

Lindinger, W., Hansel, A., & Jordan, A. (1998). On-line monitoring of volatile organic compounds at pptv levels by means of proton-transfer-reaction mass spectrometry (PTR-MS) medical applications, food control and environmental research. *International Journal of Mass Spectrometry and Ion Processes*, *173*(3), 191–241. https://doi.org/10.1016/S0168-1176(97)00281-4

Mårtensson, L., Magnusson, M., Shen, Y., & Jönsson, J. Å. (1999). Air concentrations of volatile organic acids in confined animal buildings–determination with ion chromatography. *Agriculture, Ecosystems & Environment*, *75*(1–2), 101–108. https://doi.org/10.1016/S0167-8809(99)00072-9

Mauldin, R. L., Frost, G. J., Chen, G., Tanner, D. J., Prevot, A. S. H., Davis, D. D., & Eisele, F. L. (1998). OH measurements during the First Aerosol Characterization Experiment (ACE 1): Observations and model comparisons. *Journal of Geophysical Research: Atmospheres*, *103*(D13), 16713–16729. https://doi.org/10.1029/98JD00882

Millet, D. B., Baasandorj, M., Farmer, D. K., Thornton, J. A., Baumann, K., Brophy, P., et al. (2015). A large and ubiquitous source of atmospheric formic acid. *Atmospheric Chemistry and Physics*, *15*(11), 6283–6304. https://doi.org/10.5194/acp-15-6283-2015

Niki, H., Maker, P.D., Savage, L.P., Breitenbach, L. P. (1981). An FTIR study of mechanisms for the HO radical initiated oxidation of C2H4 in the presence of NO: detection of glycolaldehyde. *Chemical Physics Letters*, *80*(3), 499–503. https://doi.org/10.1016/0009-2614(81)85065-8

O'Sullivan, D. W., Silwal, I. K. C., McNeill, A. S., Treadaway, V., & Heikes, B. G. (2018). Quantification of gas phase hydrogen peroxide and methyl peroxide in ambient air: Using atmospheric pressure chemical ionization mass spectrometry with O2−, and O2−(CO2) reagent ions. *International Journal of Mass Spectrometry*, *424*, 16–26. https://doi.org/10.1016/j.ijms.2017.11.015

Paulot, F., Wunch, D., Crounse, J. D., Toon, G. C., Millet, D. B., DeCarlo, P. F., et al. (2011). Importance of secondary sources in the atmospheric budgets of formic and acetic acids. *Atmospheric Chemistry and Physics*, *11*(5), 1989–2013. https://doi.org/10.5194/acp-11-1989-2011

Pfister, G. G., Reddy, P. J., Barth, M. C., Flocke, F. F., Fried, A., Herndon, S. C., et al. (2017). Using Observations and Source-Specific Model Tracers to Characterize Pollutant Transport During FRAPPÉ and DISCOVER-AQ. *Journal of Geophysical Research: Atmospheres*, 510–538. https://doi.org/10.1002/2017JD027257

Ren, X., Mao, J., Brune, W. H., Cantrell, C. A., Mauldin III, R. L., Hornbrook, R. S., et al. (2012). Airborne intercomparison of HOx measurements using laser-induced fluorescence and chemical ionization mass spectrometry during

ARCTAS. *Atmospheric Measurement Techniques*, *5*(8), 2025–2037. https://doi.org/10.5194/amt-5-2025-2012

Richter, D., Weibring, P., Walega, J. G., Fried, A., Spuler, S. M., & Taubman, M. S. (2015). Compact highly sensitive multi-species airborne mid-IR spectrometer. *Applied Physics B*, *119*(1), 119–131. https://doi.org/10.1007/s00340-015-6038-8

Ridley, B., Ott, L., Pickering, K., Emmons, L., Montzka, D., Weinheimer, A., et al. (2004). Florida thunderstorms: A faucet of reactive nitrogen to the upper troposphere. *Journal of Geophysical Research*, *109*(D17), D17305. https://doi.org/10.1029/2004JD004769

Schobesberger, S., Lopez-Hilfiker, F. D., Taipale, D., Millet, D. B., D'Ambro, E. L., Rantala, P., et al. (2016). High upward fluxes of formic acid from a boreal forest canopy. *Geophysical Research Letters*, *43*, 9342–9351. https://doi.org/10.1002/2016GL069599

Stavrakou, T., Müller, J. F., Peeters, J., Razavi, A., Clarisse, L., Clerbaux, C., et al. (2012). Satellite evidence for a large source of formic acid from boreal and tropical forests. *Nature Geoscience*, *5*(1), 26–30. https://doi.org/10.1038/ngeo1354

Sullivan, J. T., McGee, T. J., Langford, A. O., ALvarez II, R. J., Senff, C. J., Reddy, P. J., et al. (2016). Quantifying the contribution of thermally driven recirculation to a high-ozone event along the Colorado Front Range using lidar. *Journal of Geophysical Research : Atmospheres*, *121*, 10377–10390. https://doi.org/10.1002/2016JD025229

Treadaway, V., Heikes, B. G., McNeill, A. S., Silwal, I. K. C., & O'Sullivan, D. W. (2018). Measurement of formic acid, acetic acid and hydroxyacetaldehyde, hydrogen peroxide, and methyl peroxide in air by chemical ionization mass spectrometry: Airborne method development. *Atmospheric Measurement Techniques*, *11*(4), 1901–1920. https://doi.org/10.5194/amt-11-1901-2018

Tuazon, E. C., & Atkinson, R. (1989). A product study of the gas-phase reaction of methyl vinyl ketone with the OH radical in the presence of NOx. *International Journal of Chemical Kinetics*, *21*(12), 1141–1152. https://doi.org/10.1002/kin.550211207

Vu, K. T., Dingle, J. H., Bahreini, R., Reddy, P. J., Apel, E. C., Campos, T. L., et al. (2016). Impacts of the Denver Cyclone on regional air quality and aerosol

formation in the Colorado Front Range during FRAPP?? 2014. *Atmospheric Chemistry and Physics*, *16*(18), 12039–12058. https://doi.org/10.5194/acp-16-12039-2016

Yokelson, R. J., Susott, R., Ward, D. E., Reardon, J., & Griffith, D. W. T. (1997). Emissions from smoldering combustion of biomass measured by open-path Fourier transform infrared spectroscopy. *Journal of Geophysical Research*, *102*(D15), 18865. https://doi.org/10.1029/97JD00852

Yokelson, R. J., Crounse, J. D., Decarlo, P. F., Karl, T., Urbanski, S., Atlas, E., et al. (2009). Emissions from biomass burning in the Yucatan. *Atmospheric Chemistry and Physics*, *9*, 5785–5812.

Yuan, B., Veres, P. R., Warneke, C., Roberts, J. M., Gilman, J. B., Koss, a., et al. (2015). Investigation of secondary formation of formic acid: urban environment vs. oil and gas producing region. *Atmospheric Chemistry and Physics*, *15*(4), 1975–1993. https://doi.org/10.5194/acp-15-1975-2015

Yuan, B., Coggon, M. M., Koss, A. R., Warneke, C., Eilerman, S., Peischl, J., et al. (2017). Emissions of volatile organic compounds (VOCs) from concentrated animal feeding operations (CAFOs): Chemical compositions and separation of sources. *Atmospheric Chemistry and Physics*, *17*(8), 4945–4956. https://doi.org/10.5194/acp-17-4945-2017

Zheng, W., Flocke, F. M., Tyndall, G. S., Swanson, A., Orlando, J. J., Roberts, J. M., et al. (2011). Characterization of a thermal decomposition chemical ionization mass spectrometer for the measurement of peroxy acyl nitrates (PANs) in the atmosphere. *Atmospheric Chemistry and Physics*, *11*(13), 6529–6547. https://doi.org/10.5194/acp-11-6529-2011

Table 3.1: Chemical Instrumentation onboard the NSF/NCAR C-130 during FRAPPÉ used in this analysis

Instrument	Species	Uncertainty	Reference/PI
Trace Organic Gas Analyzer (TOGA)	54 volatile organic compounds	Varies by species	Apel et al. (2015)
Whole Air Sampler (WAS)	69 volatile organic compounds	Not Listed	Blake et al. (2003)
NCAR Aero-Laser 5200	CO	3 ppbv +/- 3%	Gerbig et al. (1999)
Picarro 2311	CO_2, CH_4, H_2O	0.25 ppmv CO_2 & 3 ppbv CH_4 for a 0.2 sec averaging time 100 ppmv for H_2O	Frank Flocke & Teresa Campos
NCAR PAN Chemical Ionization Mass Spectrometer (CIMS)	PAN and PPN	13%	Zheng et al. (2011)
Aerodyne Dual NH3/HNO3 QCL Instrument	NH_3	+/- (22% +0.305 ppbv) + 0.058 ppbv	Scott Herdon
CAMS	C_2H_6, CH_2O	3%	Richter et al. (2015)
Peroxide CIMS (PCIMS)	H_2O_2, CH_3OOH, HCOOH, CH_3COOH	H_2O_2 30%; CH_3OOH 30%; HCOOH 30%; CH_3COOH 50%	Heikes et al. (2018); O'Sullivan et al. (2017); Treadaway et al. (2018)
Proton-transfer-reaction mass spectrometer (PTR-MS)	Methanol, acetonitrile, acetaldehyde, acetone+propanal, MBO+isoprene, MVK+MACR+HMPR, benzene, toluene, C8 aromatics, C9 aromatics	~20%	de Gouw & Warneke (2007); Lindinger et al. (1998)
HOx CIMS	HO,HO_2, RO_2, H_2SO_4	HO,HO_2 ~35% RO_2, H_2SO_4 ~45%	Hornbrook et al. (2011); Mauldin et al. (1998); Ren et al. (2012)
Gas phase chemiluminescence	NO, NO_2, O_3	NO 20 pptv + 10% NO_2 40 pptv + 15% O_3 3 ppbv + 5%	Ridley et al. (2004)

Table 3.2: Formic acid (HCOOH) Master Chemical Mechanism (v. 3.3.1) production and loss reactions. Italicized species were measured on the C-130.

Production
C_2H_2 + *HO* -> **HCOOH** + CO + HO_2
C_2H_4 + *O_3* -> CH_2OOA
MBO + *O_3* -> CH_2OOB
MVK + *O_3* -> CH_2OOB
C_3H_6 + *O_3* -> CH_2OOB
Acrolein + *O_3*-> CH_2OOB
Ibutene + *O_3* -> CH_2OOC
Isoprene + *O_3* -> CH_2OOE
b-*pinene* + *O_3* -> CH_2OOF
MACR + *O_3* -> CH_2OOG
$CH_2OOA/B/C/E/F/G$ + *H_2O* -> **HCOOH**
Loss
HCOOH + *HO* -> products

Table 3.3: Acetic acid (CH_3COOH) Master Chemical Mechanism (v. 3.3.1) production and loss reactions. Italicized species were measured on the C-130.

Production
C_3H_6 + *O_3* -> CH_3CHOOA
CH_3CHOOA -> CH_3CHOO
CH_3CHOO + *H_2O* -> **CH_3COOH**
PAN -> CH_3COOO
CH_3CHO + *HO* -> CH_3COOO
CH_3COOO + *HO_2* -> **CH_3COOH**
CH_3COOO + *RO_2* -> **CH_3COOH**
Loss
CH_3COOH + *HO* -> products

Table 3.4: Glycolaldehyde ($H_2COHCHO$) Master Chemical Mechanism (v. 3.3.1) production and loss reactions. Italicized species were measured on the C-130.

Production
MBO + *HO* -> $MBOAO_2$
$MBOAO_2$ + *NO* -> MBOAO
$MBOAO_2$ + RO_2 -> MBOAO
MBOAO -> **$H_2COHCHO$**
MVK + *HO* -> $HMVKBO_2$
$HMVKBO_2$ + *NO* -> HMVKBO
$HMVKBO_2$ + RO_2 -> HMVKBO
HMVKBO -> **$H_2COHCHO$**
C_2H_4 + *HO* -> $HOCH_2CH_2O_2$
$HOCH_2CH_2O_2$ + *NO* -> $HOCH_2CH_2O$
$HOCH_2CH_2O_2$ + RO_2 -> $HOCH_2CH_2O$
$HOCH_2CH_2O_2$ -> **$H_2COHCHO$**
$HOCH_2CH_2O$ + O_2 -> **$H_2COHCHO$**
CH_3CHO + *HO* -> $HCOCH_2O_2$
$HCOCH_2O_2$ -> **$H_2COHCHO$**
Loss
$H_2COHCHO$ + *HO* -> products

Table 3.5: Formic acid (HFo) and acetic acid equivalent sum (AAES) boundary layer (BL, 1000 m and 2300 m) medians, interquartile range, and number of points for the three geographic divisions: Forest (over Rocky Mountain National Park), the combined oil and natural gas (O&NG) and concentrated animal feeding operations (CAFO), and the Denver Metropolitan Area

		Forest	O&NG/CAFO	Denver Metropolitan
HFo (ppb)	1000 m BL	1.0, 0.74-1.2 (n = 18)	0.39, 0.24-0.61 (n = 182)	0.52, 0.39-0.71 (n = 558)
	2300 m BL	0.78, 0.35-0.95 (n = 99)	0.42, 0.26-0.67 (n = 217)	0.53, 0.42-0.78 (n = 652)
	All data	0.75, 0.33-0.94 (n = 128)	0.40, 0.24-0.66 (n = 231)	0.52, 0.39-0.77 (n = 711)
AAES (ppb)	1000 m BL	2.4, 2.2-3.2 (n = 32)	2.8, 1.9-6.1 (n = 364)	3.7, 2.3-4.5 (n = 1129)
	2300 m BL	1.4, 0.78-1.9 (n = 190)	2.9, 2-6.3 (n = 419)	3.7, 2.3-4.5 (n = 1278)
	All data	1.6, 0.92-2 (n = 253)	2.8, 1.8-6.2 (n = 435)	3.6, 2.1-4.4 (n = 1379)

Table 3.6: Formic acid (HFo) and acetic acid equivalent sum (AAES) boundary layer (BL, 1000 m and 2300 m) medians, interquartile range, and number of points for the four chemical source types in Table S1: biogenic, oil and natural gas (O&NG), and concentrated animal feeding operations (CAFO), and urban. No Data is used if there was less than 2 points. If there are only 2 points both are listed.

		Biogenic	O&NG	CAFO	Urban
HFo (ppb)	1000 m BL	No Data	0.18, 0.86 (n = 2)	No Data	No Data
	2300 m BL	0.33, 0.33-0.39 (n = 3)	0.18, 0.86 (n = 2)	No Data	No Data
	All data	0.63, 0.44-0.84 (n = 940)	0.43, 0.35-0.54 (n = 69)	No Data	No Data
AAES (ppb)	1000 m BL	No Data	No Data	3.2, 2.9-3.5 (n = 44)	No Data
	2300 m BL	No Data	No Data	1.7, 1.0-3.2 (n = 98)	No Data
	All data	3.3, 2.2-4.9 (n = 512)	3.4, 3.0-4.2 (n = 43)	1.8, 1.3-2.5 (n = 288)	1.1,1.6 (n=2)

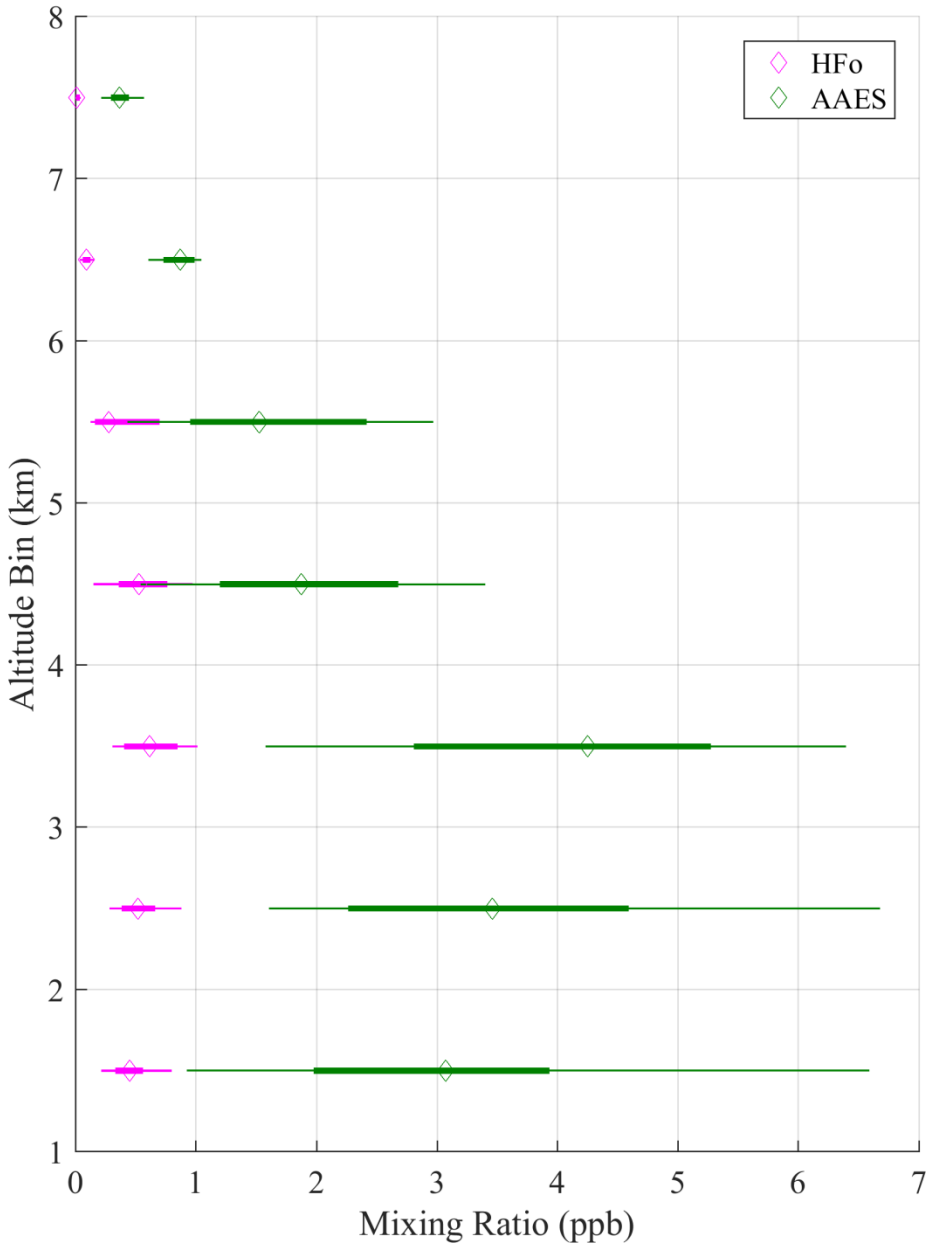

Figure 3.1: GPS altitude profiles for formic acid (HFo) and the acetic acid equivalent sum (AAES) mixing ratios (ppb) for the whole campaign. Data are grouped into 1 km bins and the diamond represents the median for each altitude bin, the thick lines the interquartile, and the thin line the 10^{th} – 90^{th} percentile.

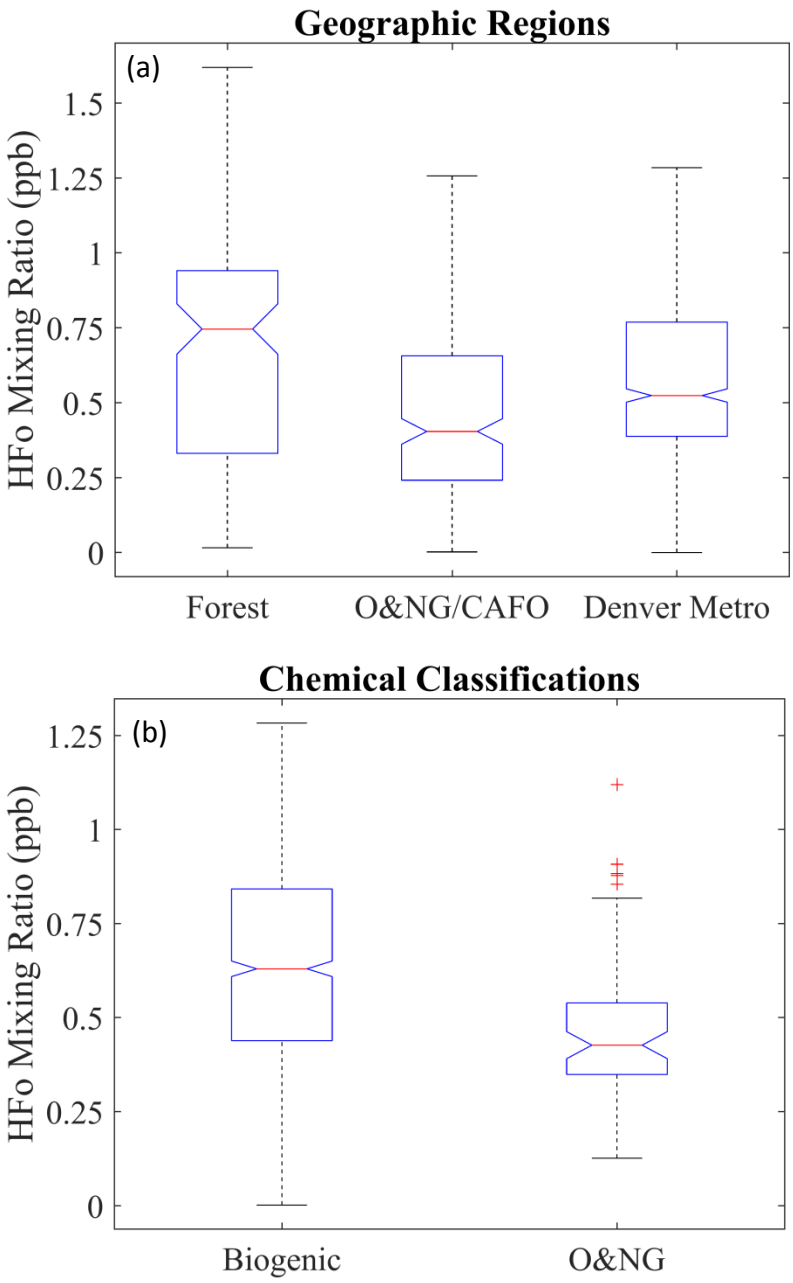

Figure 3.2: Formic acid (HFo) mixing ratio (ppb) box-whisker plot for the geographic regions (a) and chemical classifications (b) with enough available data. The geographic regions are: forest (over Rocky Mountain National Park), the combined oil and natural gas (O&NG) and concentrated animal feeding operations (CAFO), and the Denver Metropolitan Area. The two chemical source types with enough data (see Table 3.6) are biogenic and O&NG. The red line is the median and the notches are the median 95% confidence interval. The box shows the interquartile range from the 25th (q_1) to 75th (q_3) percentile. The whiskers (w) extend to the most extreme values not defined as outliers. Outlier data (red plus) are greater than $q_3 + w(q_3-q_1)$ or less than $q_1 + w(q_3-q_1)$.

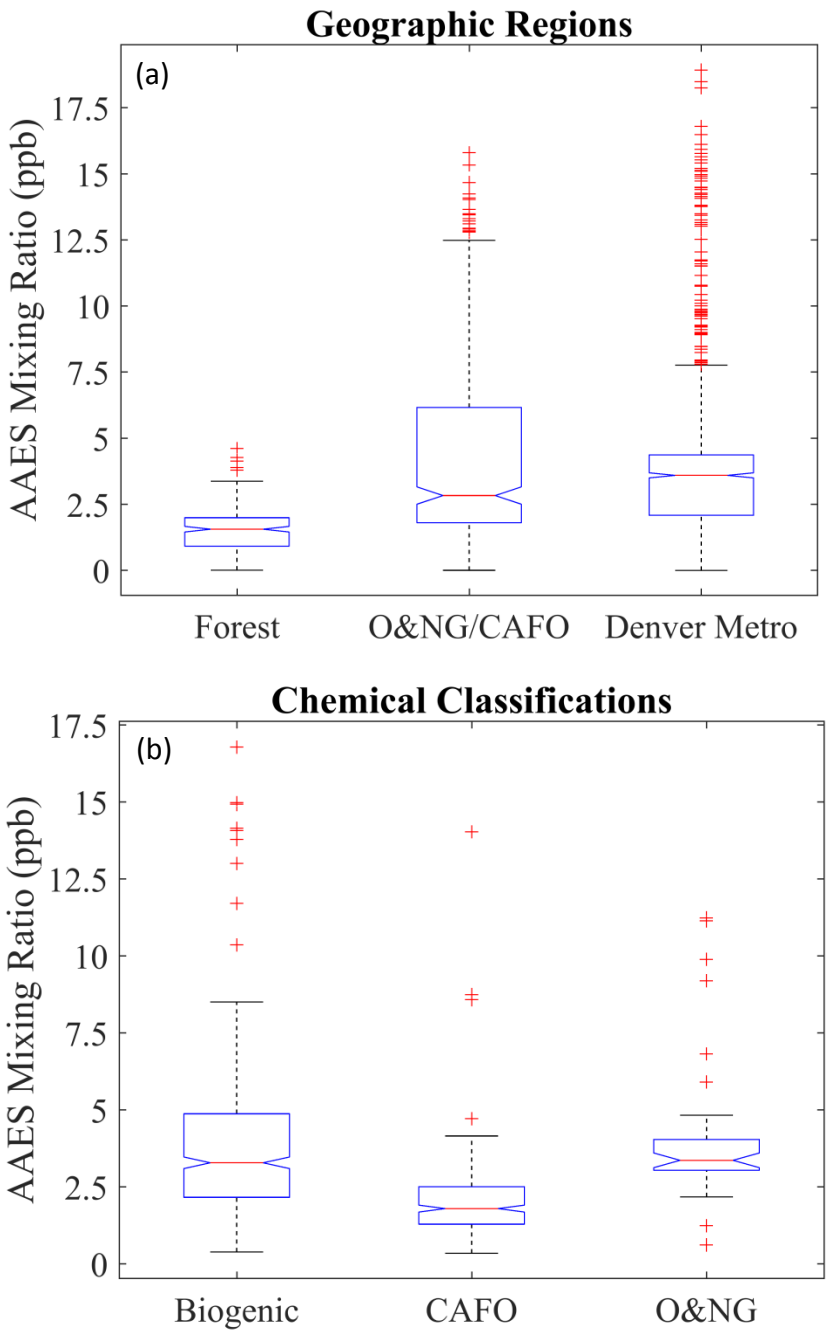

Figure 3.3: Same as Figure 3.2 except for the acetic acid equivalent sum (AAES). The three chemical source types with enough data (see Table 3.6) are biogenic, concentrated animal feeding operations (CAFO), and oil and natural gas (O&NG).

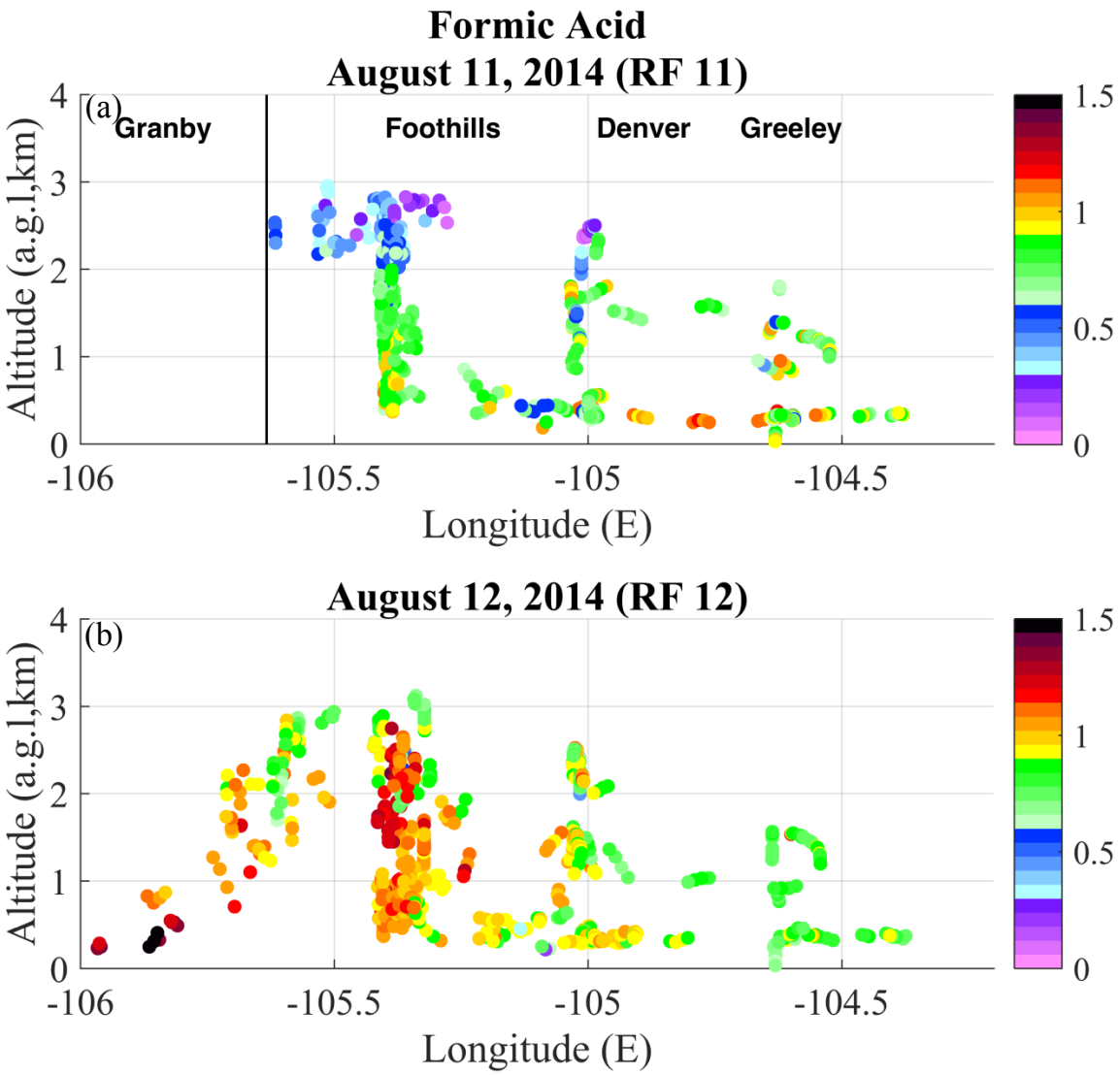

Figure 3.4: Formic acid mixing ratios (colorbar in ppb) for the (a) August 11th flight (RF 11) and (b) August 12th flight (RF 12) as a function of longitude (E) and altitude (above ground level (a.g.l), km). Relevant cities are labeled and the black line is the Continental Divide.

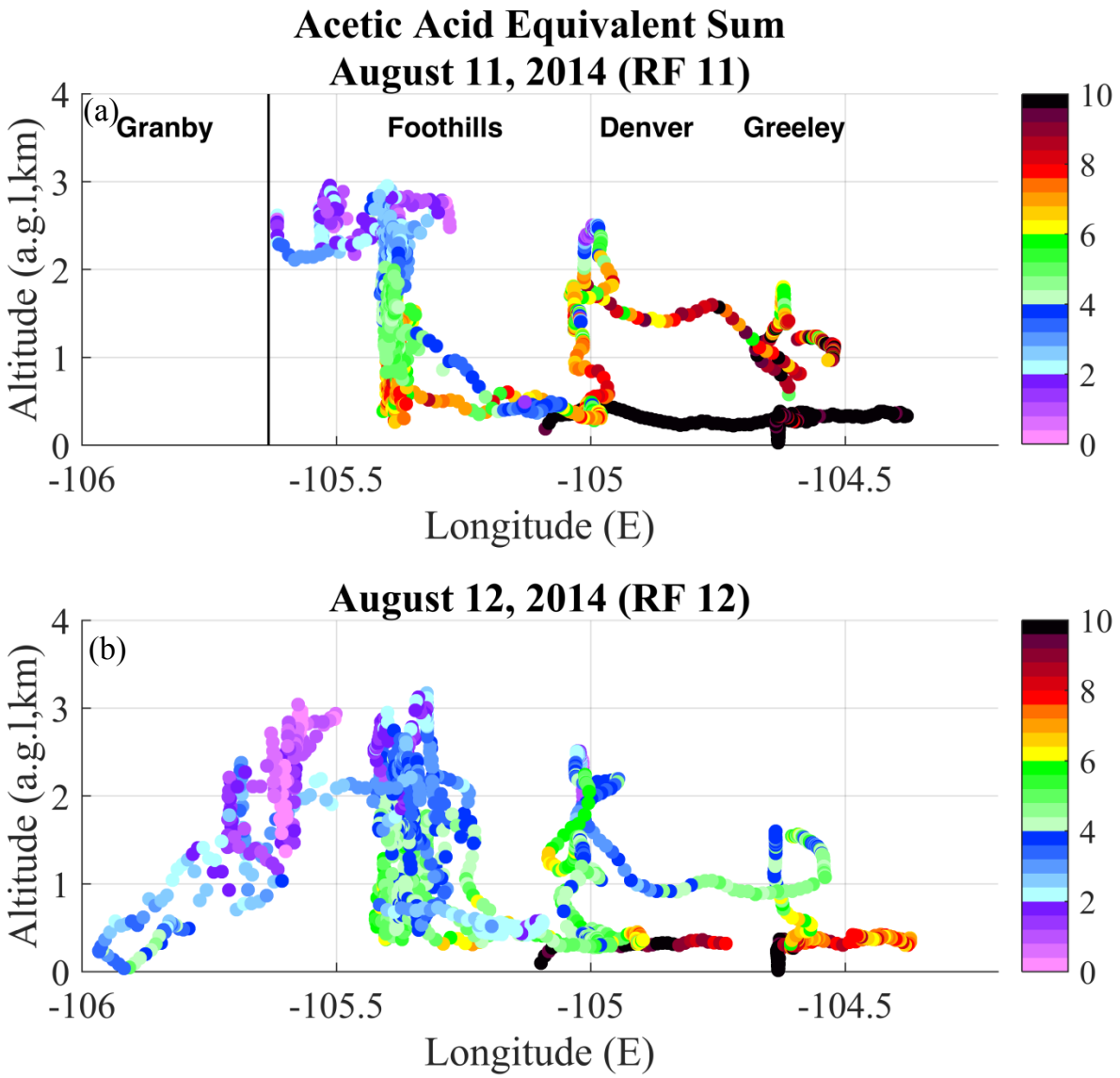

Figure 3.5: Same as Figure 3.4 but for acetic acid equivalent sum (AAES) mixing ratios (colorbar in ppb). Relevant cities are labeled and the black line is the Continental Divide.

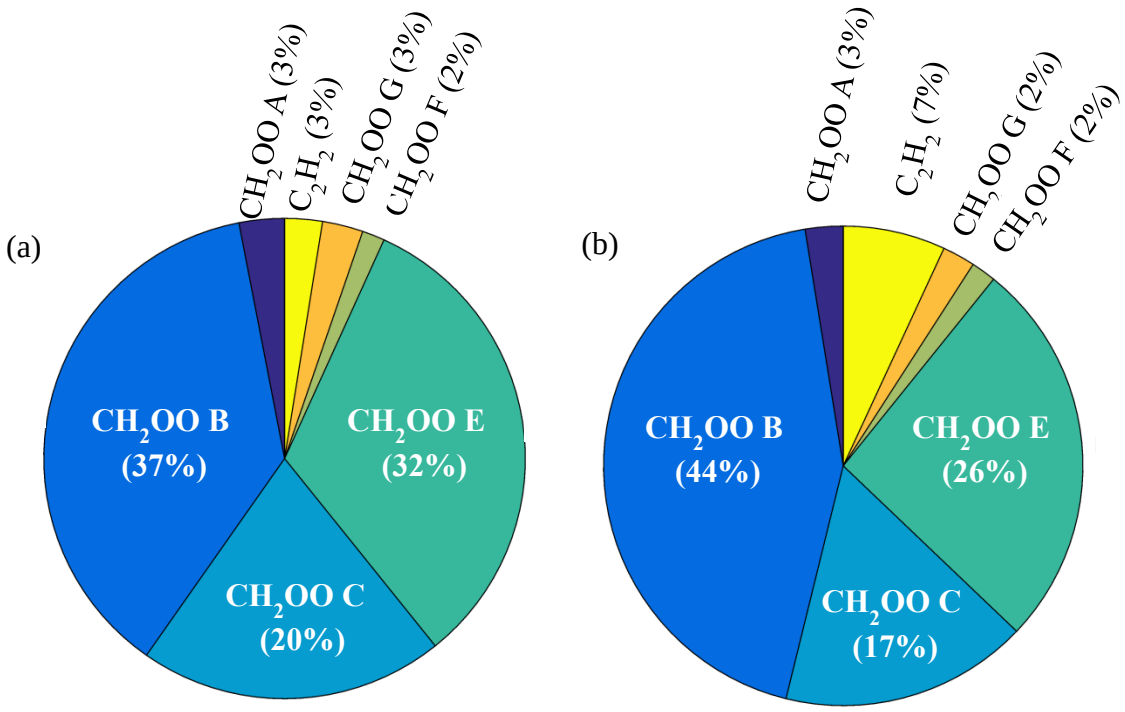

Figure 3.6: Formic acid secondary production sources using the Master Chemical Mechanism v 3.3.1 for (a) August 11th and (b) August 12th. The reaction pathways are listed in Table 3.2. CH_2OO is the Criegee intermediate.

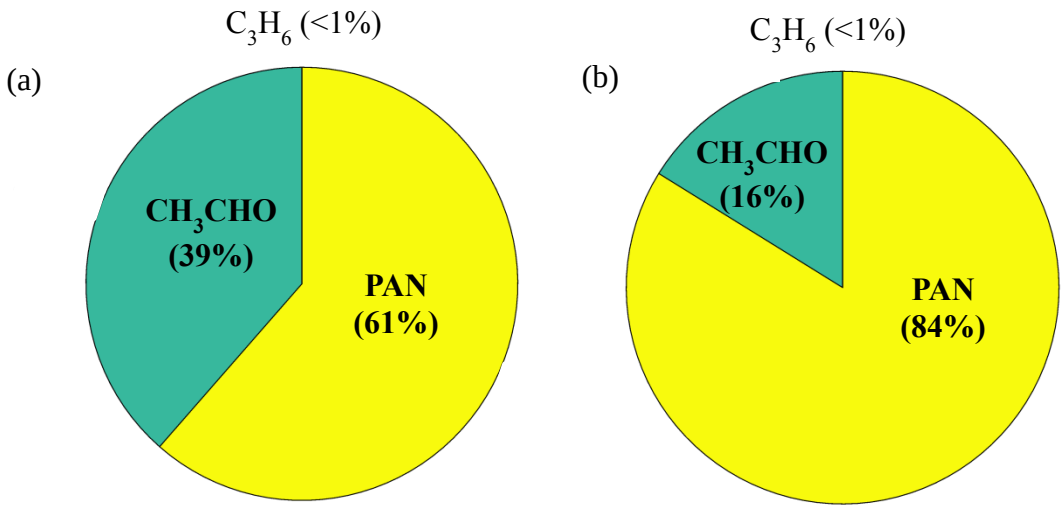

Figure 3.7: Acetic acid secondary production sources using the Master Chemical Mechanism v 3.3.1 for (a) August 11th and (b) August 12th. The reaction pathways are listed in Table 3.3.

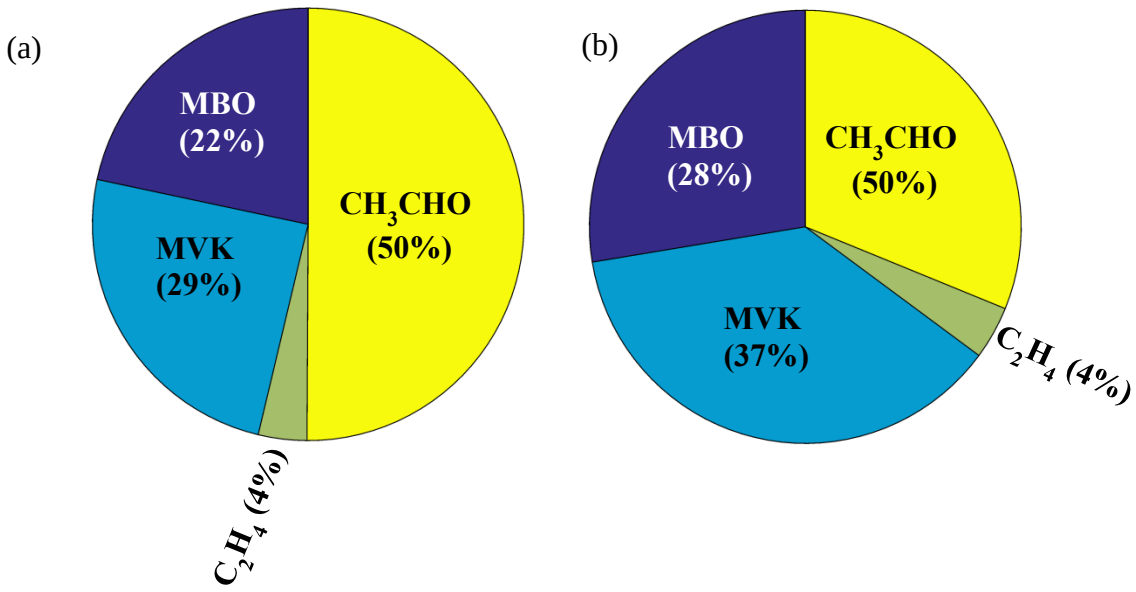

Figure 3.8: Glycolaldehyde secondary production sources using the Master Chemical Mechanism v 3.3.1 for (a) August 11th and (b) August 12th. The reaction pathways are listed in Table 3.4.

Table S3.1: Chemical characterization of four primary source regions sampled during FRAPPÉ. N/A – Not applicable, LOD – Limit of Detection

Source Category	ΔNH3/ΔCH4[a] (mol/mol)	Propane/Ethyne (ppb/ppb)[c]	Isoprene, MVK, MACR, MBO & b-pinene[b] (ppt)	iC5/C5 (ppb/ppb)[c,d]	Toluene/ Benzene (ppt/ppt)[d,e]	NO_x (ppb)[f]
CAFO	≥0.17	N/A	<100	<0.5	<2	<10
O&NG	<0.17	>20	<100	0.8-1.0	<2	<10
Urban	<0.17	N/A	<100	1.5-2.5	>2	>20
Biogenic	<0.17	<0.01	Above LOD	<0.5	<1	<2

a) Eilerman et al. (2016)
b) Kim et al. (2010)
c) Gilman et al. (2013)
d) Hornbrook et al. (2015)
e) Baker et al. (2008)
f) Hornbrook et al. (2017)

Table S3.2: Number of C-130 10 second data points in each altitude bin

Altitude Bin (km)	Number of Data Points
7-8	215
6-7	368
5-6	1449
4-5	4183
3-4	5455
2-3	7841
1-2	9773
0-1	0

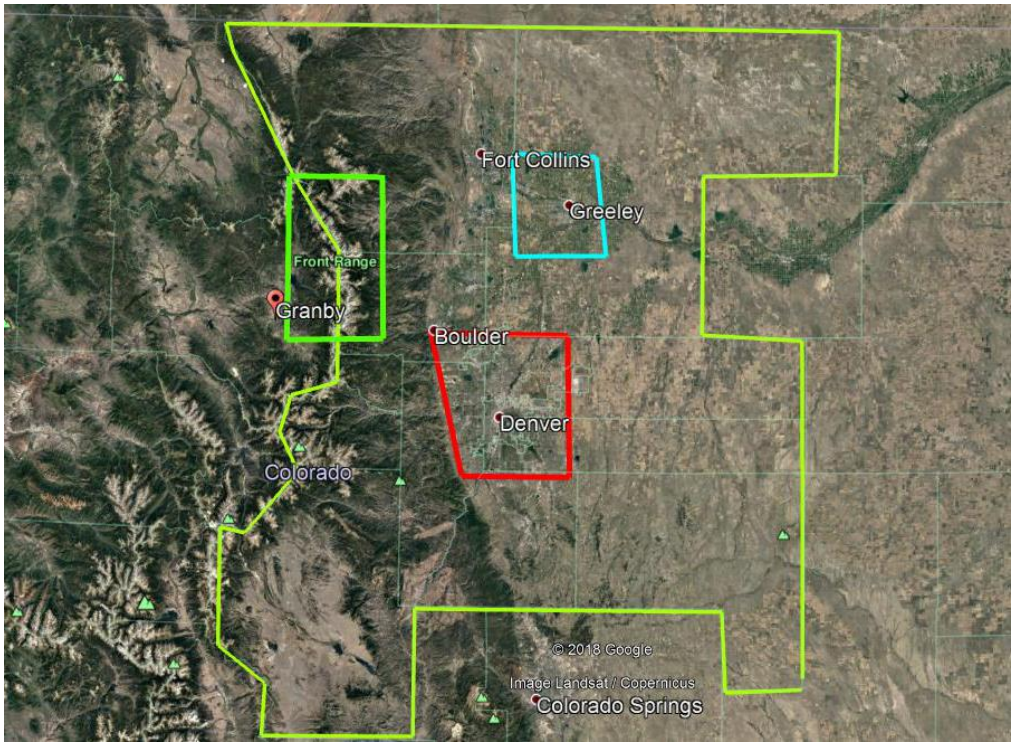

Figure S3.1: Google Earth map of geographic regions used for organic acid analysis. The overall outline shows the Colorado Front Range with designated forest region representing forested biogenic emissions (green box), Denver Metropolitan region representing urban emissions (red box), and the Greeley area representing the co-located oil and natural gas operations and concentrated animal feeding emissions (cyan box).

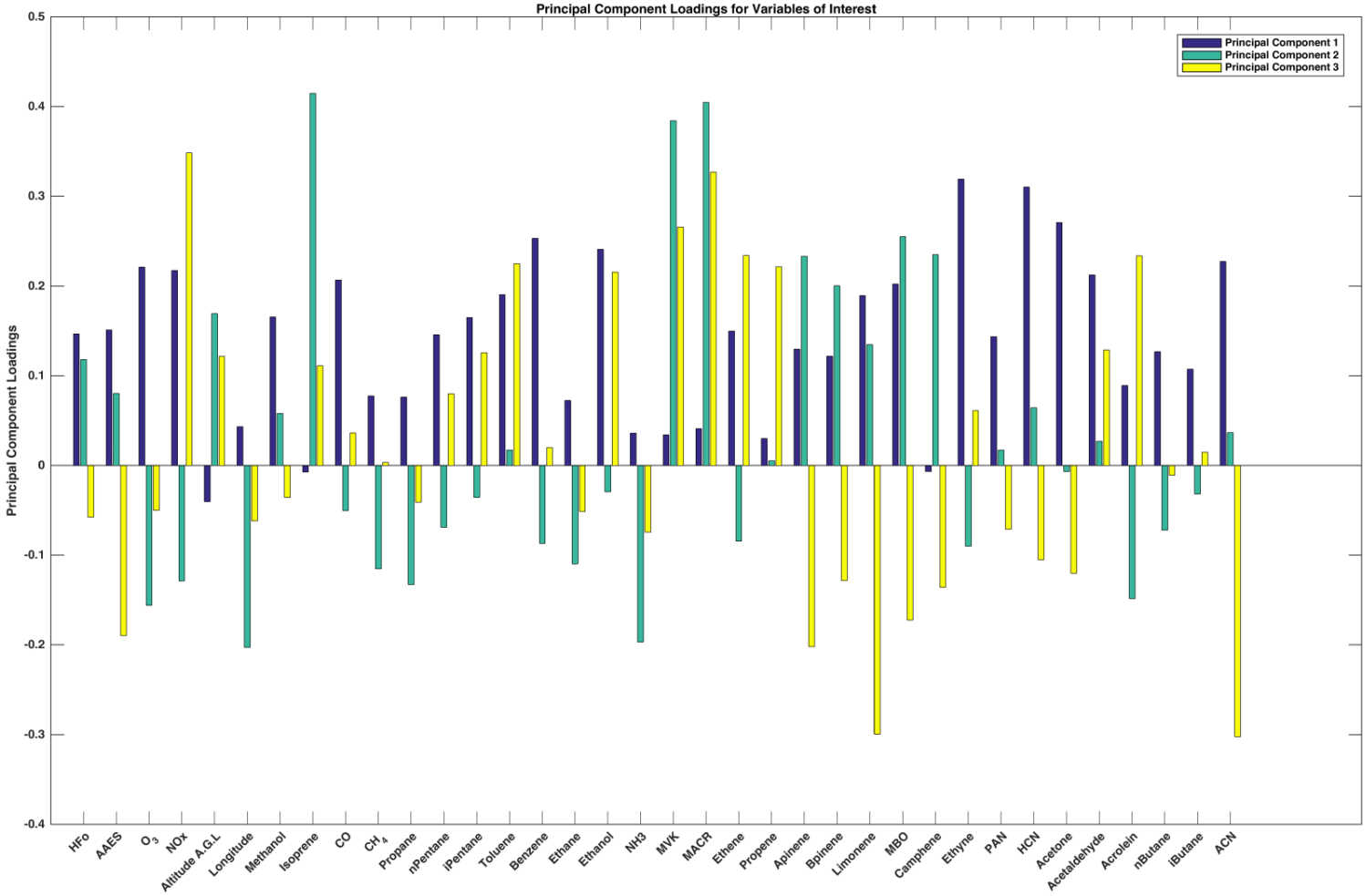

Figure S3.2: Principal component analysis of C-130 data for Research Flights 4-15. The first three principal components are shown representing 93.8% of the variance

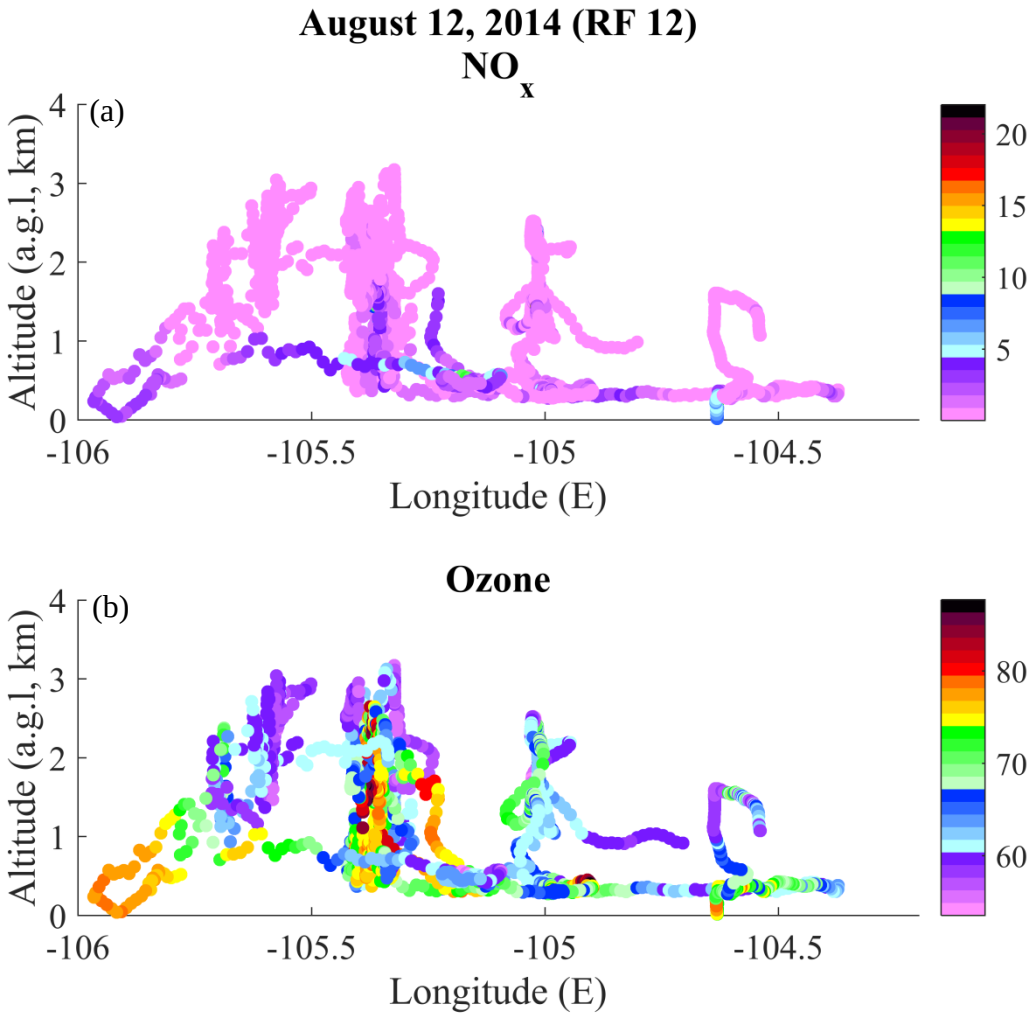

Figure S3.3: NO_x (a, ppb) and ozone (b, ppb) for Research Flight 12 on August 12th as a function of longitude and altitude above ground level

CONCLUSION

This dissertation explored the formation, transportation, and removal of formic acid (HFo) and acetic acid (HAc) in the troposphere. Results from two field campaigns, box models, and the Weather Research and Forecasting with coupled Chemistry (WRF-Chem) regional chemical transport model addressed the following questions:

1. Does organic acid scavenging extent differ between a convective multicell complex and an isolated convective cell?
2. Can HFo serve as a tracer of cloud processed air?
3. What HFo potential sources are we not accounting for in models? What does this tell us about the differences in production pathways between HFo and HAc?
4. How do HFo and HAc distributions vary based on natural and anthropogenic sources?

In addition to the questions above, manuscripts 2 and 3 explored the relative contributions of HAc and glycolaldehyde (GA) to the operationally defined acetic acid equivalent sum (AAES). Based on model simulations and previous literature measurements, the AAES HAc:GA instrumental sensitivity was closer to a 1:1 than 1:10 though it is likely the sensitivity is in between these two extremes.

Manuscripts 1 and 2 analyzed an airmass case study, Research Flight 03 on May 21, 2012, from the Deep Convective Clouds and Chemistry Experiment (DC3). The May 21st case study was chosen because there was higher than expected HFo by a

few hundred parts per trillion (ppt) above background levels in a region dominated by convective outflow. This HFo increase suggests either transport from the boundary layer or formation within the storm and subsequent release in the outflow.

Manuscript 1 discussed combinations of cloud microphysics schemes in conjunction with different temperature ranges for the Fierro lightning data assimilation (LDA) method. The Morrison double moment cloud microphysics scheme coupled with an LDA temperature range of 261 – 291 K best replicated the observed storm vertical velocity and vertical mass transport. Although this WRF-Chem set-up had a slightly lower cloud top height than observed, mass transport was an important component to accurately represent as the objective of Manuscript 2 was to look at transport through deep convection.

Manuscript 2 used the optimal WRF-Chem set-up determined in Manuscript 1. The scavenging efficiencies of multiple soluble species were calculated for both observations and WRF-Chem including those detected by PCIMS: hydrogen peroxide, methyl hydroperoxide, HFo, HAc, and GA. These are the first measurements of HFo and AAES on storm time scales in the United States. Despite the high solubilities, both HFo and AAES were lofted to the upper troposphere. Two simulated storms, isolated convection and a convective complex, were compared to see how storm structure impacts the scavenging efficiency of soluble species. Based on both DC3 observations and WRF-Chem simulations there was no significant difference in scavenging between a convective multicell complex and an isolated convective cell for HFo or AAES.

Manuscript 2 further explored the possibility of aqueous production and release and the most conducive conditions to produce the HFo plume noted at high altitude. Photochemical box model results suggested this HFo upper troposphere plume could be possible if there were multiple HFo aqueous sources and the cloud evaporated releasing HFo to the gas phase. It is also possible that the cloud water in this storm was more acidic preventing formate from reacting with HO and thus an HFo sink. Confounding this discuss was the absence of HFo storm inflow measurements to assess if this plume could have been from a local region of elevated surface HFo that was ingested into the storm, as was noted in sulfur dioxide. There is still no clear evidence for the feasibility of using HFo to detect cloud processed air.

Manuscript 2 used observed HFo measurements to constrain WRF-Chem as this dissertation corroborated previous work showing that organic acids, HFo in particular, are underpredicted in chemical transport models. WRF-Chem HFo mixing ratios were substantially lower than expected, less than 10 ppt, while observed HFo ranged from 28 – 724 ppt. As a result, WRF-Chem and the MOZART gas phase chemical mechanism were evaluated as to the causes of this underprediction. MOZART estimated HFo mixing ratios were no more than a third of observations without the addition of isoprene ozonolysis with a 31% HFo yield. Further, acetylene, a major HFo precursor in MOZART, was four orders of magnitude lower than that observed and it was concluded that acetylene was underrepresented in the WRF-Chem emission files. As a consequence secondary production of HFo was significantly underrepresented in the model.

Manuscript 3 focused on the Front Range Atmospheric Pollution and Photochemistry Experiment (FRAPPÉ) field campaign and in particular HFo and AAES source characterization. FRAPPÉ was designed to explore ozone over the Colorado Front Range and there is a potential role for organic acids to aid in characterizing carbon processing and ozone chemistry. HFo was highest in forested regions and near biogenic emissions. AAES was highest near anthropogenic sources including the Denver Metropolitan Area and near oil and gas operations. In addition to a campaign wide characterization, two case study flights, August 11th and 12th, were analyzed. These two were chosen because both were forecasted to be upslope, or mountain-valley, circulation flights; although, this was only observed on August 12th. August 12th upslope flow resulted in a "spillover" event in which Front Range air made it up and over the divide to Granby, CO located on the western slope. Elevated HFo was measured in the upslope flow and the highest HFo measured on the 12th was during the spillover event. The same pattern was not observed in AAES.

HFo, HAc, and GA secondary production for the August 11th and 12th flights was estimated using VOC measurements of the acid precursors also obtained on the C-130. The Master Chemical Mechanism was interrogated to identify these precursors. Both anthropogenic and biogenic sources for HFo were present though the majority was from biogenic precursors. A third of HFo production was attributed to isoprene ozonolysis alone. HAc production was found to be controlled by anthropogenic sources with at least 60% from peroxyacetyl nitrate (PAN), a secondary product of VOCs and nitrogen oxides in photochemical smog. GA production was determined to be a mix of anthropogenic and biogenic sources with at least 50% of its

production from MBO and MVK. MVK is an isoprene secondary product and MBO emissions are linked to coniferous trees which are found in the Rocky Mountains. FRAPPÉ measurements and MCM production estimates underscored the breakdown between biogenic and anthropogenic sources for HFo and HAc on the Colorado Front Range.

This work reinforces prior analyses showing organic acids are underpredicted in chemical transport models and highlights gaps in understanding atmospheric carbon processing. As shown here, both organic acids are lofted to the upper troposphere through midlatitude deep convection which will transport them far from their emission source. Moving forward, these measurements can be used to better constrain model reactions to improve our understanding of carbon processing in the atmosphere.